A new concept short pulse fiber laser source.

Igor Samartsev

Femtosecond Optics Group Photonics,

Department of Physics

Imperial College

London

United Kingdom

May 2021

Thesis submitted for the degree of Doctor of Philosophy

of Imperial College London

and for the Diploma of the Imperial College

All of the work presented in this thesis was carried out by the author in the period 2017-2021 at the

Blackett Laboratory, Imperial College London and

IPG Photonics laboratory Oxford MA USA.

Any work taken from external sources is duly acknowledged in the text.

Igor Samartsev May 2021

Abstract

Ultrashort-pulse fiber laser systems, which offer, due to their high peak pulse intensity in combination with high pulse frequencies (repetition rate), an innovative technology of nonlinear interaction with materials, help to fabricate components with unprecedented quality, precision and speed. Also due to the short pulse duration, laser energy can be introduced into the material in a shorter time than heat transfer occurs, which thus prevents thermal damage to the part. It is not surprising that industrial laser systems with a sub-nanosecond pulse length are widely used in the markets of precision processing, medical devices and in many other applications. The most critical component of such systems is the seed laser source. To date, the existing devices in the commercial market do not fully satisfy the industrial requirements.

In this thesis I describe a new concept for the generation of ultrashort laser pulses using an all-passive, fiber-ring, mode-locked laser with at least two passive spectral filters incorporated. Also presented is a full theoretical model of the operation of the laser. I report on the development and the comprehensive characterization of a fully optimized laser configuration, finding excellent agreement of the theoretical model and the experimental results. Various practical configurations and their application were demonstrated. During the period of the project, a fully commercially developed laser scheme was implemented in a variety of IPG Photonics picosecond and femtosecond laser systems.

Acknowledgments

My biggest thanks goes to my scientific supervisor Valentin Gapontsev who actually made me a laser scientist and taught me the right development techniques.

Also, my big note of thanks goes to Prof. Roy Taylor, who was kind enough guide me through the PhD process. Without his guidance, knowledge and help I may have had a lot more problems on my way.

My thanks are also given to all the members of the group, both past and present, whose support, knowledge and friendship throughout my time here has been invaluable.

Many thanks goes to my college Dr. Andrey Bordenyuk who participated in the concept development and in many theoretical and practical discussions. He has also taken huge responsibility in the implementation of the results into the various IPG products.

Thanks to Dr. Vadim Lozovoy who implemented the theoretical model into the computer simulation tools.

Also, thanks to Dr. Dmitry Pestov and Dr. Anton Ryabtsev for help with ultrafast measurements and developing MIIP based compressor.

Overview

This thesis is organized as follows.

In chapter 1, an overview of all the essential components and techniques as well as the basic physics and technology required for describe and understand the construction and characterization of this new laser concept are presented.

Chapter 2 then contains a brief analysis of existing technologies of femtosecond laser sources and discusses major advantages and disadvantages of different laser configurations.

Chapter 3 is devoted to the description and explanation of the concept of the new “Cross Filter” (CF) mode locking technique. This Chapter also describes the configuration and performance of the CF assembled for initial investigation. Additionally, the startup technique and conditions are discussed.

In Chapter 4 a comprehensive theoretical model of the laser is provided. The basic parameters of the algorithm providing stable, reproducible results of laser operation are reported. Also demonstrated is very good correlation of simulation results and experimental performance.

Chapter 5 Experimentally reports the versatility of the oscillator, demonstrating transform limited (TL) operation and femtosecond pulse shaping on demand. The control of the outputs was also demonstrated with the use of the booster-amplifier and the optimal results are presented.

Chapter 6 contains conclusions and the major results of this project.

Contents

List of Figures 9

1 Introduction 16

1.1 Propagation of light in a transparent homogeneous dielectric medium. 17

1.2 The propagation of light in a fiber light waveguide. 19

1.3 Nonlinear interaction of light with the propagation medium. 21

1.3.1 Self phase modulation and Cross Phase Modulation 22

1.3.2 Four wave Mixing 24

1.3.3 Stimulated Raman scattering. 26

1.3.4 Brillouin scattering. 28

1.4 Amplification of light in a fiber. 28

1.5 Optical fibers 31

1.6 Fiber Optic Isolator 33

1.6.1 Polarization-dependent isolators (LP) 34

1.6.2 Polarization-independent isolators IS/PM) 34

1.7 Diode pumped amplifier. 36

1.8 Fiber amplifier pump and amplification model. 37

1.9 Interference optical thin-film bandpass filters 40

1.10 Ultrafast pulse measurements 42

1.10.1 Autocorrelations 42

1.10.2 Autocorrelation function of field 43

1.10.3 Autocorrelation function of intensity 44

1.10.4 Comparison of autocorrelation function of field and intensity for Transform Limited (TL) and linear chirped pulses 46

1.10.5 Comparison of autocorrelation function of field and intensity for spectrally and phase asymmetrical pulses 48

1.10.6 Examples of strongly distorted pulses 49

1.10.7 SPIDER 51

1.10.8 FROG and MIIPS 52

1.10.9 Fidelity 56

2 Technological Landscape 62

3 The concept of the new Cross Filter mode locking technique 69

3.1 The basic configuration of laser under research 69

3.2 Laser start-up 76

3.3 Seed laser tests in configuration with stretcher and compressor. 78

4 Modeling of Cross-filter Femtosecond Fiber Laser. 84

4.1 Schematic of the laser 84

4.2 Theoretical model of the pulse propagation. 85

4.2.1 Main equation 85

4.2.2 Fourier method of solution of equation. 87

4.3 Model of linear dissection of the cavity. 89

4.4 Spectral and phase characteristics of the laser components. 90

4.5 Control of B -integral. 92

4.6 Optimization of the filters in the cavity. 95

4.7 Laser generation stabilization. 96

4.8 Calculation of field intensity in time domain. 97

4.9 Starting of the laser. 98

4.10 Stability of single and double pulsing. 99

4.11 “Shelves” of extra stability of laser generation. 101

4.12 Validation of the model on existence of the “shelves” 103

5 Ultrashort femtosecond pulses setup. 106

5.1 Targets 106

5.2 Master oscillator 108

5.3 Two-stage compressor 110

5.4 Pulse Compression and Shaping 112

5.5 Booster-converter. 116

5.6 Booster – converter test results. 118

6 Conclusions. 123

7 References 125

8 Acronyms 138

9 List of publications: 141

List of Figures

Figure 1-1 Representative loss spectrum of silica fiber highlighting the principal contributions. 17

Figure 1-2 Schematic of the transmission of light in an optical fiber due to total internal reflection and the acceptance angle. 19

Figure 1-3 Fundamental mode fiber cross-section field distribution in a standard step-index fiber. 21

Figure 1-4 A picosecond Gaussian pulse and associated self-phase modulation SPM induced frequency chirp across the pulse. 23

Figure 1-5 Sample of spectrally broadened Gaussian pulse due to SPM effect. Silica fiber 1m, 6.5µ MDF, λ=1025 nm, Pin=5nJ, Tin=1pS. 24

Figure 1-6 Schematic of the process of four wave mixing with two pump frequencies ω_1 and ω_2 generating two new frequencies ω_3 and ω_4, the signal and the idler 24

Figure 1-7 Simulation of the process of four wave mixing 25

Figure 1-8 Normalized Raman gain in silica glass. 27

Figure 1-9 Schematic of the energy level scheme of the Yb3+ ion, showing the excitation (absorption) and emission processes. 29

Figure 1-10 Emission and absorption cross-section in our Yb-doped SiP core fiber. 30

Figure 1-11 Photograph of the cross-section of a “PANDA” type optical fiber where: 1 - core, 2 - fluorosilicate shell, 3 - stressing element, 4 - technological quartz shell, 5 - primary polymer coating, 6 - secondary polymer coating. 32

Figure 1-12 Construction of our LP (linear polarized or polarization dependent) and IS/PM (isotropic state or polarization maintained) isolators. 35

Figure 1-13 Schematic of the double cladding pumping 36

Figure 1-14 Calculations Left and Right, Forward and backward pumping respectively, Bi-integrals were calculated for input pulse parameters are presenting in the laser under research. 39

Figure 1-15 One layer of thin-film interferometric filter. 40

Figure 1-16 Transmission, group delay and phase shift for two types of filters used in our system. 41

Figure 1-17 Simple configuration of field autocorrelator. 42

Figure 1-18 Typical intensity autocorrelation configuration..44

Figure 1-19 Gaussian pulse I(t)=exp($-t^2/\tau^2$) with Full Width Half Maximum 15 fs in the time domain (τ=9fs). Left column is for a transform limited (TL) pulse (no phase distortion), right is for a pulse chirped with a linear phase distortion $\phi(\omega)=(\tau\omega)^2$ in the frequency domain. First row shows the spectra (black) and Group Delay Dispersion $d\phi(\omega)/d\omega=2\tau\omega$ for a chirped pulse. The second row is the intensity and the electric field strength (normalized on max). The third row is the interferograms (see formula 7). The fourth row is the SHG non-collinear autocorrelation (see formula 12)...47

Figure 1-20 Left column is a TL pulse (no phase distortion), right is for a pulse with cubic chirp. The first row is the spectra (black) and the Group Delay Dispersion ($d\phi(\omega)/d\omega$) (red). The second row is the intensity and the electric field strength (normalized on max). The third row is the interferograms (see formula 7). The forth row is the SHG non-collinear autocorrelation (see formula 12). 48

Figure 1-21 The pulse generated by our laser (model). The top row is the uncompensated pulse and its ACF, middle row the theoretical fully phase compensated pulse, bottom row pulse with compensation of smoothed phase distortion. Note: Uncompensated pulse picosecond pulse duration with linear rising and sharp end and some tail. Compensated pulse has long tail...50

Figure 1-22 Typical SPIDER configuration..51

Figure 1-23 Typical FROG configuration...52

Figure 1-24 Typical MIIPS configuration. 52

Figure 1-25 Left columns are FROG, and right are MIIPS traces. The first row is the analysis of the pulse with a complex spectrum and no phase distortion (TL pulse). The second row is a pulse with linear chirp. 1. Spectrum and a) phase $\phi(\omega)$ b) GDD= $d\phi(\omega)/d\omega$ c) local chirp $=d^2\phi(\omega)/d\omega^2$. 2 FROG trace, 4. MIIPS trace and line corresponding to local chirp 54

Figure 1-26 Left columns are FROG, and right are MIIPS traces. The first row is the analysis of a pulse with a complex spectrum and positive (left) and a negative (right) cubic phase distortion ($d^3\phi(\omega)/d\omega^3$). 1. Spectrum and a) phase $\phi(\omega)$ b) GDD= $d\phi(\omega)/d\omega$ c) local chirp $=d^2\phi(\omega)/d\omega^2$. 2 FROG trace, 4. MIIPS trace and line corresponding to local chirp 55

Figure 1-27 Homogeneous fidelity, when all pulses in measuring the SHG as a function of the chirp are identical. First row is the case of periodical spectral distortion, second row is the case of periodical phase distortion. 59

Figure 1-28 Inhomogeneous fidelity, when all the pulses used to measure the SHG as a function of chirp are different. First set is the case of periodical spectral distortion with different phases, second set is the case of periodical phase distortion with different 60

Figure 1-29 Fidelity, when calculation were carried out using distorted spectrum (first set) or additional uncompensated cubic distortion (second set) 61

Figure 2-1 Configuration of a fiber laser mode locked using nonlinear polarization rotation 64

Figure 2-2 Configuration of a NOLM(A) and NALM(B) 65

Figure 2-3 (a) Schematic of a passively mode locked fiber laser incorporating a SESAM and (b) the reflection/absorption profile associated with a SESAM for operation in the 1060 nm spectral region.....................................67

Figure 3-1 A schematic of the proposed fiber laser configuration...................................69

Figure 3-2 Principal architecture of laser under the investigation and pulse evolution during transient “unsaturated broadening” stage. 71

Figure 3-3 Schematic of the “laser initiation” excitation pump pulse profile 77

Figure 3-4 Examples of the laser output spectra under high (left) and low (right) pump intensity. 79

Figure 3-5 Spectrum and pulse temporal waveform after stretching the pulse with a Fiber Bragg Grating (FBG). Left: spectrum reflected by FBG. Right: waveform of pulse stretched by FBG. 80

Figure 3-6 Output pulse train stability. RMS < 0.3%, P-to-P < 2%...................................81

Figure 3-7 Autocorrelation, indicating a square pulse, FWHM 10 ps. 81

Figure 3-8 Spectral replica of band pass filter coupled out of cavity after the filter. 81

Figure 3-9 Pulse shaping using MIIPS methodology and a FemtoJock pulse shaper. The fraction of the output spectrum selected for shaping (left), autocorrelation of the shaped pulse (right) having FWHM=135 fs when

Gaussian calibration is applied or FWHM=200 fs for square pulse calibration. 83
Figure 4-1 Schematic of the CFF laser. 84
Figure 4-2 Left hand column illustrates the dependence of the population of the excited states in RA and BA (red and blue amplifiers) normalized, along the fiber in meters. The right hand column displays the pulse energies along the cavity in meters, Black – experimentally measured, Red – calculated. 89
Figure 4-3 Spectral properties of laser' components. 1. Red – absorption and blue – stimulated emission spectra of Yb doped fiber. 2 – Group Delay Dispersion (GDD) of fibers. 3- Transmission and GDD of isolator, 4 Transmission of couplers, 5 – Gdd of couplers. 6,7,8 – measured transmission and GDD of filters. 90
Figure 4-4 General Parameters used in the model. 91
Figure 4-5 Three upper rows illustrate the dependence of the population of the excited state of Yb, the energy of the pulse (nJ) at each point along the fiber and the maximum value of time-dependent Bi integral along the fiber. The two lower panels present on the left, the calculated spectra (in the wavelength domain) and on the right, the Bi-integral (in the time domain). 92
Figure 4-6 Spectral intensity of the pulse (Z - log scale) along the length of the cavity (Y), X axis is wavelength in nanometers. 93
Figure 4-7 Comparison of calculated (red) and measured (black) spectra at the output of the cavity. 94
Figure 4-8 Laser cavity composition. 95
Figure 4-9 Optimization of the additional RG filter to improve output spectrum. 95
Figure 4-10 Lock of generation on blue filter. 96
Figure 4-11 Optimization of red amplifier 96
Figure 4-12 Calculation of spectra, intensity and autocorrelation of the optimized and compressed pulses. Left figure : blue – spectrum, black – group delay and red – smoothed GDD (using 2 nm resolution); Right figure: Displays the temporal profile of the pulse , red, compressed by removing smoothed GDD, blue using fully compensated phase (no phase distortion). 97

Figure 4-13 Calculation of the development of the laser pulse in the cavity. Left figure is the time dependence of output energy of the pulse, blue – linear,in nano-Joules, red similarly but presented on a log scale. On the right hand is shown the time dependence of the population inversion in first (RA, red) and second (BA, blue) amplifiers. 98

Figure 4-14 Modeling of the suppression of double pulsing. Figures A and B. represent the energy of the pulses, after the red and blue amplifiers, lasing energy (green), solid one pulse, open – another pulse. C. pumping powers of the red and blue amplifiers...99

Figure 4-15 Modeling of pump ranges of operation and tuneability for single pulse (black) and double pulse (red) modes of operation. 100

Figure 4-16 Modeling of stable shelves and unstable intermediate regimes in laser operation. X – is time in cavity, Y – energy of output pulse. The modeling was carried out under different rates of switching-off the pumping of the second amplifier. In the top row the pumping was switched-off at zero time. In the lower panels the pumping power decreased linearly with time with different rates going from max to zero from 0.1 ms to 100 ms range. Stable operational regions or “shelves” can be seen with very unstable regions between them. 102

Figure 4-17 Demonstrating up to 6 stability “shelfs “ of laser generation. 103

Figure 4-18 Pulse stability at TSS (c) P-k to P-k stability 1.6%, RMS stability 0.24%; 104

Figure 4-19 Spectrum in the middle of the second shelf..104

Figure 4-20 Calculated spectrum of the field at the output of the laser (black, in units of nJ/nm) and associated group delay (red, in units of ps)..................105

Figure 4-21 Comparison of calculated (black) and measured (red) spectra (nJ/nm). 105

Figure 5-1 Typical output pulse characteristics for the cross-filter oscillator: (a) Experimental laser spectrum, measured with an AQ6374 optical spectrum analyzer (Yokogawa, Japan); (b) Experimental autocorrelation trace, showing 12ps ACF FWHM. The ACF profile is measured with PulseCheck autocorrelator (APE, Germany)...109

Figure 5-2 Modelling of the cross-filter oscillator using CGLE: (a) Simulated output spectrum (red curve) and group delay (green curve); (b) Simulated time-domain profile of strongly chirped output pulses. The width of the simulated ACF profile (not shown) matches the width of the experimental ACF trace in Figure 5.1(b). 110

Figure 5-3 Two-stage pulse compressor, comprising a grating pair and a folded-4f shaper with an adaptive element at the Fourier plane: M1-4, guiding mirrors; G1-3 – transmission gratings; RM – roof mirror; L – lens assembly; SLM – spatial light modulator..111

Figure 5-4 Verification of pulse compression using the two-stage compressor: (a) ACF trace for the optimized grating-pair compressor, without the 4f shaper; (b) ACF trace for compressed pulses at the system output. The theoretical limit (red curve) is calculated for the experimental output spectrum and a constant spectral phase...112

Figure 5-5 Tuning the generated pulse duration using a programmable linear chirp: (a) A Parabolic phase mask corresponding to 7000 fs^2 SOD at 1025nm, applied by the 4f shaper. The laser spectrum is shown as a reference; (b) Calculated intensity profile for 7000 fs^2 SOD at 1025nm; (c) Experimental ACF profiles for the compressed pulse (reference) and for 1900 fs^2, 3700 fs^2, and 7000 fs^2 SOD at 1025 nm. The corresponding target sech^2 pulse durations are 100 fs, 200 fs, and 400 fs, respectively. 113

Figure 5-6 Generation of pulse bursts using sinusoidal phase modulation: (a) Sinusoidal phase with amplitude 0.45π and 0.2 ps modulation “frequency” (in the spectral domain). The input laser spectrum is shown as a reference; (b) Calculated intensity profile for the sinusoidal mask described in Fig. 5.6(a); (c) Experimental ACF profiles for 0.2 ps, 0.4 ps, and 0.8 ps spacing between pulses in the burst..114

Figure 5-7 Selective two-photon excitation using programmable cubic phase: a) Cubic phase mask corresponding to -106 fs^3 TOD at 1025nm, applied by the 4f shaper. The laser spectrum is shown as a reference; (b) Calculated intensity profile for -106 fs^3 TOD at 1025nm; (c) Experimental SHG spectra for the cubic phase mask scanned across the laser spectrum from 1015 nm to 1040 nm, in 5 nm increments. The SHG spectrum of the compressed pulses is given as a reference. The spectra were acquired with AQ6374 optical spectrum analyzer (Yokogawa, Japan), configured for 0.1nm resolution...115

Figure 5-8 Booster-amplifier with nonlinear converter. BA – ytterbium amplifier 1m, BF –relatively small mode field diameter fiber 1m (operating as a nonlinear converter), BG, BE, BI, BO – feeding, isolator and output LMA fibers. 116

Figure 5-9 Input spectral FWHM 1 nm, “control fiber” diameter 6 µm, 55 nJ 117

Figure 5-10 Input spectral FWHM 1 nm, “control fiber” diameter 12 µm, 100 nJ 117

Figure 5-11 Input spectral FWHM 1 nm, “control fiber” diameter 12 µm, 528 nJ 117

Figure 5-12 Output spectrum 750 mW output power, 70 nJ. 118

Figure 5-13 Pulse ACF. 119

Figure 5-14 A screenshot of femto Pulse Master simulation software, showing the calculated time-domain characteristics of a pulse defined by the laser spectrum (top-left) and a flat spectral phase (bottom-left); time-domain electric field profile (top-middle); intensity profile, normalized to unity at the peak and zoomed down to 1% level (bottom-middle); interferometric autocorrelation (top-right) and background-free autocorrelation, normalized to unity at the peak and zoomed down to 1% level to highlight the pedestal (bottom right). 119

Figure 5-15 Fidelity calculations based on the chirp scan: (top-left) the loaded laser spectrum; (bottom-left) calculated and experimental SHG spectra for the compressed pulses; (top-middle) laser spectrum, refitted on the calculation grid; (bottom-middle) calculated and experimental SHG traces as a function of linear chirp, scanned within +/-30,000fs^2; (top-right) instantaneous SHG spectra plotted by the program for every chirp value as the spectrograms are generated; (bottom-right) Spectrally-integrated SHG signal as a function of the applied chirp, calculated and experimental; the ratio between the theoretical (blue) and experimental (red) curves gives “fidelity” curve (black). 120

Figure 5-16 Filtered spectrum 122

Figure 5-17 Improved pulse ACF 122

1 Introduction

Before proceeding directly to the description of the subject of this study it is necessary to briefly describe the physical effects, which lie at the basis of the operation of the laser system that has been developed.

To fully understand the operation of the laser, it is absolutely necessary to develop a relatively comprehensive mathematical model of the laser while the experimental results generated provide a clearer understanding of the processes involved and allow possible improvements and future developments to be suggested. However, in order to have a basic understanding of the experimental laser and the associated processes it is important that the principles of operation and the basics of the main optical components used in the laser system are briefly described. Also, knowledge of the structure and principles of operation of the various optical components are extremely important both for modeling and for understanding the results of experiments.

The basic physical principles and effects considered in this work are:

1. Propagation of light in a transparent dielectric medium.
2. Light propagation in a glass light waveguide.
3. Nonlinear interaction of light within the propagation medium, including
4. Kerr effect, self-phase modulation (SPM), cross-phase modulation (XPM), four wave mixing (FWM), stimulated Raman scattering (SRS) and stimulated Brillouin scattering.
5. Amplification of radiation in a rare earth doped fiber amplifier.

1.1 Propagation of light in a transparent homogeneous dielectric medium.

A transparent dielectric medium is characterized by the parameters such as the optical loss, the refractive index and refractive index dispersion. Silica glass is the basis of the most widely deployed fiber optic light waveguides. For silica glass used in telecommunication optical fibers at present the achieved experimental losses have almost reached the theoretical limit set by the purity of the material.

The passive losses are mainly determined by two physical effects. Rayleigh scattering through fluctuations of the glass density is responsible for the loss in the short-wavelength region of the spectrum, while multi-phonon absorption limits transmission in the long-wavelength region of the spectrum. In the region of the minimum optical loss around 1.55 µm, used in telecommunications, the overall loss reaches a value of less than 0.17 dB / km.

In the spectral range of operation of the laser described in this work, around 1 micron, the loss is typically about 1 - 2 dB / kilometer and determined mainly by the Rayleigh scattering in the glass, see Figure 1.1

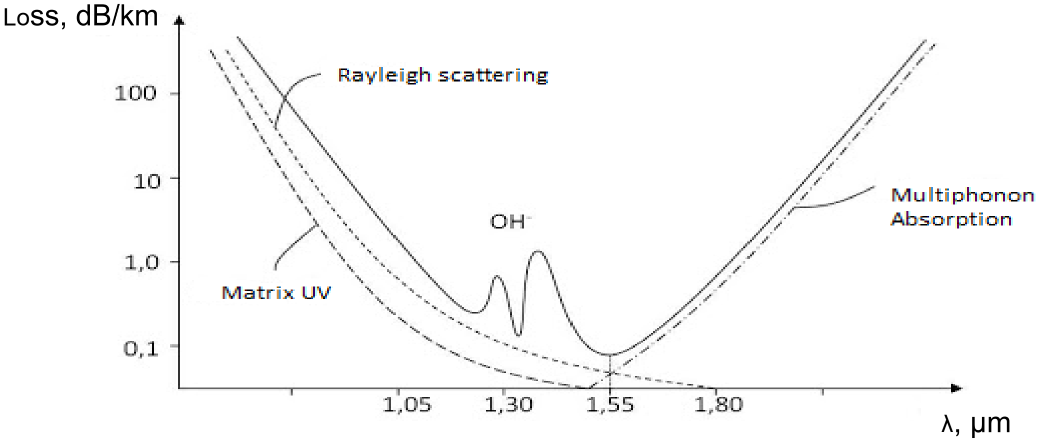

Figure 1-1 Representative loss spectrum of silica fiber highlighting the principal contributions.

The dispersion of the refractive index is due to the dependence of the absolute refractive index on the frequency of the light, or similarly the dependence of the phase velocity of light on frequency. As a rule, for the more "red" or for the longer wavelength part of the light, then the propagation velocity in the medium is a maximum and the refraction is a minimum, while for the "blue" or short wavelength part of the spectrum, the propagation velocity is a minimum, and the index refraction is maximal. Such a case is referred to as “normal” dispersion. In our laser systems, normal light dispersion takes place in silica glass at the operational wavelength around 1 micron.

The dispersion parameters are most conveniently expressed in terms of the propagation constant of light in a fiber.

$$\beta = n\frac{\omega}{c}$$, where n is the refractive index.

Since n also depends on the frequency, then

$$\beta(\omega) = n(\omega)\frac{\omega}{c}$$

This expression can be expanded in a Taylor series in the region of the operating wavelength.

$$\beta(\omega) = \beta_0 + \beta_1(\omega - \omega_0) + \frac{1}{2}\beta_2(\omega - \omega_0)^2 + \cdots,$$

In this case, β_1 will determine the group velocity of the propagating pulse and β_2 is responsible for the second-order dispersion, also called the group velocity dispersion.

It is the sign β_2 that determines the type of dispersion. If the sign of β_2 is positive, then the dispersion will be positive (normal), if negative, then anomalous [Agr08].

1.2 The propagation of light in a fiber light waveguide.

A fiber waveguide is most commonly a thin rod of circular cross-section with a refractive index profile varying over the cross-section of the fiber [San02]. A typical profile is a step-index. The principle of guiding light by total internal reflection, which underpins the operation of optical fibers, was initially demonstrated in a water fountain by Daniel Colladon in 1842 [Col42]. Due to the fact that the inner part of the fiber, the core, has a higher refractive index of light than the outer cladding, light introduced into the core with an angle less than the angle ϕ (see Fig.1.2) will propagate through the fiber, practically without loss, due to the effect of total internal reflection at the boundary of the refractive indices [Agr08].

where $\varphi = \sin^{-1}\frac{n_2}{n_1}$

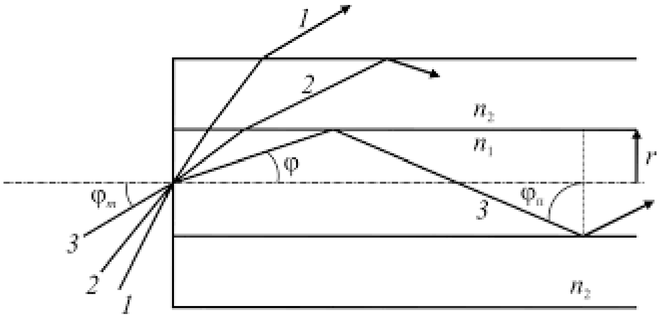

Figure 1-2 Schematic of the transmission of light in an optical fiber due to total internal reflection and the acceptance angle.

For a small difference in n_1 and n_2 , as typically takes place then,

$$\varphi \cong n_0 \sin\varphi = NA = \frac{1}{n_0}\sqrt{(n_1^2 - n_2^2)}$$

NA is the numerical aperture of the fiber and n_0 is the refractive index of the medium surrounding the fiber [Sal07], which is most commonly air and so

$n_0 = 1$

When light propagates along the fiber core, multi-beam interference occurs, which creates an interference pattern inside the fiber that corresponds to positive interference. The pattern can be divided into mode states, the so-called eigenstates of the waveguide field, which are stationary in the cross section. The number of modes in the fiber is approximately equal to the $\frac{V^2}{2}$ were V is so-could V-parameter of the fiber.

$$V = \frac{2\pi}{\lambda} a\sqrt{(n_1^2 - n_2^2)}$$

Where a is a radius of the core and λ is wavelength of propagating radiation.

If V <2.404, then only one transverse mode propagates in the fiber. Such a fiber is called a single-mode fiber. In all the laser systems described in this thesis, only single-mode fibers were deployed [Glo71].

Figure 1.3 shows an example of a fundamental mode fiber cross-section field distribution in a standard step-index fiber.

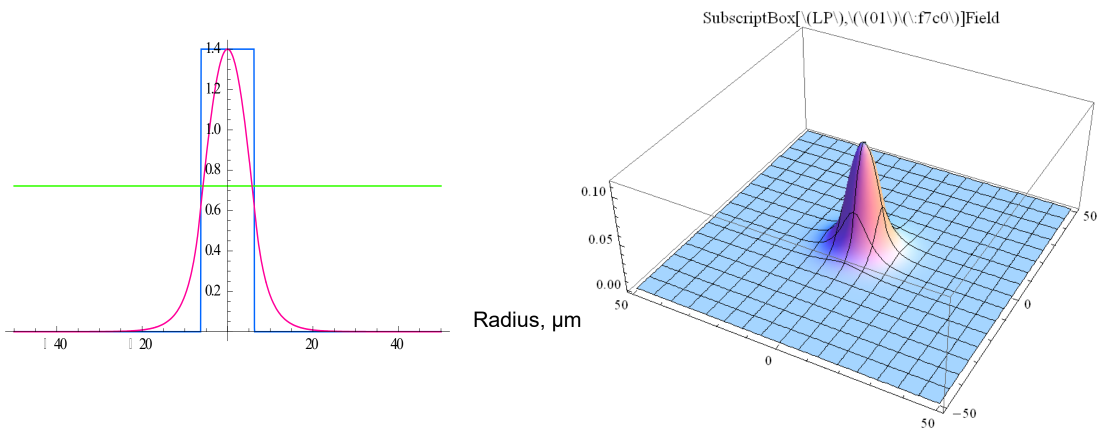

Figure 1-3 Fundamental mode fiber cross-section field distribution in a standard step-index fiber. Red - mode shape, Blue – fiber core shape, Green – FWHM.

The geometry of the waveguide also contributes to the dispersion characteristics of the fiber. This additional dispersion contribution is called waveguide dispersion and is added to the normal fiber material dispersion. As a result we deal with an effective overall dispersion. A short pulse of light propagating in a fiber receives a so-called frequency chirp as a result of the dispersion of the group velocities in the fiber, which usually leads to temporal dispersive broadening of the pulse.

1.3 Nonlinear interaction of light with the propagation medium.

Light is an electromagnetic field that creates an induced polarization in a medium. The interaction of a field with a medium is most fully described by Maxwell's equations. In the case of a transparent dielectric media such as silica glass, in which there are no free charges, the Maxwell system of equations is simplified to:

$$\nabla^2 E = -\frac{1}{c}\frac{\partial^2 E}{\partial t^2} - \mu_0 \frac{\partial^2 P}{\partial t^2}$$

where P is the polarization of the medium depending on the applied field, c is the speed of light and μ_0 is vacuum permeability. In general, polarization can be written as:

$$P(E) = \varepsilon_0(\chi_1 E + \chi_2 EE + \chi_3 EEE + \cdots$$

Where the first term χ_1 is the linear polarization response to the applied field and determines the refractive index of the medium (as well as attenuation and gain in the case of a complex value of this parameter).

The second term determines the non-linear second-order effects and is observed only in the centro-asymmetrical materials (in fact it is the induced birefringence and in the case of a static field it is responsible for the Pockels effect). When light interacts with such a medium, effects such as the generation of second harmonic, sum and difference frequencies take place. In the case of silica glass, because of the symmetry of the medium, this term can be neglected.

The third term determines the change in the refractive index due to the intensity of the radiation, the so-called Kerr effect or Kerr nonlinearity.

$$n(\omega, |E|^2) = n(\omega) + n_2|E|^2$$

1.3.1 Self-Phase Modulation and Cross-Phase Modulation

For short, high-power pulses the Kerr nonlinearity leads to two main effects.

The so-called effect of self- phase modulation (SPM) when a pulse of light acts on itself nonlinearly and cross-phase modulation (XPM) when the nonlinear effect is created by another powerful pulse overlapping in space with the investigated one.

For SPM, the nonlinear phase shift can be written as:-

$$\psi_{nl} = n_2 k_0 L I(t)$$

Where n_2 is the nonlinear refractive index, k_0 is the wavevector, L the interaction length and I(t) the intensity profile of the incident laser pulse .

This effect was first observed in optical fibers in 1978 [Sto78]

The effect of SPM is shown on Fig.1.4

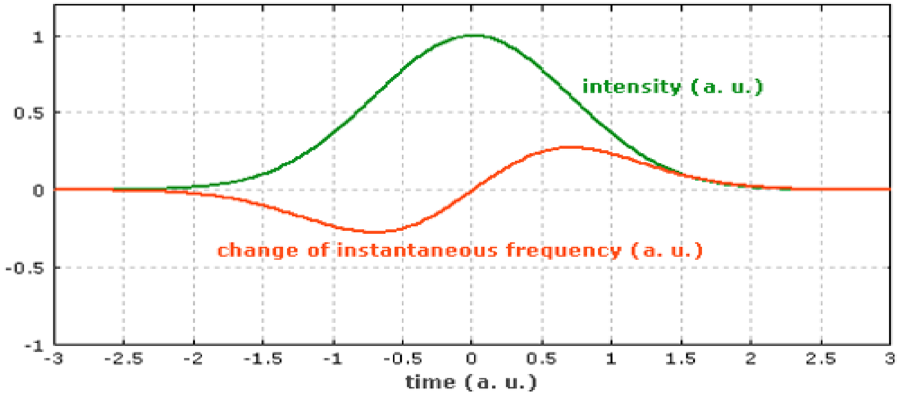

Figure 1-4 A picosecond Gaussian pulse and associated self-phase modulation SPM induced frequency chirp across the pulse.

Since this nonlinear effect introduces phase changes along the pulse and leads to a change and the appearance of new frequencies, this is in fact equivalent to spectral broadening of the pulse (see Fig. 1.5).

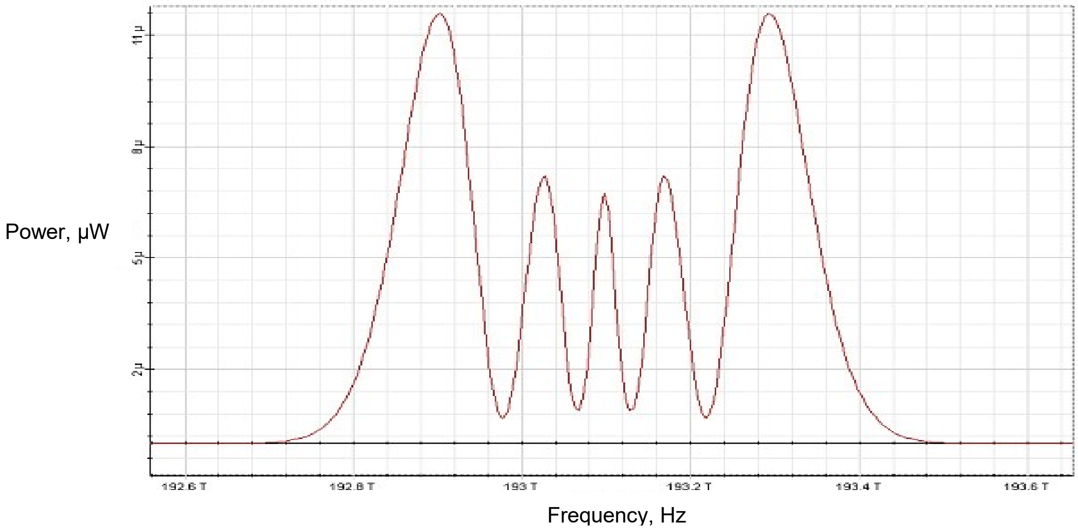

Figure 1-5 Sample of spectrally broadened Gaussian pulse due to SPM effect. Silica fiber 1m, 6.5µ MDF, λ=1025 nm, Pin=5nJ, Tin=1pS.

1.3.2 Four wave Mixing

Four wave mixing is a special case of Kerr nonlinearity, a parametric effect which takes place in the case of the presence of two pump wavelengths in the fiber, which generate two other wavelengths during nonlinear interaction (see Fig.1.6)

$$\omega_1 + \omega_2 = \omega_3 + \omega_4$$

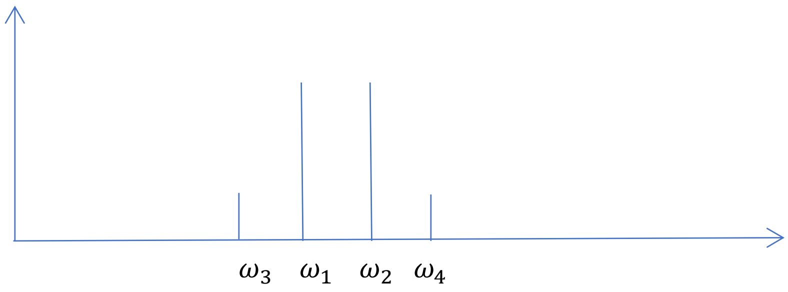

Figure 1-6 Schematic of the process of four wave mixing with two pump frequencies ω_1 and ω_2 generating two new frequencies ω_3 and ω_4, the signal and the idler

In our work, this effect was neglected and not observed as the efficiency of four wave mixing significantly reduces through using short duration broadband pump pulses.

The simplest way to understand the effect is purely mathematically, at the peaks of positive interference, the Kerr effect takes place and thus self- phase modulation which changes the shape of the quasi pulse (see Figure 1.7)

In the case of a Fourier transformation, this is equivalent to the formation of harmonics with frequencies

$\omega_3 = \omega_1 - \Delta\omega$ and $\omega_4 = \omega_2 + \Delta\omega$ where $\Delta\omega = \omega_2 - \omega_1$

E1+E2 = $\cos\omega_1 t + \cos\omega_2 t$

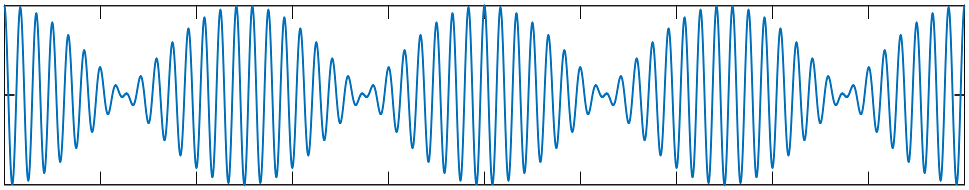

$\cos\Delta\omega t/2 * \cos(\omega_1 + \omega_2)t\,/2$

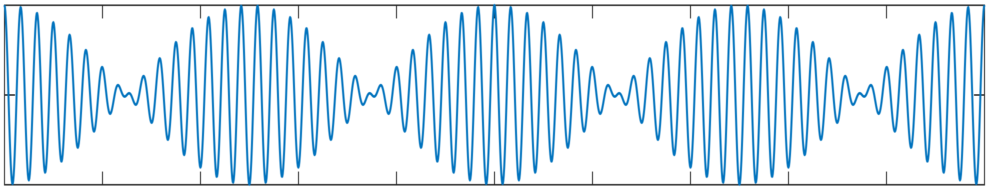

$(\cos\Delta\omega t/2)^2$

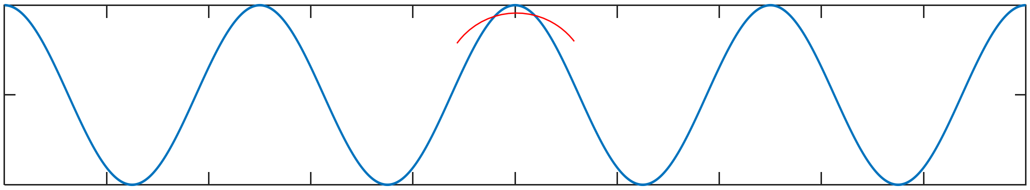

Figure 1-7 Simulation of the process of four wave mixing. Red is nonlinear distortion.

The FWM effect in optical fiber was first observed in 1974 [Sto74]

In high-power CW fiber lasers, where there are a large number of cavity longitudinal modes, the four-wave mixing effect plays a dominant role in broadening the laser radiation spectrum.

In our case of a pulsed laser with ultrashort pulses, the spectrum is continuous, physical longitudinal modes are absent, and the effect can be neglected.

1.3.3 Stimulated Raman scattering.

In contrast to the above effects, in the case of Raman scattering [Ram28], the light interacts not with the electron cloud’s induced dipoles, but with the dipoles of the atomic or molecular vibrations in a medium. Raman scattering of light is scattering by the optical phonons of the medium. Optical phonons are vibrations of atoms in a lattice or in a molecule in which neighboring atoms always move in opposite directions like weights on springs, in contrast to Brillouin scattering by acoustic phonons, in which a neighboring atom always moves in one direction.

Vibrations of atoms create an oscillating dipole moment (or we can talk about oscillations of the refractive index) which interacts with the radiation field and leads to the formation of a new field with a frequency equal to

$$\omega_1 = \omega_0 - \omega_R$$

The difference energy is transferred to the thermal vibrations of the medium.

If two beams, a pump beam and a signal beam, are launched into the fiber, so that the signal beam will be amplified due to the transfer of energy from the pump with the exchange of a part of the energy for the excitation of optical phonons.

$$K_a = e^{pK_R l}$$

Where p is the pump power density

K_R is the Raman coefficient

l is the interaction length

The Raman gain spectrum for silica is shown in Fig1.8 [Hol02]

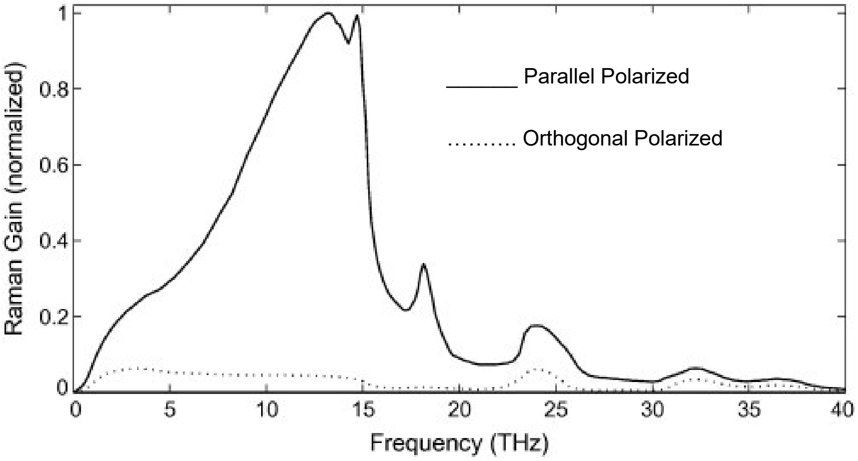

Figure 1-8 Normalized Raman gain in silica glass.

SRS was first observed in optical fiber in 1972 [Sto72].

Raman amplifiers are widely used in telecommunications [Isl02] and for conversion of laser sources to other wavelength [Sto72].

The results of our simulations and experiments, which will be described below, show that SRS, although insignificant, affects the spectral characteristics of our laser, mainly on the tail of the long-wavelength part of the laser pulse spectrum. The Raman Effect is taken account of in our model.

1.3.4 Brillouin scattering.

As mentioned earlier, Brillouin scattering is the scattering by acoustic phonons. Stimulated scattering is the case of effective backscattering from an acoustic traveling wave (coherent Bragg scattering) in which the frequency of the scattered backward wave obeys the Doppler Effect.

$$\omega_1 = \omega_0 - \omega_B$$

Where $\omega_B = \frac{2\pi V_S}{c}$ and V_S is the speed of sound in the medium. The Brillouin frequency shift ω_B is typically 10-20 GHz with less than 100 MHz bandwidth [Agr08]. SBS is a very important effect for very narrow laser lines and extended interaction lengths (long fibers) however, within the context of the short pulse, broad bandwidth lasers developed and reported in this thesis, the effect is negligible.

1.4 Amplification of light in a fiber.

Fiber light amplifiers are usually doped fiber amplifiers. It is based on the stimulated emission effect. Typically, the gain medium is a glass fiber doped with rare earth ions such as Er, Yb, Tm, and others [Sni61b]. The first fiber amplifier was demonstrated by C.J.Koester and E.Snitzer in1964 [Koe64].

Fiber amplifiers were not in demand until the second half of the eighties when erbium-based amplifiers became key components of the booming telecommunications industry [Mea87] and the demonstration that they could be efficiently pumped by semiconductor diode lasers.

The next fundamental leap forward in fiber amplifier applications came in the early nineties when ytterbium-doped fiber amplifiers became the backbone of the entire fiber laser industry and has dominated the laser market ever since

[Han88]. For pumping amplifiers, as a rule, semiconductor diodes with a fiber output are used. In high-power laser systems, pumping is carried out by high-power multimode laser diodes using various variations of the so-called double-clad technology [Sni88].

In the practical schemes described in this thesis, for amplification in the region of one micron, we use fibers doped with Yb^{3+} ions and pumped by a semiconductor diode at a wavelength of 960 nm. The energy level diagram of the Yb^{3+} ions is shown in Figure 1.9

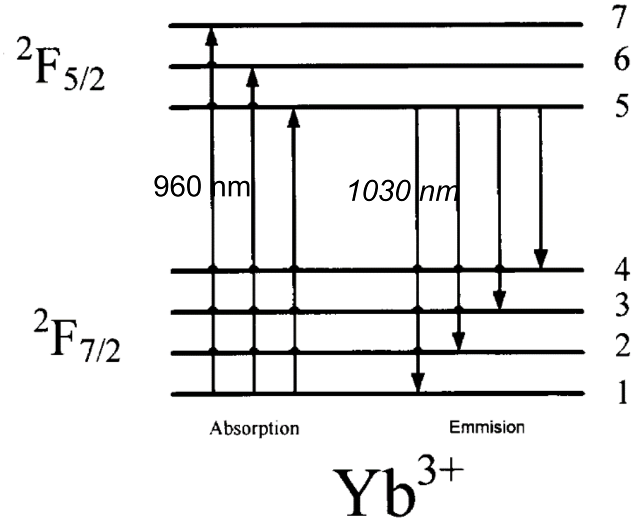

Figure 1-9 Schematic of the energy level scheme of the Yb3+ ion, showing the excitation (absorption) and emission processes.

The transitions occur between two levels with strong Stark splitting. Due to the fact that there are many Stark sublevels which are closely spaced, the transitions turn out to be very broad spectrally and practically uniformly broadened.

Under the action of pumping due to the absorption of radiation at a wavelength of 960 nm, ytterbium exhibits transitions from the lowest sublevel of the lower level ($F_{7/2}$) to the upper sublevels of the upper energy level ($F_{5/2}$). Further, due to the thermal interaction, rapid thermalization takes place within the upper sublevels of the upper level, relaxing rapidly to the lower sublevel of the upper manifold in times of the order of a picosecond. The lifetime of the excited state of the upper metastable energy level in silica glass is on the order of 1 millisecond.

When a signal with a wavelength falling into the amplification band passes through the excited medium, ytterbium ions pass from the upper metastable level to the lower level with energy transfer in the form of radiation at the signal wavelength. Thus, the signal emission in the fiber amplifier is amplified.

$\Delta I_s = I_s(g_e n_2 - g_a n_1)\Delta L$, or

$I_s = I_{s0} e^{(g_e N_2 - g_a N_1)L/S}$,

Where g_e – emission cross-section

g_a – absorption cross-section

n_2 – upper level population density

n_1 – lower level population density

L –length of fiber

S – fiber core cross-section

N1 - total number of Yb ions on the lower level

N2 - total number of Yb ions on the upper level

The emission cross-section and absorption cross-section in SiP fiber is shown in Fig.1.10

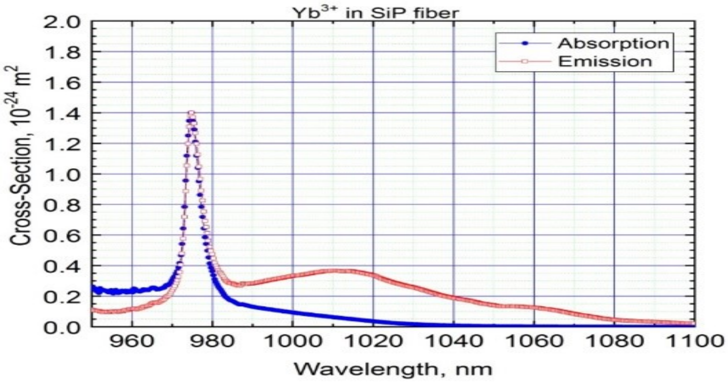

Figure 1-10 Emission and absorption cross-section in our Yb-doped SiP core fiber.

1.5 Optical fibers

In our experiments to be described later, we used polarization-maintaining fibers (PANDA type).

In a conventional single-mode fiber with a circular cross-section of the core and an axisymmetric distribution of the refractive index, two orthogonally polarized modes HE_{11} propagate, which are usually denoted HE_{x11} and HE_{y11}. When one of these modes is introduced into the fiber, the state of its polarization changes due to the transformation into an orthogonal mode under the influence of external factors: pressure, temperature, vibrations, etc. Therefore, optical fibers exhibit birefringence as the two polarisation axis modes have different propagation constants [Pas08]. Consequently, linearly polarized radiation becomes elliptically polarized. The transfer of light energy from one mode to another is due to the fact that they are degenerate, that is, their propagation constants βx and βy are the same. The state of polarization of the radiation can be preserved if the symmetry of the shape or refractive index of the core is broken. In this case, βx and βy will differ, limiting the degree of transformation of orthogonal modes. Optical fibers of this type are called anisotropic single-mode fibers. Geometric anisotropy is created by the transformation of the round shape of the core into an elliptical one, and the anisotropy of the refractive index is generally provided by the orthogonal orientation of stresses when using materials with different coefficients of thermal expansion.

The mode birefringence B, is a measure of the anisotropy of such a fiber:

$B = (\beta x - \beta y)/(2\pi/\lambda)$ Is the birefringence $\Delta B = B_x - B_y = 2\pi/\lambda\ (n_x - n_y)$

But $\Delta\phi = \Delta BL = 2\pi$ from which $(n_x - n_y) = \lambda/L$

Which is calculated on the basis of measuring the beat length (Lb) of orthogonal modes (the length at which the phase incursion of the polarization modes is 2π).

$B = \lambda / Lb$.

The shorter the beat length, the greater the birefringence and therefore the less the coupling between the polarization modes. The fraction of the power of linearly polarized radiation Px introduced into the fiber, which has passed into the orthogonal (parasitic) mode Py, is characterized by the attenuation coefficient η:

$$\eta = 10 \log (Py / Px) = 10 \log (hL)$$

Where h is the degree of conservation of polarization of the radiation, L is the length of the fiber. It follows from this equation that:

$$h = (Py / Px)/L$$

An optical fiber of the "PANDA" type is a special optical fiber that preserves the polarization of the polarized radiation introduced into it due to high birefringence (BR). In PANDA type fibers, birefringence occurs due to the stress anisotropy caused by the structure of the fiber, in particular, through "stressing" elements made of borosilicate glass. A photograph of the end of a typical "PANDA" type optical fiber is shown in Fig.1.11

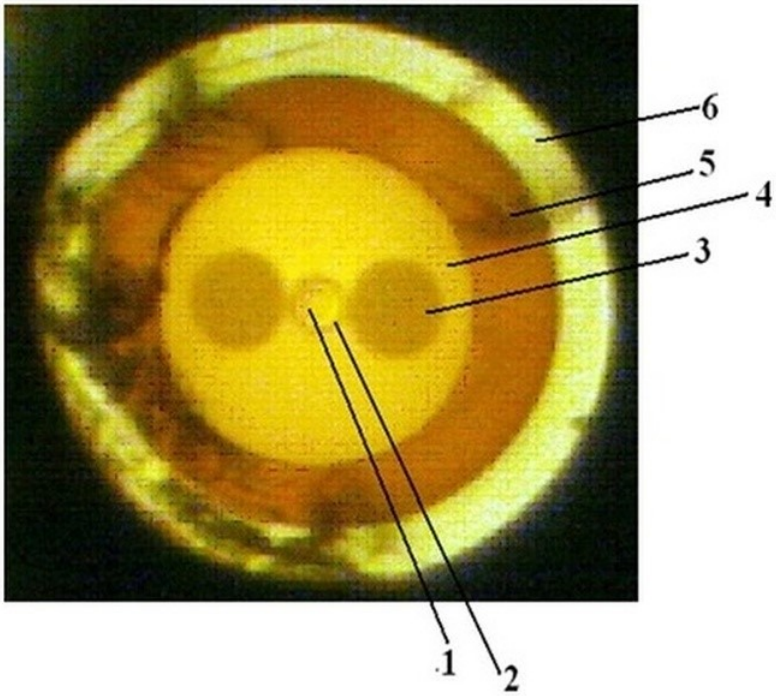

Figure 1-11 Photograph of the cross-section of a “PANDA” type optical fiber where: 1 - core, 2 - fluorosilicate shell, 3 - stressing element, 4 - technological quartz shell, 5 - primary polymer coating, 6 - secondary polymer coating.

The fiber consists of a round core formed by pure silica glass or germanium-silica glass. The core is surrounded by a reflective depressed shell of fluorosilicate glass deposited inside the support tube by MCVD.

The typical parameters of optical fibers of the PANDA type are :-

- Losses are ≤ 3 dB / km at λ = 1.06 μm,
- Runout (beat) length ≤ 1.5 mm at λ = 1.06 μm,
- Value of coupling of polarization modes (h-parameter) $(6 \div 8) \times 10^{-6}\ m^{-1}$

The use of polarization-maintained fiber in our laser avoids the parasitic effect of polarization mode dispersion. Unlike conventional chromatic dispersion, PMD is very difficult to compensate for.

1.6 Fiber Optic Isolator

The fiber optic coupled optical isolator is a key element in the systems incorporating a fiber optic amplifier. An isolator is actually a unidirectional valve that allows light to pass through in one direction and blocks its propagation in the opposite direction, the operation of which is based on the magneto-optical Faraday Effect.

In 1842, Faraday discovered that the plane of polarization of radiation rotates as it propagates through optically inactive substances that are in a magnetic field [Far48]. The direction of rotation depends on the direction of the magnetic field and does not depend on the direction of propagation of light. Optically inactive substances under the action of an external magnetic field acquire the ability to rotate the plane of polarization of linearly polarized light propagating along the direction of the field and optical materials become optically active. The angle of rotation of the plane of polarization θ is proportional to the thickness of the substance layer through which the linearly polarized monochromatic radiation L [cm] passes and the strength of the external longitudinal constant magnetic field H, the Verdet constant V [min / Oersted · cm].

$\theta = L \times H \times V$

The structure of the optical isolator includes an input polarizer, a Faraday cell with a magnet, and an output polarizer.

1.6.1 Polarization-dependent isolators (LP)

The construction of a polarization-dependent isolator is shown in the upper figure of Fig. 1.12. For forward propagation of light let us assume that the polarizer at the input transmits only radiation whose polarization plane is vertical, that is, the angle of rotation of the intensity vector E is equal to zero (0 °). Radiation, polarized or unpolarized, passing through the polarizer becomes linearly polarized. The Faraday cell will rotate the plane of polarization 45 ° clockwise, and light will exit the isolator through a polarizer that transmits light whose plane of polarization is rotated 45 °, relative to the plane of polarization of the input polarizer. In the backward propagation of light through an isolator, light will pass through the output polarizer, which transmits light with polarization rotated 45 ° relative to the plane of the input polarizer, then the light passes through the Faraday cell and the plane of polarization will rotate another 45 ° clockwise. Thus, the plane of polarization will be rotated by 90 ° relative to the transmission plane of the input polarizer. As a result, light will be reflected or absorbed.

1.6.2 Polarization-independent isolators IS/PM)

In this case, referring to the bottom figure of Fig.1.12, for forward propagation of light in a polarization-independent fiber-optic isolator, the input light is split into two beams using a birefringent crystal. The Faraday cell and half-wave plate (SiO_2) rotate the polarization of the light in each beam before they enter the second birefringent crystal, at the exit from which they combine into one beam. Light propagating in the opposite direction will hit the second birefringent crystal and will be split into two beams, the polarization of which will correspond to the states of polarization in the beams propagating in the forward direction. The Faraday cell is a nonreciprocal optical element, so it will eliminate the polarization rotation that a half-wave plate introduces. When the light passes through the input birefringent crystal, the beams are diverged in such a way that they do not pass through the collimating lens and do not enter the optical fiber.

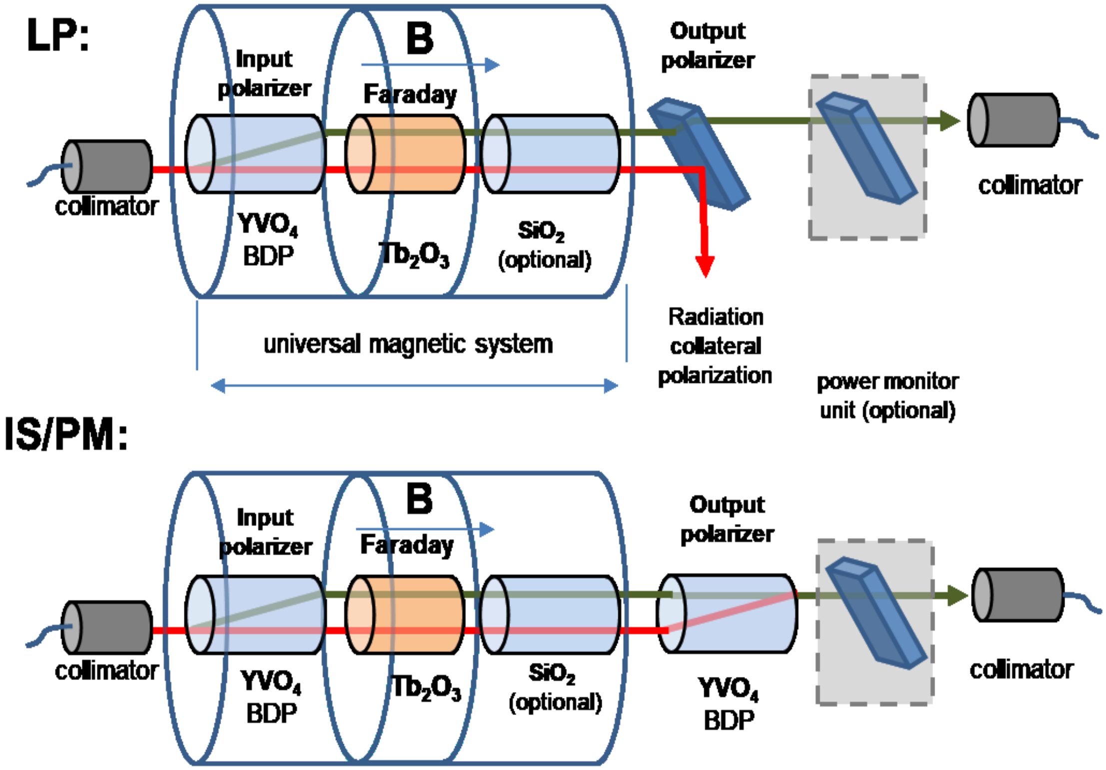

Figure 1-12 Construction of our LP (linear polarized or polarization dependent) and IS/PM (isotropic state or polarization maintained) isolators.

The typical parameters of the isolators are deployed in our laser systems are:

Insertion loss 0.7-1.2 dB

Return loss 28-38 dB in operation spectral range

Pulse dispersion less than 50 fsec (chromatic)

1.7 Diode pumped amplifier

In our laser systems that will be described later, we use Yb-doped fiber amplifiers pumped by multimode high power semiconductor laser diodes (SLD). The pump configuration is that of a double fiber, double-clad. This means that the two fibers are in optical contact and are both covered with the same reflective polymer cladding as in a standard double-clad pumping. One of the fibers is a multimode fiber through which the pump radiation is coupled into an amplifier, and the other is a fiber with an ytterbium-doped single-mode core Fig.1.13.

When the pump from a high-power multimode diode enters the pump fiber, due to the optical contact, it penetrates into the doped fiber and is absorbed in the core. A common reflective cladding maintains the pump radiation inside the fiber along its entire length.

The distribution of the amplification along its length significantly affects the parameters of the fiber laser. The key question is, does the amplifier induce nonlinearity of the propagating pulse or only effects the amplitude of the pulse with no penalty?

In order to take this effect into account, a separate mathematical model of the amplifier operation was developed and its results are taken into account in the lasing model.

Below you can see description of the amplifier model.

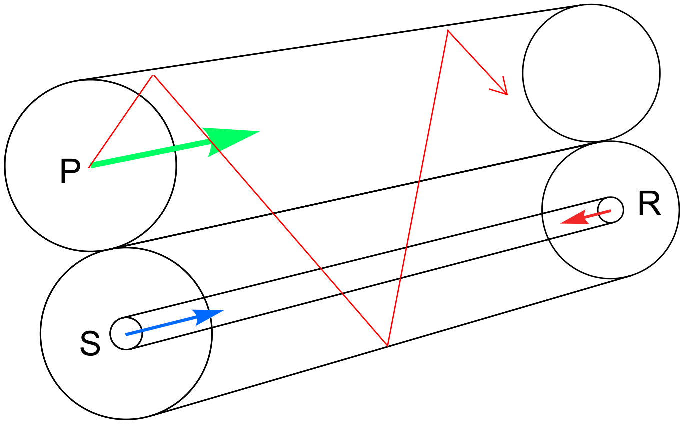

Figure 1-13 Schematic of the double cladding pumping

1.8 Fiber amplifier pump and amplification model.

We consider pumping of the upper, large fiber with diameter d_p [m] using power P_p [Watt] at wavelength λ_p [m] to amplify a signal in the core fiber of diameter d_s [m] at wavelength λ_s [m] along the length z [m]. The amplified signal has a spectral density $P_s(\lambda)$ with power $P_s = \int P_s(\lambda)d\lambda$ [Watt], The concentration of Yb doping n_{Yb} = ppm×6×10^{22} [m^{-3}]. The intensities of the pump and signal are $I_p=P_p/A_p$ and $I_s=P_s/A_s$ [$\mathrm{W/m}^2$], the photon flux $F_p=P_p/h\nu_p/A_p$ [photons/m^2s], where the area $A_p=2\pi r_p^2$, and $F_s=P_s/h\nu_s/A_s$, and where area $A_s=\pi r_p^2$. The area of pump is $2\pi r_p^2$ because the pump is distributed over two fibers and the photon energy $h\nu_p=hc/\lambda$ [Joule]. To have numbers in the equation small we multiply using the dopant concentrations $\underline{Y}_p=F_p/n_{Yb}$ and $\underline{Y}_s=F_s/n_{Yb}$ [m/s]. The cross-sections of absorption and stimulated emission of the pump light are σ_{gp} and σ_{ep} and the absorption and stimulated emission are $\sigma_{gs}(\lambda)$ and $\sigma_{es}(\lambda)$ [m^2]. It is more convenient in our calculations to use gain parameters $a_{gp}=\sigma_{gp}n_{Yb}$, $a_{ep}(\lambda)=\sigma_{ep}(\lambda)n_{Yb}$, $a_{gs}=\sigma_{gs}n_{Yb}$, $a_{es}(\lambda)=\sigma_{es}(\lambda)n_{Yb}$ [1/m].

The dynamics in time and space are described as a solution of a partial differential equation, where n_g and n_e are the population of ground and exited states and $n_g+n_e=1$. The numbers c_p and c_s are group velocity of light in the media, and are not used in the case of stationary conditions. The ratio A_s/A_p appears because the pump power P_p is spread over area A_p but interact with dopant in an area A_s. Forward and backward pumping is $P_p^{\pm}$

$$\pm\frac{\partial P_p^{\pm}(z,t)}{\partial z}+\frac{\partial P_p(\lambda,z,t)}{c_p\,\partial t}=\frac{A_s}{A_p}\Big(\sigma_{ep}n_e(z,t)-\sigma_{gp}(\lambda)n_g(\lambda,z,t)\Big)n_{Yb}P_p^{\pm}(z,t)$$

$$\frac{\partial P_s(z,t)}{\partial z}+\frac{\partial P_s(\lambda,z,t)}{c_s\,\partial t}=\Big(\sigma_{es}n_e(z,t)-\sigma_{gs}(\lambda)n_g(z,t)\Big)n_{Yb}P_s(\lambda,z,t)$$

$$\frac{\partial n_e(z,t)}{\partial t}=\left(\frac{\sigma_{gp}}{A_p}\frac{P_p^{\pm}(z,t)}{h\nu_p}+\frac{\sigma_{gs}}{A_s}\frac{P_s(\lambda,z,t)}{h\nu_s}\right)n_g(z,t)-\left(\frac{\sigma_{ep}}{A_p}\frac{P_p^{\pm}(z,t)}{h\nu_p}+\frac{\sigma_{es}}{A_s}\frac{P_s(\lambda,z,t)}{h\nu_s}+\frac{1}{\tau_f}\right)n_e(z,t)$$

$$n_g(z,t)=1-n_e(z,t)$$

In the case of stationary conditions when spatial profiles are stabilized $\frac{\partial}{\partial t}=0$ we can rewrite these semi-explicit nonlinear differential equations in terms of normalized flux of photons.

$$\pm\frac{dY_p^{\pm}(z)}{dz} = \frac{A_s}{A_p}\left(a_{ep}n_e(z) - a_{gp}n_g(z)\right)Y_p(z)$$
$$\frac{dY_s(\lambda,z)}{dz} = \left(a_{es}(\lambda)n_e(z) - a_{gs}(\lambda)n_g(z)\right)Y_s(\lambda,z)$$
$$0 = \left(a_{gp}Y_p^{\pm}(z) + \int a_{gs}(\lambda)Y_s(\lambda,z)d\lambda\right)n_g(z) - \left(a_{ep}Y_p^{\pm}(z)(z) + \int a_{es}(\lambda)Y_s(\lambda,z)d\lambda + \tau_f^{-1}\right)n_e(z)$$
$$0 = 1 - n_e(z) - n_g(z)$$

We can simplify these equations to an ordinary differential equation with two additional semi empirical filling parameters Γ_p and Γ_p

$$\pm\frac{dY_p^{\pm}(z)}{dz} = \Gamma_p\left[a_{ep}n_e(z) - a_{gp}(1 - n_e(z))\right]Y_p^{\pm}(z)$$
$$\frac{dY_s(\lambda,z)}{dz} = \Gamma_s\left[a_{es}n_e(z) - a_{gs}(1 - n_e(z))\right]Y_s(\lambda,z)$$
$$n_e(z) = \frac{a_{gp}Y_p^{\pm}(z) + \int a_{gs}(\lambda)Y_s(\lambda,z)d\lambda}{a_{gp}Y_p(z) + \int a_{gs}(\lambda)Y_s(\lambda,z)d\lambda + a_{ep}Y_p^{\pm}(z) + \int a_{es}(\lambda)Y_s(\lambda,z)d\lambda + \tau_f^{-1}}$$

In forward pumping we know $Y_p^{\pm}(0) > 0$ and $Y_s(0) > 0$ and backward when $Y_p^{\pm}(L) > 0$ and $Y_s(0) > 0$. We used a standard Runge-Kutta 4th order method (MATLAB “ode45”).

The simulation results are shown in the Fig.1.14 below. The model contains exactly the parameters of the amplifier used in the laser.

As you can see from the figure, the efficiency, the gain and the output power depend very little on the direction of pumping, however, such an important parameter as B-integral,

$$B(z) = \int_0^z \frac{2\pi n_2}{\lambda\pi r^2}\max_t[I(t,z)]\,dz$$

which determines the SPM efficiency, differs almost by a factor of 2 and in both cases is large enough to take into account the influence of the amplifier on the pulse formation in our main model .Results of modeling of amplification of the seed signal when pumping is in the direction opposite to that of the propagation are shown below in the right hand column of Fig. 1.14.(A) shows the dependence of pump (green) and amplified pulse (black) along the fiber. (B). Gain per meter (red) and accumulated nonlinear phase (blue) for 1 ps pulse. (C). Population on ground (red) and excited states (blue).

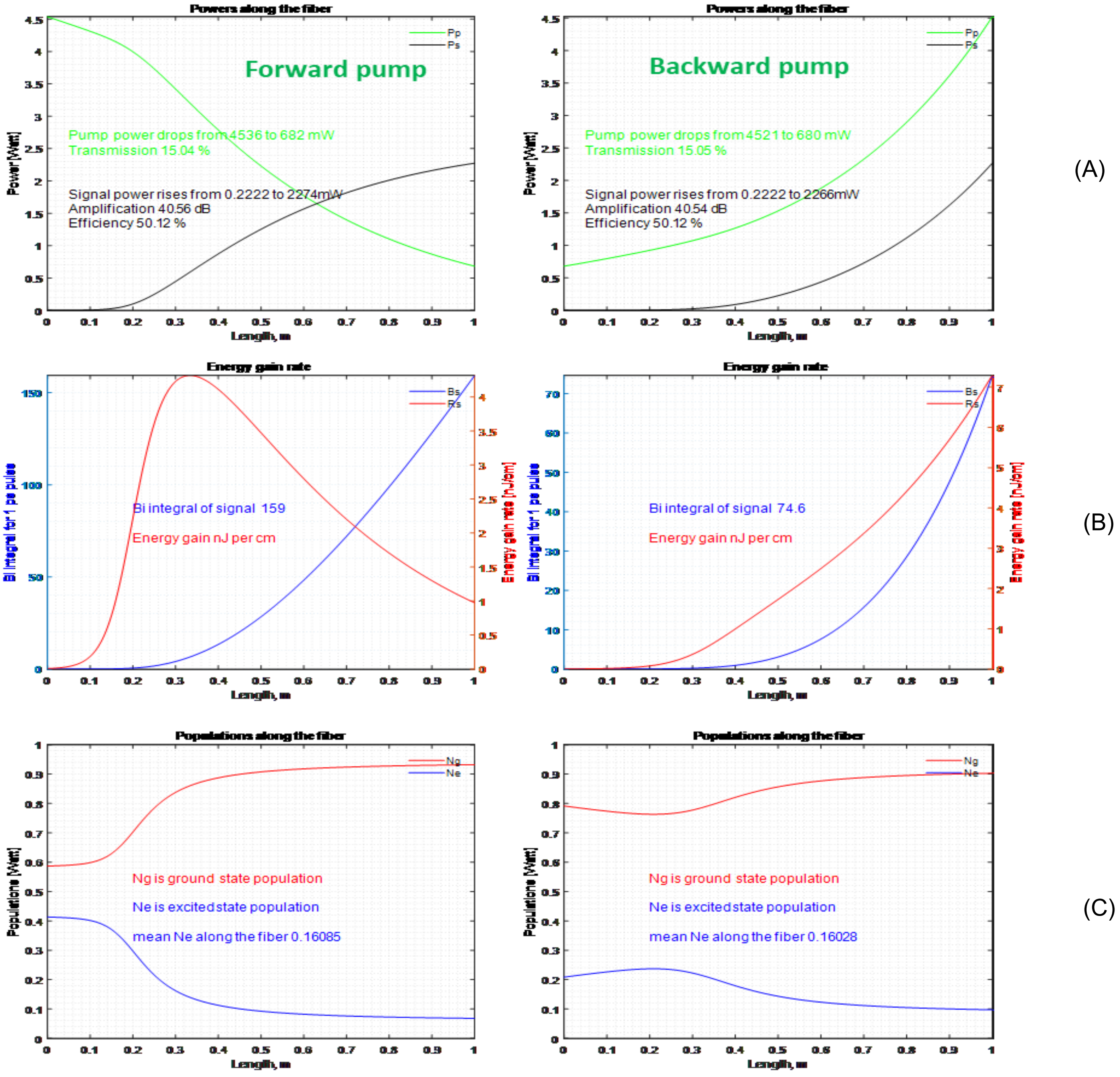

Figure 1-14 Calculations Left and Right, Forward and backward pumping respectively, Bi-integrals were calculated for input pulse parameters are presenting in the laser under research.

1.9 Interference optical thin-film bandpass filters

Interference optical bandpass filters are one of the key components used in the X-filters laser configuration, to be described later.

Interference spectral filters are, in fact, Fabry - Perrot interferometers with a very small gap between parallel mirrors.

A schematic representation of the design of the interference filter is shown in Fig.1.15

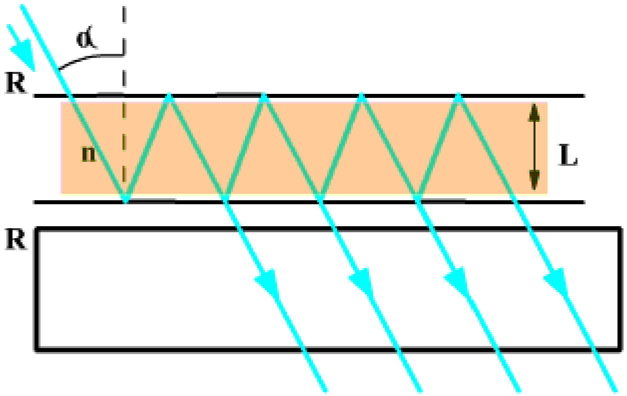

Figure 1-15 One layer of thin-film interferometric filter.

On a glass substrate are deposited sequentially (usually by vacuum sputtering): a mirror R with a high reflectance; a dielectric layer with a refractive index n of small thickness L (one - several radiation wavelengths for which this filter is designed), - and another mirror R, similar to the first. The result is a Fabry - Perrot etalon with a very small dielectric gap thickness. The combination of multiple such interferometers can produce almost any desirable transmission spectrum [Mar96]. We are using thin-film filters with about 300 layers which give us very narrow optical pass band with high suppression beyond the band and, at the same time, very low optical losses within the band.

In spite of the very small thickness (less than 1 mm) due to multiple layers interference the filter can produce a phase shift on our signal that can destroy the pulse quality (coherence). Fig.1.16

As a part of the development program, we measured the real phase shift induced by the applied filters.

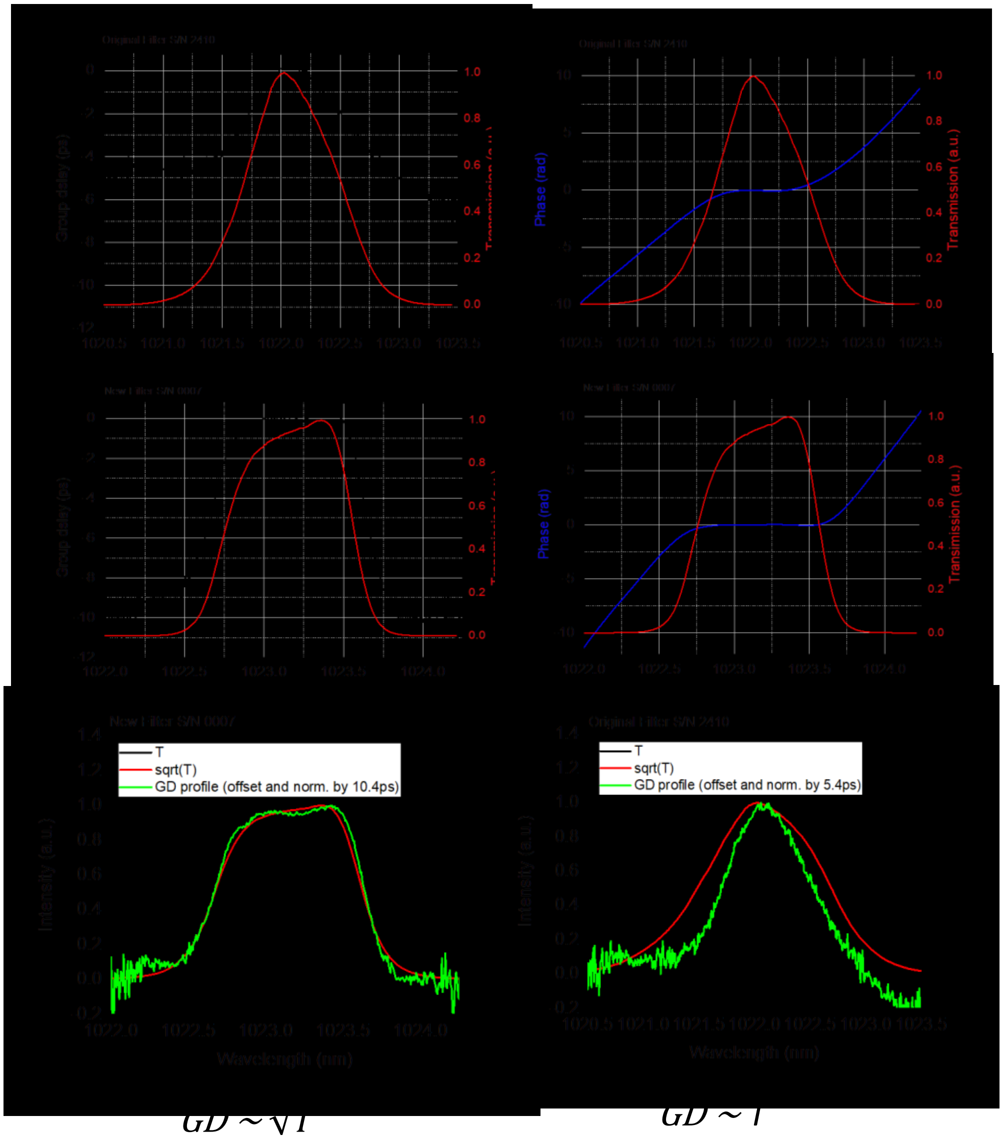

Figure 1-16 Transmission, group delay and phase shift for two types of filters used in our system.

As can be seen within the transmission band, the phase shift for the second filter (that is used now in the laser) is much more flat than for the previous one. But in the computer model we still using actual data, even if the effect is small enough, for better compliance.

1.10 Ultrafast pulse measurements

In the 1960s, laser pulse durations broke the nanosecond barrier and became shorter than even the fastest electronics could measure - hence the field of ultrashort laser pulse measurement was born, as new techniques were required in order to overcome the limits of electronics.

In this work, we deal with laser pulses with durations from 10-15 psec to 40 fsec.

Various types of autocorrelation are used to measure the duration of such pulses. [Tre02]

1.10.1 Autocorrelations

The simplest way to measure a short pulse is by field autocorrelation at the photodetector. See Fig.1.17 Technically, the system is a two-arms Michelson interferometer in which the initial pulse is split into two beams that interfere with each other at the input of the photodetector. By continuously varying the length of one arm, you can extract the autocorrelation function of the pulse and so determine the pulse duration.

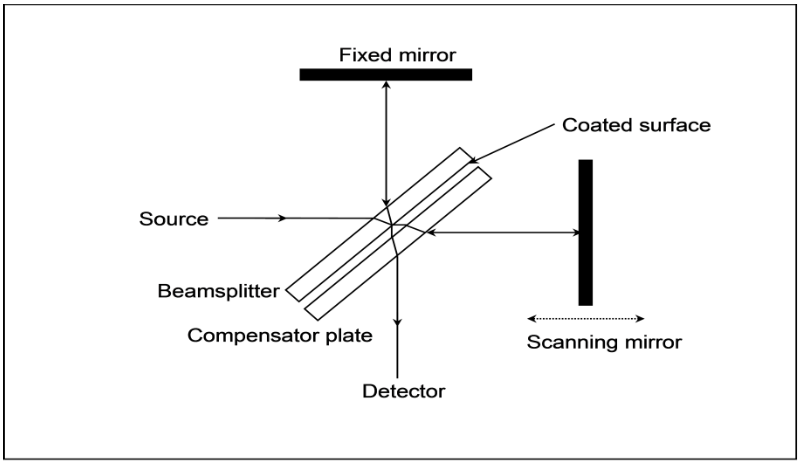

Figure 1-17 Simple configuration of field autocorrelator.

1.10.2 Autocorrelation function of field

The real electric field is practically impossible to measure, because of the fast oscillations ($\sim 10^{-15} s$)

$$\mathcal{E}(t) \propto E(t) + \overline{E(t)} \tag{1}$$

where $E(t)$ is the complex electric field, a mathematical construction, which is not physical and impossible to measure and $\overline{E(t)}$ is complex conjugate to $E(t)$.

The Fourier transform of electric field is a complex function

$$E(v) \propto \int_{-\infty}^{+\infty} E(t) e^{-i2\pi v t} dt \tag{2}$$

The power spectrum of the field,

$$S(v) \propto |E(v)|^2 \tag{3}$$

where v is defined for positive value, it is possible to measure.

The intensity of light of two delayed replicas of pulses

$$I(t,\tau) \propto |E(t) + E(t-\tau)|^2 = |E(t)|^2 + |E(t-\tau)|^2 + 2Re\left[E(t)\overline{E(t-\tau)}\right] \tag{4}$$

Here an autocorrelation function of the field is not a constant part of integrated intensities, it is a function of delay time.

$$A(\tau) \propto \int_{-\infty}^{+\infty} E(t)\overline{E(t-\tau)} dt \tag{5}$$

The spectrum of the signal is the Fourier transform of an autocorrelation function (Weiner-Khinchin theorem) and autocorrelation function is the Fourier transform of the Spectrum

$$\begin{gathered} S(v) \propto \int_{-\infty}^{+\infty} A(\tau) e^{-i2\pi v \tau} d\tau \\ A(\tau) \propto \int_{-\infty}^{+\infty} S(v) e^{i2\pi v \tau} dv \end{gathered} \tag{6}$$

The Interferogram is a fully measured signal including a constant part and the autocorrelation function normalized on full intensity:

$$INT(\tau) \propto 1 + Re\left\{\int_{-\infty}^{+\infty} E(t)\overline{E(t-\tau)} dt\right\}/I \;= 1 + Re\{A(\tau)/A(0)\} \tag{7}$$

Unfortunately, the direct autocorrelation field function adequately reflects the pulse width only for the case of a transform limited pulse. In real devices and experiments, a laser pulse propagates in a medium with nonzero chromatic dispersion, which leads to a significant broadening of the pulse with a constant spectrum. The autocorrelation of the field does not feel the influence of the phase incursion from the frequency and gives deliberately distorted values for the pulse duration and shape.

1.10.3 Autocorrelation function of intensity

In an intensity autocorrelator as shown in Figure 1.18, a beam splitter splits the incoming pulse into two pulses, which are focused and sent to a nonlinear crystal with χ (2) nonlinearity. Relative timing of the pulses, can be mechanically adjusted by means of a variable delay line (different types of delay lines are used, for example, rotating glass blocks or mirrors mounted on vibrating speakers).

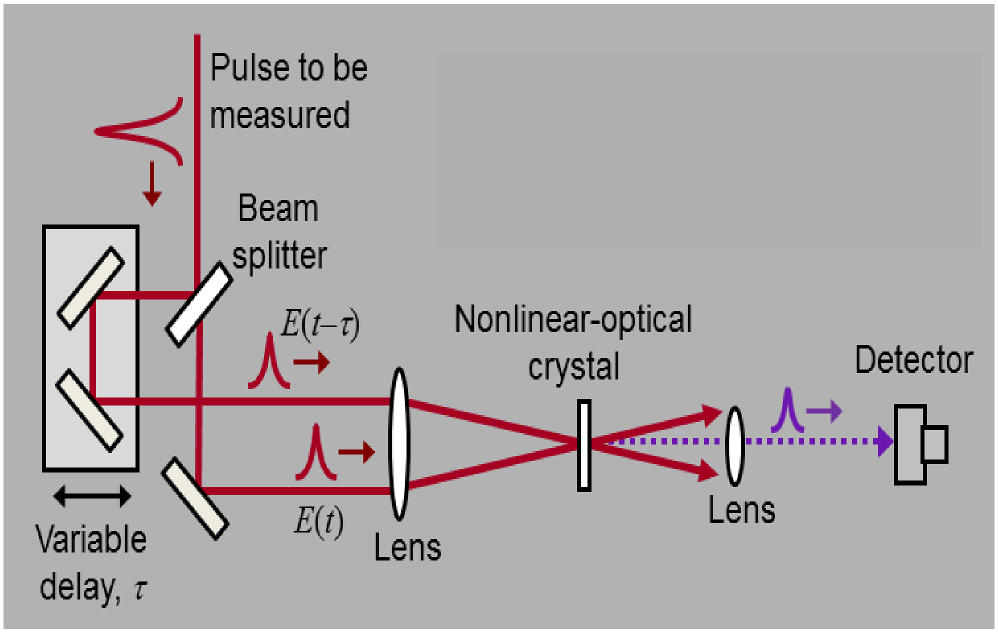

Figure 1-18 Typical intensity autocorrelation configuration.

If the arm lengths match, such that the pulses arrive simultaneously at the nonlinear crystal, the second harmonic is generated, which can be detected at the output of the device. If the relative delay is increased and the overlap of two pulses in the crystal decreases, the intensity of the second harmonic generation is weaker.

The intensity of second harmonic generation of the two delayed fields is given by

$$E_{SHG}(t,\tau) \propto [E_1(t) + E_2(t-\tau)]^2 \qquad (8)$$

$$I_{SHG}(t,\tau) \propto |[E_1(t) + E_2(t-\tau)]^2|^2 = |E_1(t)^2 + 2E_1(t)E_2(t-\tau) + E_2(t-\tau)^2|^2 \qquad (9)$$

$$\begin{aligned} I_{SHG}(t,\tau) \propto {} & E_1(t)^2\overline{E_1(t)^2} + 2E_1(t)^2\overline{E_1(t)E_2(t-\tau)} + E_1(t)^2\overline{E_1(t-\tau)^2} + \\ & 2E_1(t)E_2(t-\tau)\overline{E_1(t)^2} + \underline{2E_1(t)E_2(t-\tau)\overline{E_1(t)E_2(t-\tau)}} + 2E_1(t)E_2(t-\tau)\overline{E_2(t-\tau)^2} \\ & E_2(t-\tau)^2\overline{E_1(t)^2} + 2E_2(t-\tau)^2\overline{E_1(t)E_2(t-\tau)} + E_2(t-\tau)^2\overline{E_1(t-\tau)^2} \end{aligned} \qquad (10)$$

There are 9 terms here, but not all of these terms are giving a contribution to the signal because SHG can be achieved only according to some specific selection rules depending on the direction of propagation of the fields, the type of SHG and the indexes of refraction for fundamental and second harmonic. Analysis of the selections rules can be found in textbooks [Agr08, Ahm88]. According to these rules, in some cases (non-collinear propagation SHG of type II crystal cut) the measured SHG intensity will be equal to the barred term of the Eq.10.

$$I_{SHG}(t,\tau) \propto 2E_1(t)E_2(t-\tau)\overline{E_1(t)E_2(t-\tau)} \propto I_1(t)I_2(t-\tau) \qquad (11)$$

If we measure the integrated intensity of SHG generation as a function of delay time we will get an autocorrelation function of the intensity, similar but different to the interferogram of Eq.7

$$\boldsymbol{ACF(\tau)} \propto \int_{-\infty}^{+\infty} \boldsymbol{I(t)I(t-\tau)dt} \quad \mathbf{(12)}$$

Because the intensity in the time domain depends not only on the spectrum of the pulse but also on the so called spectral phase, then this function is not equal to the Fourier transform of the spectrum as for the autocorrelation function in Eq.6

1.10.4 Comparison of autocorrelation function of field and intensity for Transform Limited (TL) and linear chirped pulses

Fig. 1.19 compares the results of modeling the measurement of pulses with the same spectra but different durations or shape in the time domain using field or intensity autocorrelations. In Fig.1.19 (left and right) the spectrum is the same but pulse on the right has a chirp (different frequencies have different speed of propagation as in normal media). We can see that the interferogram (or autocorrelation of field) cannot detect this distortion and in both cases are the same, but the autocorrelation of intensity is wider and the pulse duration can be calculated using this measurement, if and only if we know that pulse has a known phase distortion, in other words we can recalculate the value of a known phase distortion.

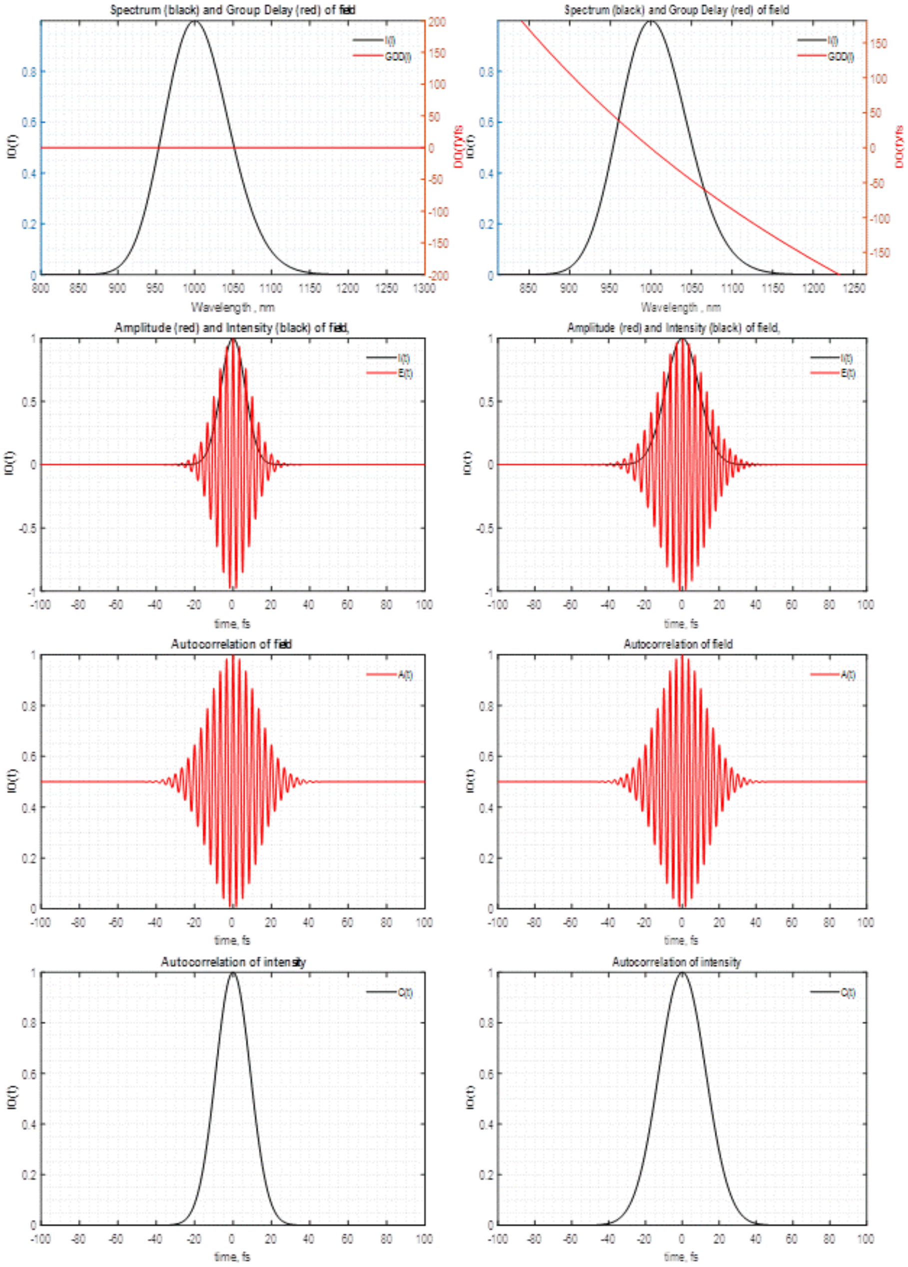

Figure 1-19 Gaussian pulse I(t)=exp(-t^2/τ^2) with Full Width Half Maximum 15 fs in the time domain (τ=9fs). Left column is for a transform limited (TL) pulse (no phase distortion), right is for a pulse chirped with a linear phase distortion $\phi(\omega)=(\tau\omega)^2$ in the frequency domain. First row shows the spectra (black) and Group Delay Dispersion $d\phi(\omega)/d\omega=2\tau\omega$ for a chirped pulse. The second row is the intensity and the electric field strength (normalized on max). The third row is the interferograms (see formula 7). The fourth row is the SHG non-collinear autocorrelation (see formula 12).

1.10.5 Comparison of autocorrelation function of field and intensity for spectrally and phase asymmetrical pulses

In Fig.1.20 (left and right) the spectrum of the pulse is the same but the pulse on the right has a more complicated phase distortion. Here we can see that even the autocorrelation of intensity cannot determined even the sign of the time delay (it is symmetrical around zero delay time). Both methods cannot measure time profiles of intensity in the time domain for even slightly complicated spectra and phase distortions.

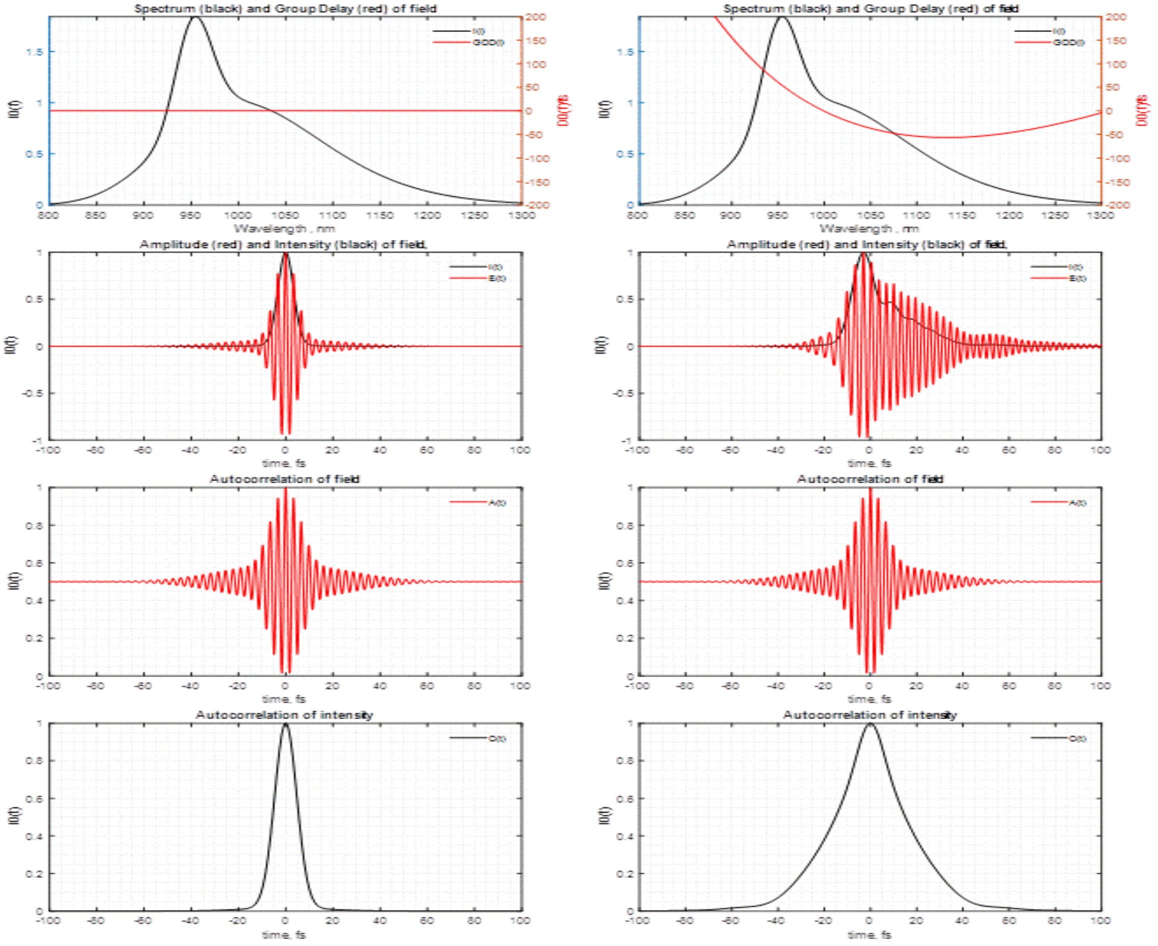

Figure 1-20 Left column is a TL pulse (no phase distortion), right is for a pulse with cubic chirp. The first row is the spectra (black) and the Group Delay Dispersion (dϕ(ω)/dω) (red). The second row is the intensity and the electric field strength (normalized on max). The third row is the interferograms (see formula 7). The forth row is the SHG non-collinear autocorrelation (see formula 12).

1.10.6 Examples of strongly distorted pulses

In Fig. 1.21 we demonstrate pulses generated from the model of our laser (which will be described later in the text) in the spectral and time domains and their associated autocorrelation. In the first row we see the pulse generated by the laser. It is about 50 nm wide and heavily chirped, up to 5 ps pulse duration, with the autocorrelation only reflecting that the pulse is long, but have no information about the real shape of it in time domain. On the second row is the result of calculations in the case of a TL (no phase distortion) pulse with the same spectrum. We can see that the pulse is very short in time domain and exhibits pre and sub pulses. It is practically impossible to remove all phase distortion. In the best case we can remove the smoothest region and end up with the pulse presented on third row. Here the pulse has a very sharp front edge and a long tail, but the simple autocorrelation function cannot distinguish between the nose and the tail. In this particular case, the compression is very good. The intensity of the main fs portion of pulse is more than 1000 times intense and the autocorrelation looks as a scanning delta function across the long tail. If we can define a sign of the time delay we can use it for pulse characterization.

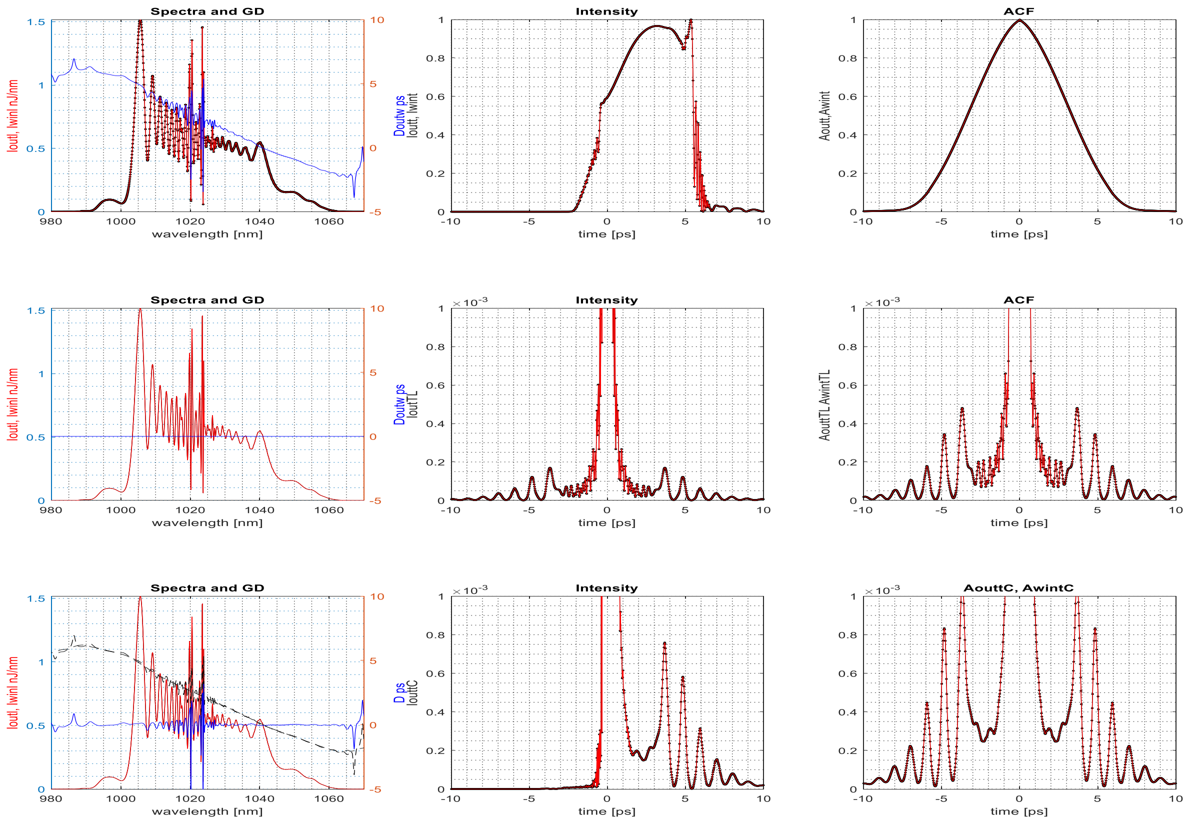

Figure 1-21 The pulse generated by our laser (model). The top row is the uncompensated pulse and its ACF, middle row the theoretical fully phase compensated pulse, bottom row pulse with compensation of smoothed phase distortion. Note: Uncompensated pulse picosecond pulse duration with linear rising and sharp end and some tail. Compensated pulse has long tail.

As we have seen in the previous examples, neither the autocorrelation of field nor intensity can measure the temporal profile of a light pulse in the case of an asymmetrical spectral shape and/or nonlinear phase distortion. To measure the time profile of a nontrivial light pulses different methods have necessarily been developed including:

SPIDER (Spectral Phase Interferometry for Direct Electric-field Reconstruction)

FROG (Frequency-Resolved Optical Gating)

MIIPS (Multiphoton Intrapulse Interference Phase Scan)

1.10.7 SPIDER

SPIDER is an interferometric pulse measurement technique in the frequency domain based on spectral shearing interferometry in the frequency domain. The spectral shear is generated by sum-frequency mixing the test pulse (TP) with two different quasi-monochromatic frequencies derived by chirping a copy of the pulse (CP). See Fig. 1.22 [Wal98]

The intensity of the interference pattern from two time-delayed spectrally sheared pulses can be written as

$$S(\omega) = \left|E(\omega) + E(\omega-\Omega)e^{i\omega\tau}\right|^2 = I(\omega) + I(\omega-\Omega) + 2\sqrt{I(\omega)I(\omega-\Omega)}cos[\phi(\omega) - \phi(\omega-\Omega) - \omega\tau] \tag{13}$$

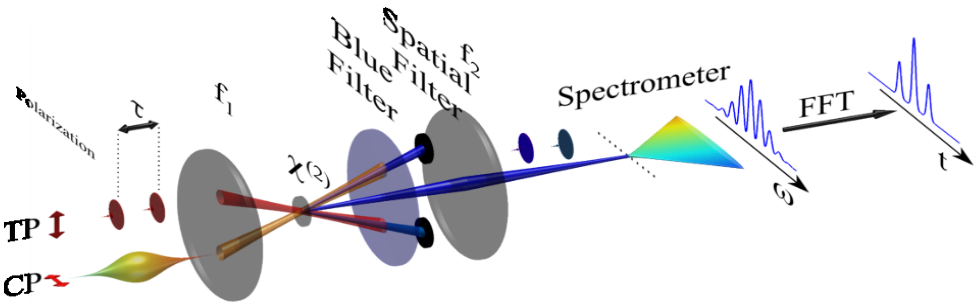

Figure 1-22 Typical SPIDER configuration.

Analyzing the phase of the oscillating *cos* function it is possible to extract the unknown spectral phase $\phi(\omega)$. But, this method requires extreme spectrometers with very high spectral resolution, very high energy of the pulse to be analyzed and overall is a very expensive and complex method, which can be afforded only by a handful of university laboratories.

1.10.8 FROG and MIIPS

The FROG spectrogram is a graph of the intensity as a function of frequency ω and delay τ between two replicas of the pulse. See Fig.1.23 [Tre97]

The measured signal can be generated using different nonlinear optical methods, and in the case of using non-collinear sum harmonic generation in type II SHG media can be written as

$$FROG(\omega,\tau) = \left|\int E(t)E(t-\tau)e^{i\omega t}d\omega\right|^2 \tag{14}$$

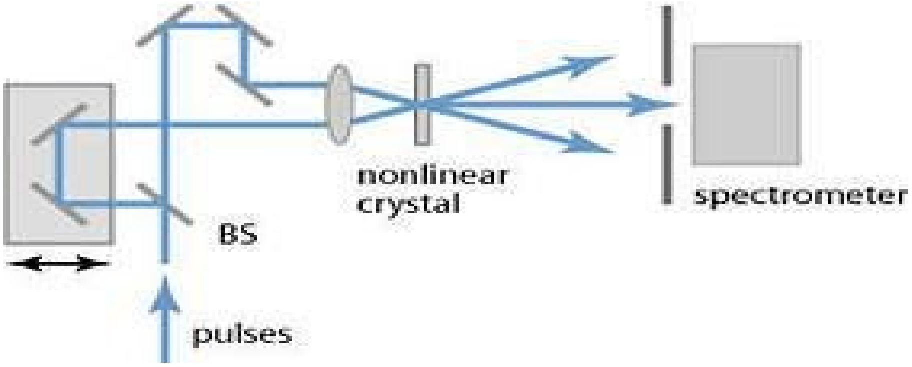

Figure 1-23 Typical FROG configuration.

The MIIPS is a method that simultaneously measures (phase characterization), and compensates (phase correction) femtosecond laser pulses using an adaptive pulse shaper. See Fig.1.24 [Dan03]

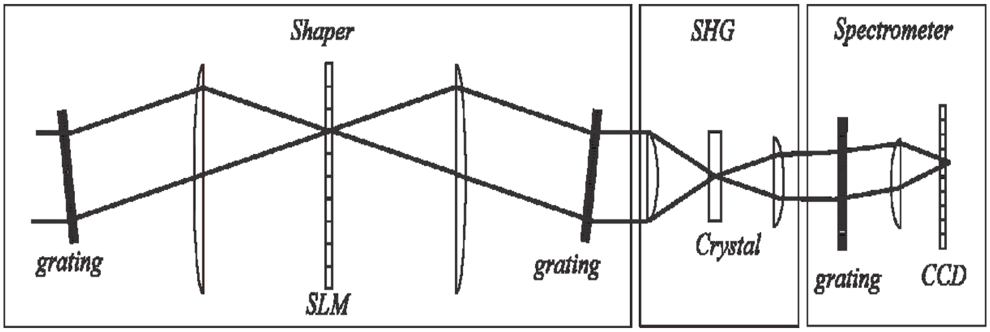

Figure 1-24 Typical MIIPS configuration.

The MIIPS trace is dependent on the SHG intensity as a function of frequency ω and applied calibrated phase distortions, in the simplest case an additional constant chirp $c(\omega) = d^2\phi(\omega)/d\omega^2$

$$MIIPS(\omega, c) = \left|\int E'^2(t)e^{i\omega t}d\omega\right|^2, \tag{15}$$

where $E'(t) = \int E(\omega)e^{-ic(\omega-\omega_0)^2/2}e^{-i\omega t}d\omega$ (16)

Both the above methods are based on measuring sum frequency generation, but show very different methods of extraction/measuring the phase distortions. In the case of FROG, one must use a very complex and sophisticated mathematical algorithm, but in essence is a guess and probe of the spectra to reproduce the measured 3D surface of FROG, which is very sensitive to systematic and random noise of measurements and unreliable in the case complex spectra and/or phase distortions. In the case of MIIPS to extract phase one does not need any mathematical manipulation, it is a simple measurement line through the maximum of the 3D surface as a function of frequency. In rare cases when the extracted second derivative is too big and/or too complicated then using the same shaper which applied roughly compensates the pulse chirp and then the procedure is repeated. Usually in second or third iteration phase $c(\omega) = d^2\phi(\omega)/d\omega^2$ the distortion is measured from which phase is just calculated by numerical integration $\phi(\omega) = \iint c(\omega)d\omega d\omega$.

In the following figures a comparison of the FROG with MIIPS methods are presented for pulses with complicated phase and nonlinear phase distortions. One can easily see that MIIPS traces are very easy to analyze and see phase distortion, as opposed to the FROG trace where it is impossible to see what has occurred without use of unreliable fitting procedures. For example, in Fig.1.25 the presence of just a simple linear chirp generates a very complicated FROG trace, but in the case of MIIPS the chirp scan is very easy to detect and measure on the basis of the visual picture shape. In the case of more complicated phase distortion (positive or negative cubic chirps on Fig. 1.26) the FROG traces are a complete mess and practically impossible to analyze, but with MIIPS a simple pattern is displayed and through determination of the maximums of 3D surface the second derivative of the phase in the frequency domain may be measured and phase calculated by a simple integration.

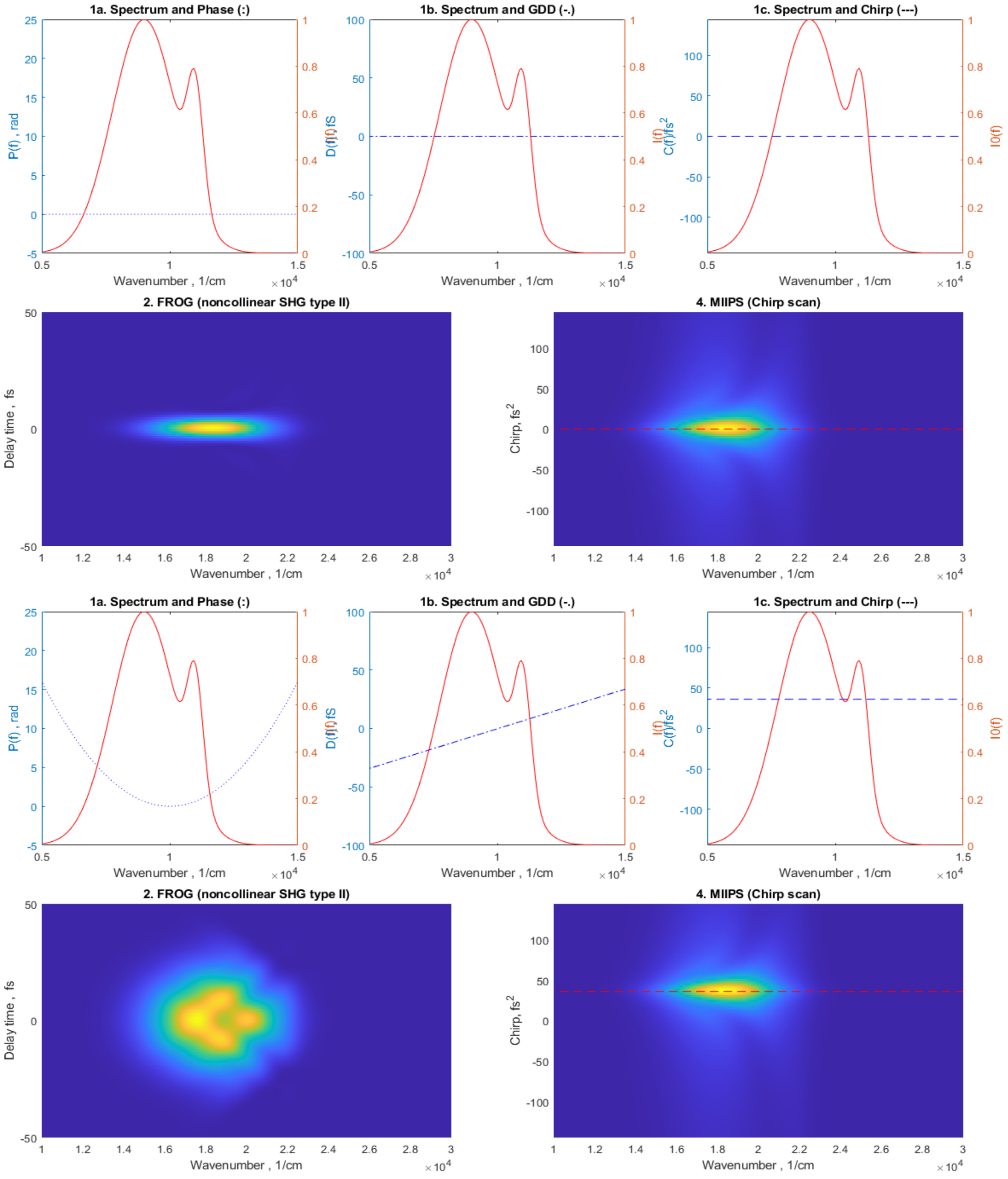

1a. Spectrum and Phase (:)

1b. Spectrum and GDD (-.)

1c. Spectrum and Chirp (---)

2. FROG (noncollinear SHG type II)

4. MIIPS (Chirp scan)

1a. Spectrum and Phase (:)

1b. Spectrum and GDD (-.)

1c. Spectrum and Chirp (---)

2. FROG (noncollinear SHG type II)

4. MIIPS (Chirp scan)

Figure 1-25 Left columns are FROG, and right are MIIPS traces. The first row is the analysis of the pulse with a complex spectrum and no phase distortion (TL pulse). The second row is a pulse with linear chirp. 1. Spectrum and a) phase $\phi(\omega)$ b) GDD= $d\phi(\omega)/d\omega$ c) local chirp $=d^2\phi(\omega)/d\omega^2$. 2 FROG trace, 4. MIIPS trace and line corresponding to local chirp

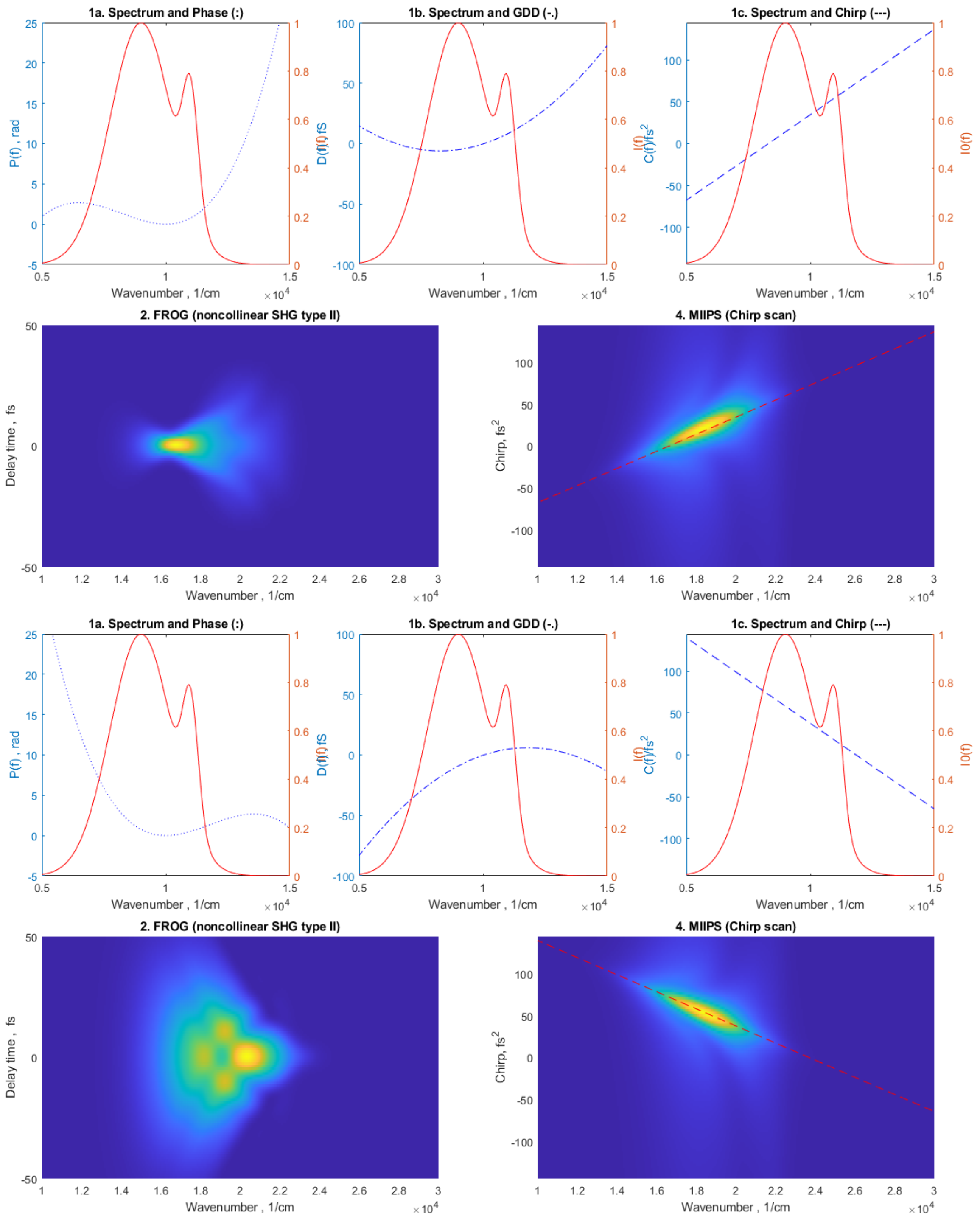

Figure 1-26 Left columns are FROG, and right are MIIPS traces. The first row is the analysis of a pulse with a complex spectrum and positive (left) and a negative (right) cubic phase distortion ($d^3\phi(\omega)/d\omega^3$). 1. Spectrum and a) phase $\phi(\omega)$ b) GDD= $d\phi(\omega)/d\omega$ c) local chirp =$d^2\phi(\omega)/d\omega^2$. 2 FROG trace, 4. MIIPS trace and line corresponding to local chirp

1.10.9 Fidelity

Here we discuss measuring a pulse which cannot be fully characterized because it has some unknown values, such as some spectral and phase distortions, or a sequence of pulses with slightly different spectra and phases. Three examples of such uncertainties are discussed here including:-

Homogeneous distortion (all pulses are identical but there is distortion of the spectrum or spectral phase).

Inhomogeneous pulse sequence (all pulses have different spectra and spectral phases).

Distorted spectrum and phase (in this case we do not know the exact spectrum or there is some systematic phase compensation).

New metrics for femtosecond lasers have been introduced called “fidelity” [Dan13] to characterize pulse-to-pulse stability and intrinsic pulse quality. The method is based on using an additional strong chirp to stretch the pulse and compare the intensity of SHG (Second Harmonic Generation) of that pulse with the SHG intensity generated by pulses with the same spectrum but no amplitude or phase distortions. Because the distorted pulse is usually longer than the corresponding TL pulse then it will generate less second harmonic signal and this attenuation will give a metric to characterize generation. The MIIPS trace is the dependence of the SHG intensity as a function of the frequency ω and applied calibrated phase distortions, which in the simplest case is an additional constant chirp $c(\omega)=d^2\phi(\omega)/d\omega^2$. MIIPS is a function of frequency and chirp and the integral of the MIIPS 2D trace over all frequencies will the give total intensity of SHG generational at some chirp SHG(c)

$$MIIPS(\omega,c) = \left|\int E'^2(t)e^{i\omega t}d\omega\right|^2, \qquad (17)$$

where $E'(t) = \int E(\omega)e^{-ic(\omega-\omega_0)^2/2}e^{-i\omega t}d\omega$ (18)

$$SHG(c) = \int MIIPS(\omega, c) d\omega \tag{19}$$

Simple spectral measurements of the pulse do not produce phase information, but we can calculate how the SHG will be generated by a TL pulse with measured spectrum $SHG_{TL}(c)$. Because (usually) we do not know efficiency of SHG we can use relative values to characterize the efficiency of SHG

$$S(c) = \frac{SHG(c)}{SHG(0)} \tag{20}$$

For large chirps the value 1/S(c) is proportional to c because of the linearly stretched pulse in the time domain. The shorter pulse initially the bigger the stretching by chirping. The ratio of the efficiency of stretching in comparison to a TL pulse we call the “Fidelity function” of the pulse

$$F(c) = \frac{S_{TL}(c)}{S(c)}. \tag{21}$$

For large chirps this value converges to some constant called just simple “Fidelity”. The closer the fidelity to 1 the “better” the quality of the pulse.

Pulse distortions may be different in nature. If all pulses are identical, but the amplitude or phase have the same non coherent distortions of each pulse, then we call this case homogeneous distortions (analogous to optical spectroscopy). If the pulses have different distortions of any kinds, then it the case of inhomogeneous distortions we only characterize the whole ensemble of pulses by comparing the fidelity measured using the average spectrum of the ensemble, using $E_{TL}(\omega) \propto \sqrt{I(\omega)}$ with the measured $I(\omega)$ to calculate the efficiency of SHG

In the following figures the results of simulation of the calculation of fidelity for different cases are presented. In each figure on panel 1 are the spectra and phase of the average pulse (dash line) and measured pulses. On panel 2 is the corresponding intensity in time in dB ($10\log_{10}(I(t)/I(0))$) for the TL pulse calculated using the average spectrum. On panel 3 is MIIPS (chirp scan of measured pulse). On panel 4 are intensities of SHG of measured and TL pulses (blue) and their inverse functions (red). On panel 5 the Fidelity function which converges to the fidelity value at large chirps is presented. In Fig. 1.27 it is shown how the presence of amplitude or phase modulation of measured pulse decreases the value of the Fidelity (which is value of fidelity function for large chirps).

Fig. 1.28 shows the results of modeling a sequence of pulses with different amplitude or phase distortions, when we do not measure the individual pulses but take an overall average result, when the pulses with distortions have smaller than 1 Fidelity.

Shown in Fig.1.29 are the results of modeling the measurement of a pulse with an unknown hole in the spectrum or unknown (uncompensated) phase distortion. Again the asymptotic fidelity is less than 1. The main question is what fidelity is acceptable for a particular application of a particular laser and this is a practical problem. Usually we assess lasers with fidelity 0.99 as perfect, 0.9 as good, 0.8 as acceptable and 0.7 as bad.

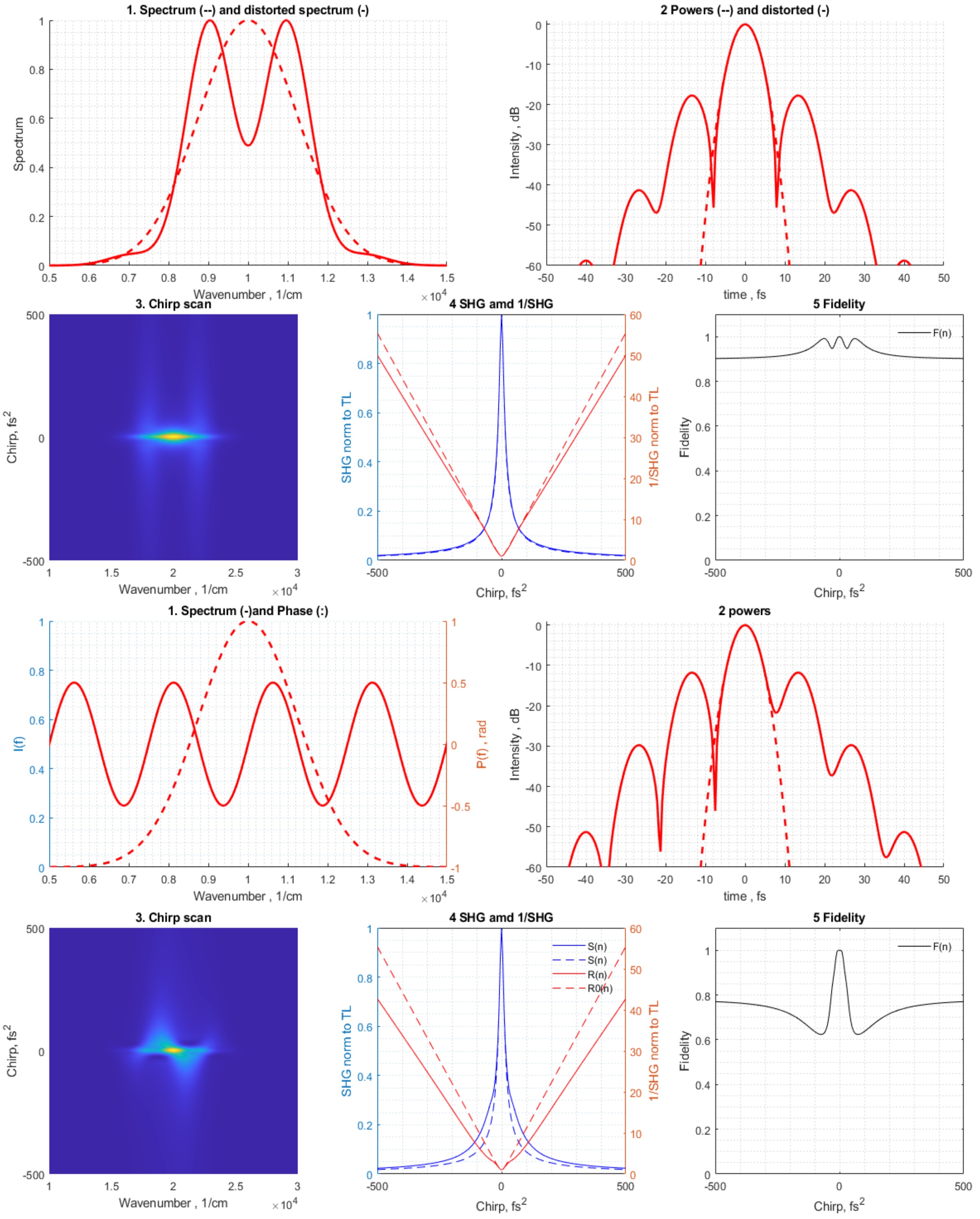

Figure 1-27 Homogeneous fidelity, when all pulses in measuring the SHG as a function of the chirp are identical. First row is the case of periodical spectral distortion, second row is the case of periodical phase distortion.

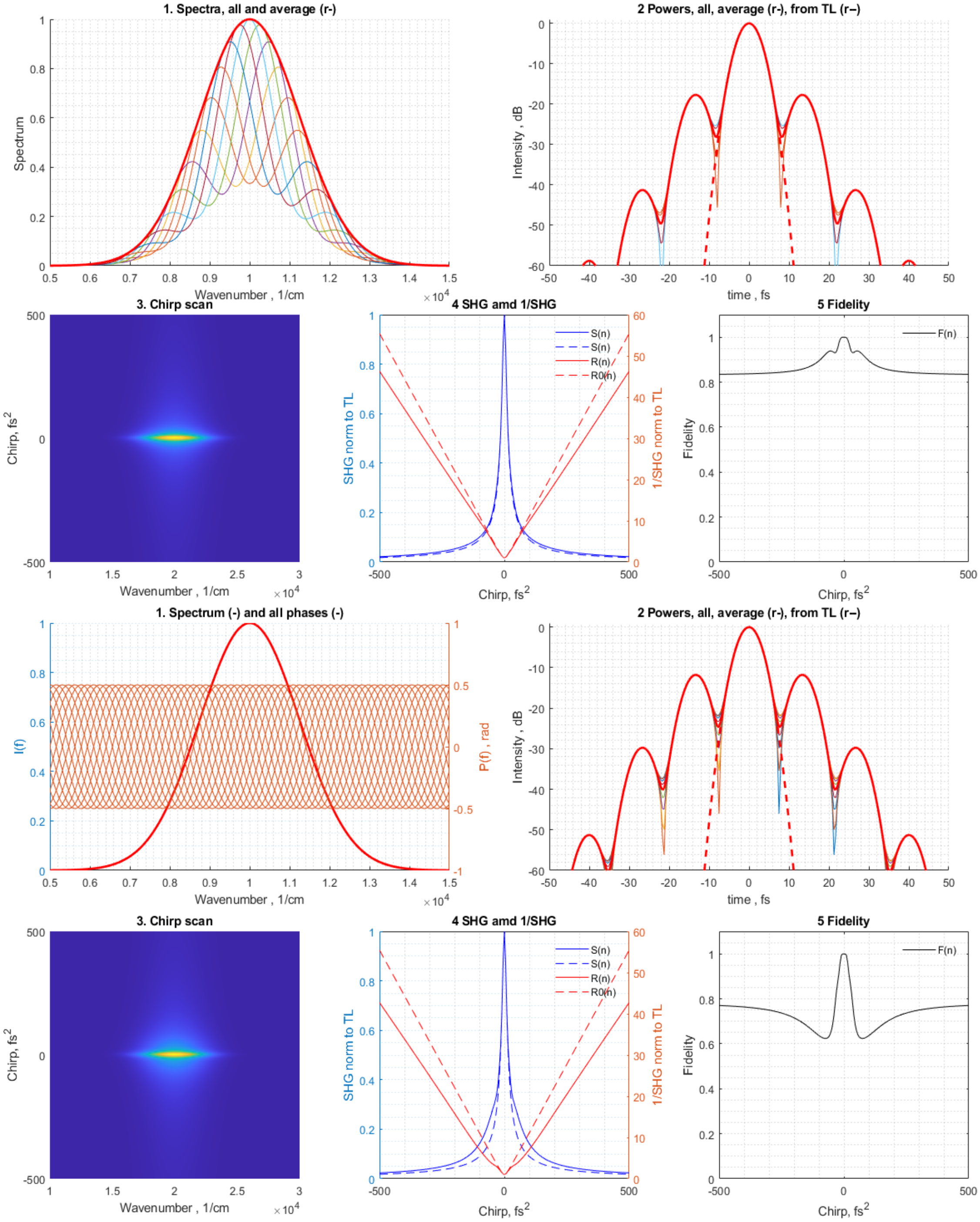

Figure 1-28 Inhomogeneous fidelity, when all the pulses used to measure the SHG as a function of chirp are different. First set is the case of periodical spectral distortion with different phases, second set is the case of periodical phase distortion with different

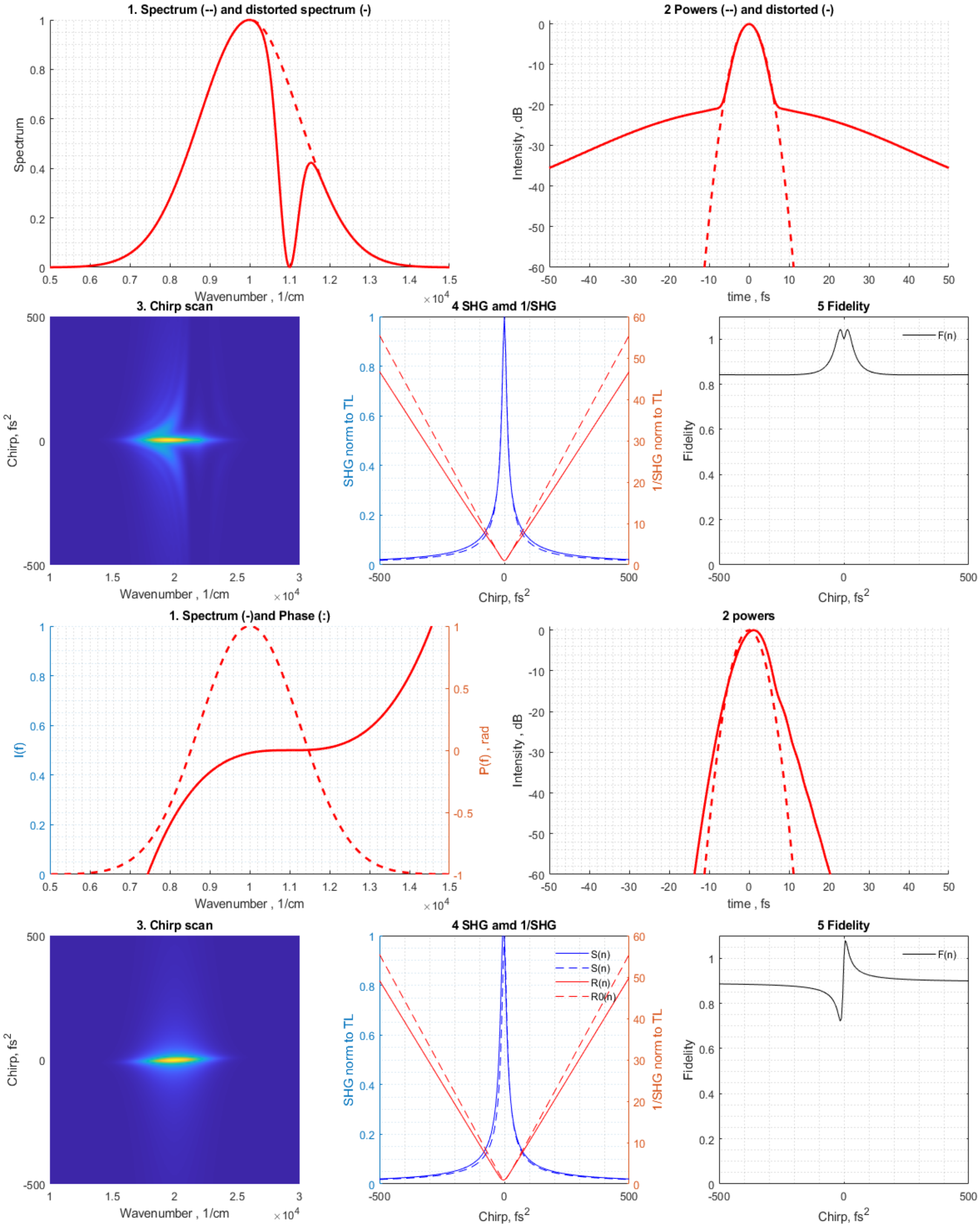

Figure 1-29 Fidelity, when calculation were carried out using distorted spectrum (first set) or additional uncompensated cubic distortion (second set)

2 Technological Landscape

Here we consider the main advantages of picosecond and femtosecond lasers over traditional nanosecond and microsecond lasers.

Picosecond lasers allow the processing of any kind of solid-state materials, regardless of the linear absorption coefficient of the material at the incident laser radiation wavelength. This is due to the very high peak power of picosecond pulses, which on focusing allows operation far into the nonlinear absorption zone of any material. Thus, for example, using a 1 micron laser, it is possible to effectively cut materials like sapphire or diamond which are transparent in this spectral range.

Picosecond lasers allow one to process materials in a pure ablation mode, that is, bypassing the stage of melting of the treated material and immediately converting the materials into a vapor. This is due to the fact that the pulse energy absorbed by the electrons of the medium does not have sufficient time to transfer to the kinetic energy of the atoms of the material during the duration of the pulse, while the amount of energy pumped into the small volume at the focal spot typically significantly exceeds the melting and evaporation heating energy combined. Thus, the material goes into a plasma state with a temperature of 3000C and above instantly flying away from the surface being processed. This allows for precision cutting and micro-processing without changing the structure of the treated material and without the occurrence of thermal stresses.

Femtosecond lasers are even more flexible in their impact on these materials. While maintaining the high peak power necessary for nonlinear absorption, the pulse energy can be small enough such as not to evaporate the material but only to melt it at any specified point (for example, in welding transparent materials at the point of internal contact when the laser radiation passes through the material and is focused at a contact point between the two plates).

For femtosecond lasers with extremely short pulse durations (<100 fs), nonlinear absorption occurs without substantial heating of the material itself, which is a critical requirement for numerous applications in medicine and biochemistry.

Here we briefly consider the design of the more common commercially available ultrafast laser systems.

A pulsed laser system is most frequently configured as an oscillator with a fixed cavity length. The frequencies circulating in the cavity and having more gain than the combined losses are called the longitudinal modes and can be considered as an assembly of independent oscillators. While circulating in the cavity, the longitudinal modes are separated by $\Delta F = v/L$, for a fiber laser configured with a ring cavity which is of particular interest here, where L is the cavity length and v is the speed of light in the cavity. When these modes oscillate independently of each other, the laser emits continuously. However, when a fixed phase shift exists between the various modes, the laser becomes mode locked and the cavity emits a pulses train.

Several methods for generating ultrashort pulses are well established. One of these methods – passive mode locking – is part of the subject matter under research and reported here. The process of passive mode locking of lasers was introduced by Mocker and Collins through the introduction of a liquid saturable absorber cell in a pulsed ruby laser [MOC65]. The key to the passive modelocking is the presence in the cavity of at least one component which exhibits a nonlinear response to increasing peak intensity. Several architectures are known to carry out the passive mode locking mechanism.

One of these architectures is nonlinear polarization rotation (NLPR) [STO82] [NEL97][KOB10] which can be better understood using the ring cavity shown in the Fig.2.1. The polarizing isolator placed between two polarization controllers acts as the mode-locking element. It plays the double role of an isolator and a polarizer, such that light leaving the isolator is linearly polarized. The polarization controller placed after the isolator changes the polarization state to elliptical. The polarization state evolves nonlinearly during propagation of the pulse because of self-phase and cross-phase modulation induced phase shifts imposed on the orthogonally polarized components. The state of polarization is non-uniform across the pulse because of the intensity dependence of the nonlinear phase shift. The second polarization controller (placed before the isolator) is adjusted such that it forces the polarization to be linear in the central part of the pulse. The polarizing isolator lets the central intense part of the pulse pass but blocks (absorbs) the low-intensity pulse wings. The net result is that the pulse is shortened after one round trip inside the ring cavity. Thus the polarization-dependent isolator, working together with the birefringence fiber, can generate an intensity-dependent loss.

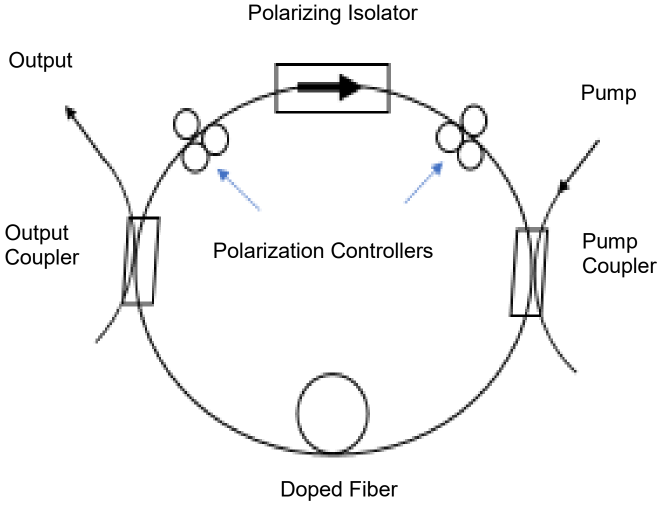

Figure 2-1 Configuration of a fiber laser mode locked using nonlinear polarization rotation

A variety of ultra-high-energy pulses can be successfully generated by using the NLPR architecture including solitons, gain-guided solitons usually with cavity dispersion purely normal, and similaritons. However, the polarizing controllers require complicated feedback with a fine control system to establish and maintain the mode locking process. The NLPR process is also sensitive to environmental changes and packaging conditions. As a consequence, it is difficult to satisfy periodicity conditions, i.e., reproducibility of pulse characteristics at a consistent location after each round trip of the laser cavity.

The interferometric fiber architecture has two general types: the nonlinear optical loop mirror (NOLM) [DOR88] shown in Fig. 2.2A and the nonlinear amplification loop mirror (NALM) [FER90] seen in Fig. 2.2B. The latest developments in pulse generation using these devices can be seen in [NIC07] [AGU10] [AGU12]. Both configurations are working in accordance with “Sagnac” interferometer operation. The latter is constructed from a fused fiber coupler whose output ports are spliced together to form a loop and the counter-propagating intensities Ic (clockwise) and Icc (counterclockwise) are made unequal either by the coupler splitting not equal 50% (NOLM) or by the inclusion of an in-line fiber amplifier closer to one of the ports of the coupler (NALM).

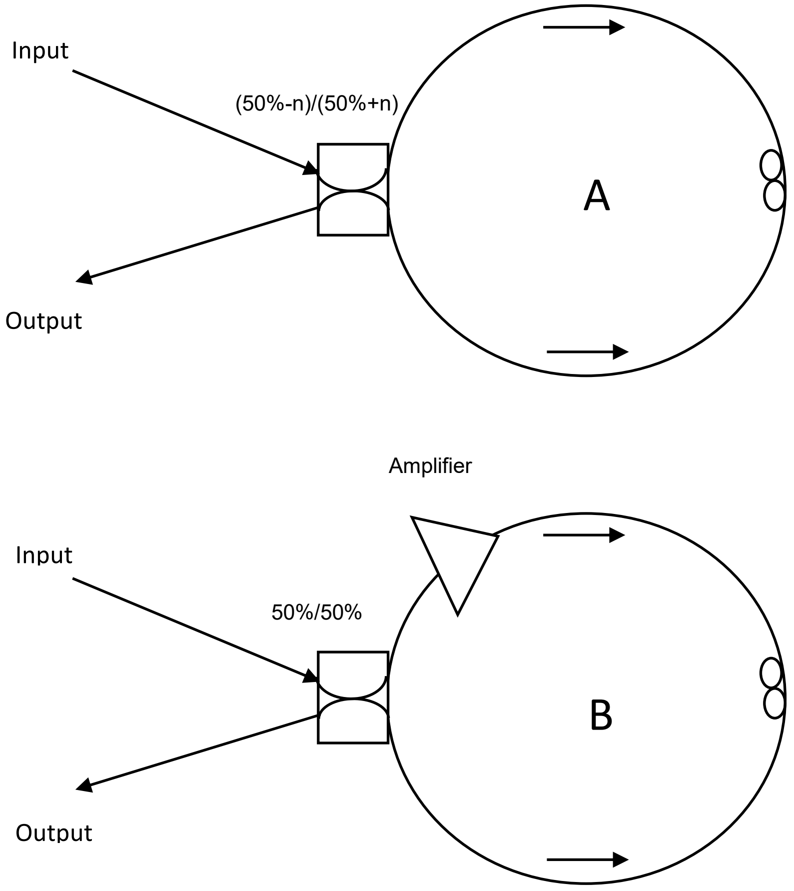

Figure 2-2 Configuration of a NOLM(A) and NALM(B)

The optical replicas with unequal intensities acquire a differential phase shift, due to the nonlinear refractive index. For example, in FIG. 2A, the coupler splits light intensity of the signal between (50 – n) % (Icc) carried in the counterclockwise propagating replica with intensity Icc and (50 + n) % (Ic) in the clockwise replica. Thus, if Ic of the clockwise replica is sufficiently intense to trigger a nonlinear response of the fiber, i.e., to induce SPM, and Icc of the other replica is low, a significant differential phase shift will accumulate between the parts of counter-propagating replicas having different instant intensities. After propagation and on recombination at the fused coupler, the signals interfere with one another. With imbalanced intensities leading to different phase shifts throughout the two pulses, phase interference leads to a resultant shorter pulse.

The lasers, configured in accordance with interferometric mode-locking architectures, represent a relatively new, rarely used structure which renders the discussion about practical advantages or disadvantages of this particular approach rather difficult. However, the NOLM/NALM architecture, like the NLPR may not have the desired stability, i.e., the output pulses may not be reproducible, leading to unacceptable laser performance. Furthermore, the NOLM/NALM architecture, like NLPR, is neither simple nor particularly more cost-effective in comparison with the other designs.

Another method to obtain passively mode-locked laser generation is to use some kind of physical saturable absorber. At present, there are several effective types of the saturable absorbers and respectively two types of appropriate fiber lasers particularly in 1 μm range. SESAM (Semiconductor Saturable Absorber Mirror) mode-locked fiber laser, Carbon nanotube mode-locked fiber laser and Graphene mode-locked fiber lasers.

Over the past twenty years, the semiconductor saturable absorbing mirror or SESAM based on substrates like InGaAs/GaAs-on-GaAs has been successfully deployed in the passive mode locking of bulk solid state lasers and has also been a remarkable scientific and commercial success in the mode locking of fiber lasers [ZIR91] [DES93]. By the nature of the structure of the device it is employed as the cavity mirror in linear or Fabry-Perot type laser cavities, a schematic of which is shown in figure 2.3(a). Figure 2.3 (b) shows the reflection/ absorption of a representative device consisting of alternating 5nm InGaAs and 10 nm GaAlAs barriers. Highly stable, self-starting mode locking of fiber lasers using SESAM technology throughout the near infra-red has been achieved, generating picosecond and femtosecond pulses.

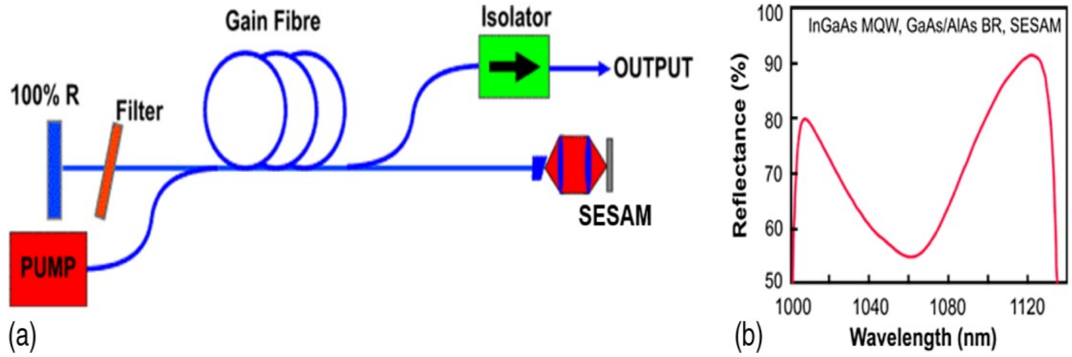

Figure 2-3 (a) Schematic of a passively mode locked fiber laser incorporating a SESAM and (b) the reflection/absorption profile associated with a SESAM for operation in the 1060 nm spectral region.

The key disadvantage of such type of mode-lock lasers is the long term reliability. Unfortunately, the semiconductor materials used as an absorber tend to degrade, especially at a wavelength of 1 micron and shorter, which makes it problematic to consider such a laser as applicable for mass and especially, industrial use.

The carbon nanotube mode-locked fiber laser [SET04] gives the possibility for a ring configuration and potentially can have better characteristics than the SESAM based laser system, but it has a similar problem with reliability. The plastic host material of the nanotube or graphene saturable absorber is also prone to damage, while exhibiting the additional problem of reproducibility.

The Graphene mode-locked fiber laser uses single but more commonly multiple layer graphene as the saturable absorber. Graphene is composed of a flat single layer of carbon atoms arranged in a 2D lattice through sp^2 hybridization. Bao et al. [BAO09] demonstrated the first passive mode locking of an Er-doped fiber laser, generating ~1 ps pulses of high dynamic range around 1560 nm. Since then the passive mode locking of Yb [ZHA10] and Tm [ZHAN12] fiber lasers using graphene saturable absorbers has been reported, as well as numerous bulk solid state laser systems [SUN12]. Generally, the mode locked performance and reliability problems are relatively similar to those based upon nanotube or SESAM based devices and like both systems

A need therefore exists for a completely new architecture capable of carrying out passive mode locking in a ring cavity pulse generator which has a simple, rugged structure capable of outputting uniform and high-energy sub-nanosecond pulses of light. This was the prime objective of the research and development work reported in the following chapters of this thesis.

3 The concept of the new Cross Filter mode locking technique

3.1 The basic configuration of laser under research

The laser cavity is a ring which consists of two parts effectively making a mirror reflection of one another, see Fig 3.1. below. Each of these parts has a narrow band pass filter, amplifier, fiber coil and output coupler. In fact, it looks like we have arranged a so called "Mamyshev Regenerator" in a ring [MAM98]. The essential difference in our case is that the width and central wavelength of filters are chosen to make them slightly overlap in wavelength see Figs. 3.2 [SAM16].

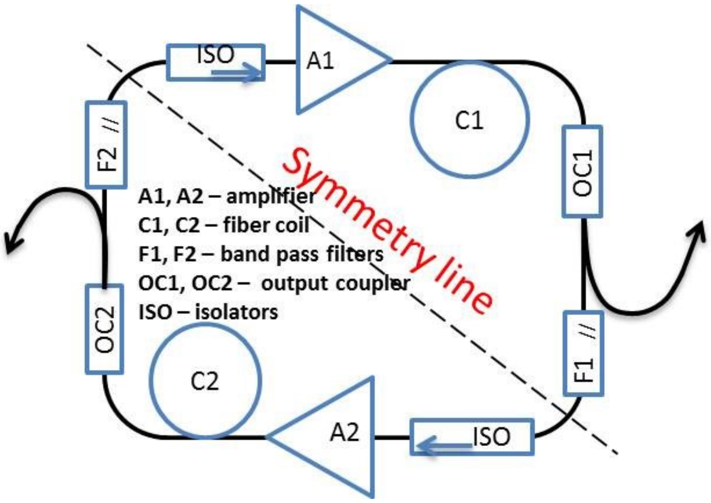

Figure 3-1 A schematic of the proposed fiber laser configuration

Formally, the overall ring laser cavity consists of two linear amplifiers, providing a weak (partial) seeding of one to another.

The polarizing isolator is needed to ensure unidirectional laser operation and selection of the appropriate polarization mode. The output coupler is used for removing useful power out of the cavity. The laser can be built as an all-normal dispersion device or may have components with anomalous dispersion.

In spite of the apparent design symmetry of the sub-cavities, their functionality is sufficiently different. One of the amplifiers provides much higher gain than the other, which creates the conditions for strong pulse broadening due to self-phase-modulation, making the pulse positively chirped and having a broad and smooth spectrum. This spectrum completely fills the pass band of the filter located next to it, so that its replica evolves in the cavity afterwards. The other, lower power pumped amplifier is needed to ensure stable performance, i.e., to lock the laser in a stable equilibrium state when small deviations from this state create an action returning it to the target state. The spectrum reaching the filter located next to the lower pumped amplifier does not fill the pass band of this filter completely, which creates the force returning the laser to the target state when a deviation happens.

In order for the laser pulse to evolve and circulate within such a ring cavity its intensity must be sufficient for the pulse to experience nonlinear spectral broadening and recover in intensity after each pass around the cavity. The combination of two filters having weak spectral overlap works as an effective “saturable absorber”. Weak spectral overlap allows discrimination against CW in favor of a pulse whose intensity is sufficient for spectral broadening. As soon as the peak intensity reaches a level sufficient to broaden the pulse spectrally the losses for the newly acquired spectral components drop as these components are spreading towards the center of filter pass band. The losses for CW stay constant and are very high. Stable and reproducible circulation of the pulse around the cavity may happen without any spectral overlap of the filters at all. The overlap is needed to allow easy start-up of laser pulsing.

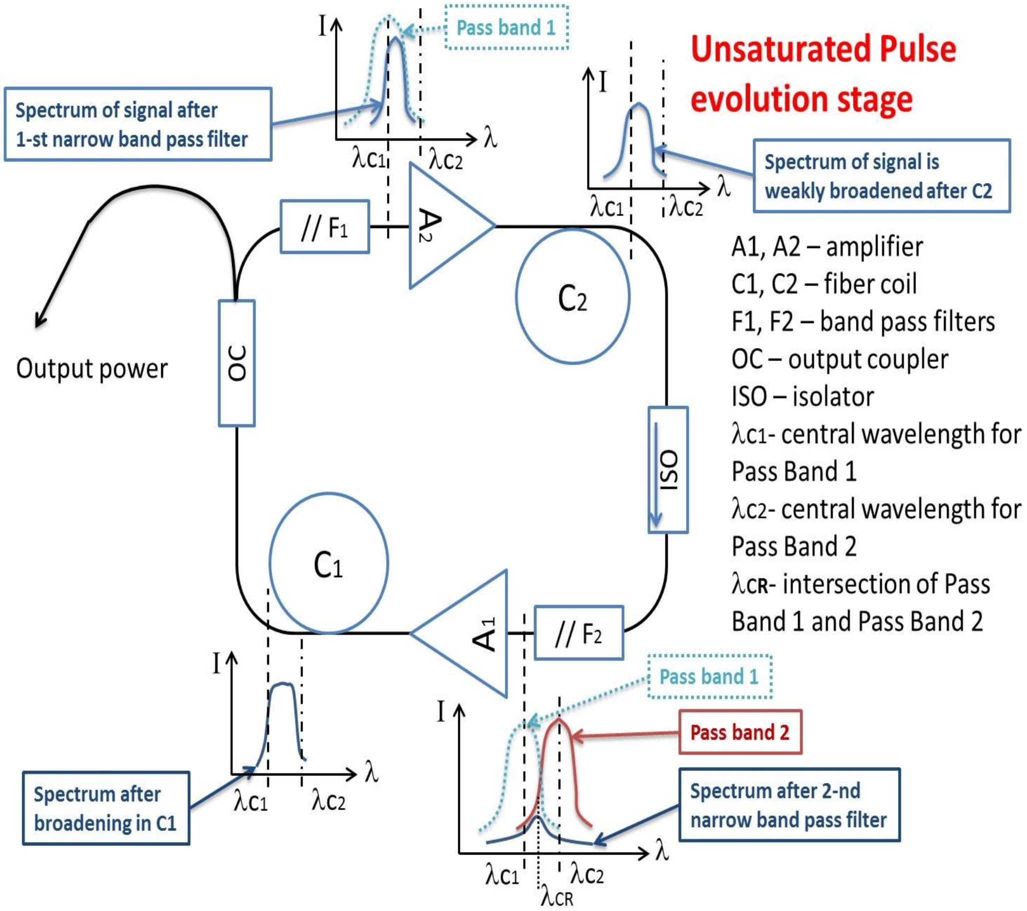

Figure 3-2 Principal architecture of laser under the investigation and pulse evolution during transient "unsaturated broadening" stage.

In contrast to conventional passively mode locked lasers that incorporate a nonlinear element (i.e. the saturable absorber), the ring cavity that was investigated in this present body of work did not have a single additional element which exhibited a nonlinear response. In this configuration, as a pulse propagates through each individual element, the intensity of any given spectral component only changes linearly. The response of the host passive fiber, however, does exhibit a nonlinear response. In fact, it is similar to the situation of the NLPR laser, all the elements in the cavity apart from the fiber show a linear response, and the polarizers are just filters. But in case of NLPR we have to control two effects resulting from nonlinear processes in the fiber, namely nonlinear polarization rotation and spectral broadening, as in our case we are concerned only about a desirable spectrum. Potentially this is much more flexible and stable.

The nonlinear effect in the developed structure is a result of the generation of new spectral components during the pulse evolution inside the fiber of a ring cavity, primarily as a result of self-phase modulation. It is these new spectral components that make the pulse passing through two spectral filters, which are centered on different central wavelengths, have its peak intensity change nonlinearly. The new spectral components make the process of mode synchronization highly competitive, due to low losses for mode locking, compared to other types of generation, like CW operation and Q-switching.

The investigated structure may generate various types of pulses including solitons, similaritons and others and the generation mechanism is particularly beneficial to the generation of ultrashort pulses with a giant chirp. For giant chirped pulse generation, two steps are important for establising a passively mode locked regime for short pulse generation: (a) filtering out a spectrally narrow pulse from a broader pulse, and (b) broadening the thus formed narrow pulse both in the frequency and time domains due to nonlinear effects affecting radiation in a long fiber length. The result of these two steps is a linear positively chirped pulse, i.e., a pulse which is broadened in both spectral and temporal domains as compared to the intial pulse and which has a carrier frequency linearly varying across the pulse. The degree of linearity of the carrier frequency is vitally important for the subsequent compression of such a stretched pulse.

The reason for trying to configure systems to output a chirped pulse is well known to one of ordinary skill in the laser art, as it is the key aspect of chirp pulse amplification, in order to decrease the available peak pulse intensity from lasers (and amplifiers), otherwise deleterious nonlinear effects and optical damage would undermine the operation of the pulse generator (and amplifier). In the chirped pulse amplification scheme the solution to this problem was found by temporal stretching the pulse duration or chirping via dispersion, thus keeping the peak power at a safe level and then, following one or multiple amplifying stages subsequently compressing the stretched and amplified output pulse to the original duration.

The proposed generator of giant chirped pulses is configured with a ring fiber waveguide or cavity guiding light in one direction. The fiber waveguide includes a fiber isolator providing the desired directionality of light propagation within the waveguide. A plurality of fiber components all constituting the device are organized in multiple fiber chains each necessarily including one amplifier, one fiber coil and one spectral filter. During the start-up stage of pulse generation, in response to pulses launched from an external seed source or artificially induced noise by the pumps, spontaneous emission is amplified (ASE) in a first fiber amplifier within the desired spectral range and which is characterized by a continuous wave (CW) component and a pulsed (spike) component or components. Propagating through the first fiber coil, the spike is spectrally and temporally broadened and then spectrally filtered by the first filter. For example, the long wavelength sub-region of the spike is filtered out from further propagation in the desired direction.

The filtered pulsed component is then amplified in a second amplifier to peak intensity sufficient to induce self-phase modulation (SPM) as it propagates through the second fiber coil. The SPM, in combination with linear dispersion, is manifested by spectral and temporal broadenings of the pulsed component and is accompanied by the generation of new frequency components or modes around a center component. Some of the newly generated frequency components partially overlap the frequency bandpass of the second filter which, in contrast to the first filter, cuts off the short wavelength sub-region of the spike. The generation of the new spectral components becomes possible only at certain peak intensities of the spikes, i.e., spikes with synchronized modes, sufficient to induce self-phase modulation.

The circulation of the spike may continue through the first group of the first amplifier, fiber coil and filter combination configured again to respectively amplify, spectrally and temporally broaden and finally filter out the developing pulsed component. The developing spike is finally amplified in the second amplifier to the required peak intensity that the spectrally broadened signal fully covers the bandpass of the second filter. At this point, the spike spectrally develops to the desired signal with a somewhat reduced peak intensity, lost in the second filter but fully compensated in the following first amplifier. The predetermined percentage of subsequent spectrally and temporally expanded signal in the first fiber coil is guided outside the ring waveguide as a pulse with the desired spectral width, intensity and energy to be further following extraction at this point. The output signal can be used as seed source for high power pico-femto laser system or can be compressed as is.

The startup of the described pulse generator requires an external source to create noise which, when amplified, is essential in creating the spectral broadening of the evolving pulse compared to the spectra of continuous wave operation. In the investigated structure, low frequency noise or CW generation cannot be significantly amplified due to the operation of the multiple spectral filters having narrow band-passes, and different central frequencies compared to a steady state spectrum of the pulsed regime. The configuration of the start-up scheme in the pulsed regime depends on a noise-generating technique.

In one start-up scheme, an external source, such as a diode laser, operates as a pump outputting light at a wavelength different from the operating wavelength of the pulse generator. In this embodiment, the described pulse generator is configured with spectral filters that have overlapped bandpasses. This configuration of the filters provides the discrimination of CW narrow line generation, which may be spontaneously formed from quantum or other type of noise, and/or of Q-switch pulses with a prohibitively high energy.

However, the CW component plays an important role in the proper functionality of the pulse generator during the transient stage of laser mode locking. The amplifiers are each characterized by a significant accumulation of energy. A spike passing through these amplifiers may have prohibitively high peak intensity at the amplifier’s output which can lead to complete destruction of not only the pulse generator but also the following amplifying stages. To somewhat decrease this accumulated energy, it is desirable to reduce the population inversion in the gain medium. This is realized by the CW component that may be provided with a significant gain to reduce the overall accumulated energy in the amplifiers. The reduced accumulated energy contributes to a decreased pulse peak intensity and energy of the spike. Having the unfiltered spectral region formed between the overlapped bandpasses of respective filters allows the CW component to be guided through this region along the ring waveguide and accomplish the reduction of accumulated energy.

A further aspect of the embodiment featuring the CW pump relates to the amplification of spontaneous emission in the desired spectral region allowing the spike to pass through the predetermined (and uniform) spectral width of both filters. Such amplification in the desired spectral region is assured by a special form of pump radiation. Initially, the pump output is controlled to emit a high-power, short duration (tens of microseconds to millisecond) pump pre-pulses to initiate noise within a required spectral region. The pre-pulse is thus needed to populate phase space of the noise distribution in the frequency and time domains. Subsequently, a current signal at the input of the pump is interrupted and the energy provided in the pre-pulse(s) is sufficient to amplify one or more small intensity peaks within the desired spectral region corresponding to the bandwidth of both filters. Thereafter, the pump outputs CW radiation with an amplitude lower than that of the initial pump signal(s) which allows the spike to develop into the desired signal and establish the mode-locked regime.

In an additional embodiment, the start-up scheme is provided with a seed launching a starting pulse or pulses at the operating wavelength of the pulse generator. These pulses are guided along the ring waveguide at a repetition rate that can be the same as or different from spikes generated in the ring waveguide in response to pump light from a pump which is turned on sometime after the seed. After the seed is switched off these etalon pulses disappear, but not before the excess of energy stored in the amplifiers is reduced to appropriate safety levels to prevent the generation of Q-switched pulses. In this embodiment the filters may or may not have their respective bandpasses overlap.

In a steady self-starting regime of generation of dissipative solitons or similaritons, the disclosed pulse generator operates similarly to other ring architectures, such the NOLM/NALM and NLPR, each having an individual nonlinear element. This is because in the stable regime, such an element does not substantially affect the evolution of a pulse but is necessary only for the pulse formation from noise. But in the stable regime, the proposed pulse generator is operative to output the desired chirped pulse at most once each round trip, which is in contrast to linear cavities where signal light repeatedly passes through the cavity. In other words, there are no spectral components which can pass the ring more than once without absorption on the filters (almost). The realization of such an output includes either one output coupler positioned immediately downstream from either of fiber coils or two output couplers which are located immediately downstream from respective fiber coils. In the case of two output couplers, the chirped pulse is coupled out of the ring waveguide each half a round trip.

3.2 Laser start-up

Pulse initiation is an important if not the critical problem for a mode-locked laser. Such lasers are usually CW pumped and in general emit a narrow CW line until special conditions, favorable for the mode-locking, are satisfied. These conditions may depend on a number of factors and may not be easily reproducible. The easiest implementation of mode-locking happens for lasers with a real saturable absorber, whereas a laser utilizing nonlinear polarization rotation requires a special procedure for searching for the favorable conditions that may take up to a minute of more, and these conditions may change from time to time. NALM/NOLM lasers may require special assisting devices to ensure start on-demand. The mode-locked pulse evolves from a noise spike or spontaneous mode beats. In our case we utilize pump modulation to create noise in the cavity to increase the probability of mode-locking within a short time scale, (less than a second), which allows start-up of the laser, in fact, on demand. For the purpose of pulse initiation, we modulate the pump source with a train of pulses of microsecond duration at tens of kilohertz repetition rate (schematically shown in Fig.3.3). The train of such pump pulses, having duration much shorter than the life time of the active centers induces stimulated emission and dissipative processes creating broad band noise, which eventually causes mode beats capable of evolving into the steady-state pulse. Simultaneously, this train of pump pulses is safe for amplifiers which cannot accumulate energy sufficient for the evolution of a Q-switched pulse due to the weakness of pump energy delivered in one pump pulse and in the complete train of pulses. Application of a train of pump pulses with 25 microsecond pulse duration and a 50% duty cycle induces evolution of pulses which are characterized by a relatively broad spectrum, inherent to mode-locked operation, but having a quite long nanosecond duration which allows attributing them to the Q-switch process. These pulses have high peak intensity and carry a lot of energy which nevertheless is safe for laser operation. Such transient pulses create the noise required which is sufficient to evolve into mode-locked pulsed operation. When such a transient pulsing is induced, the application of the CW pump at a predetermined and optimized intensity switches the laser output to the purely mode-locked operation, with the switching happening on a sub-microsecond scale.

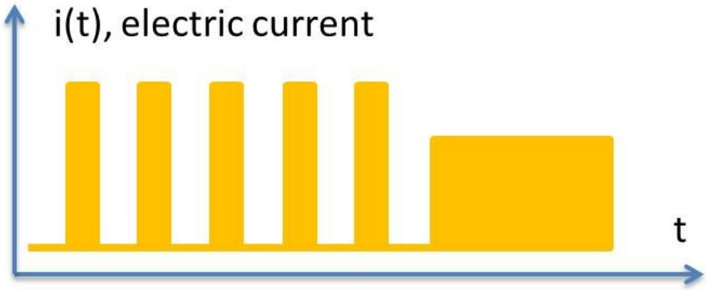

Figure 3-3 . Schematic of the "laser initiation" excitation pump pulse profile

Thus, during the startup, the laser represents a system with a high gain to compensate for the high losses which are intentionally introduced to discriminate against CW operation. However, the level of this high gain and the mode of pumping are insufficient to induce pure Q-switched evolution in cavity, which makes the laser start safely, in terms of potential laser induced damage. Upon the end of the start-up process the gain becomes quite moderate.

To understand the mechanism of pulse formation in the cavity let us follow step-by-step the evolution process with reference to the system configuration shown in Figure 3.2. Broad band spectral noise induced by pulsed, high intensity modulation of the pump source causes mode beats, resulting in the formation of relatively long in time and spectrally narrow noise spikes, having higher intensity than the rest of the noise present in cavity at that moment. This corresponds to the location between Filter 1, having a blue shifted band with respect to spectral bandwidth of the evolving noise, and Amplifier 2 (see Figure 3.2). At that instant, the high intensity pump modulation is turned off and the CW pump is applied. A noise spike of dominating intensity propagates through the cavity without any changes until it reaches Amplifier 1. When amplification is sufficient to raise the peak intensity of this spike to the level where it starts experiencing self-phase modulation due to the Kerr nonlinearity of material, the spike will transform into a pulse, having even longer duration and broader spectrum due to broadening in the fiber coil C2, (as shown on Figure 3.2). The pulse subsequently experiences linear losses at the Isolator. The band pass filter F2 represents a red shifted band with respect to the spectral bandwidth of the evolving pulse and consequently the blue fraction of the pulse will be blocked by this filter, truncating the pulse temporarily and spectrally. Only the red edge of the pulse passes the filter F2, as shown schematically in Figure 3.2 and this portion of the pulse has a much higher level of coherence than the noise spike had before it was amplified by A2. Amplifier 1 increases the pulse energy to a level sufficient for further nonlinear broadening which takes place in the fiber coil C1, after which the pulse further spectrally broadens. Then, filter F1, which has the blue-shifted pass band with respect to filter F2 transmits the blue edge of pulse after the broadening processes in C1.

3.3 Seed laser tests in configuration with stretcher and compressor.

Laser operation can be characterized by a mode-lock stability island which may not be readily and directly achievable by single step conversion from the transient oscillating state. Moreover, there are usually several stability islands and each one is attributed to a specific combination of output pulse parameters and their ranges. For this reason, it may take several steps, each characterized by a specific intensity of the CW pump and the duration of the exposure at that intensity to reach the desired stability island. Once trapped within the specific island, the laser remains stable within a broad range of pump parameters. Upon reaching some threshold value, the pulse peak intensity stays constant and the spectrum experiences significant broadening with an increase in the pump intensity, see Figure 3.4.

The spectrum has a plateau region where it does not show modulations and where the chirp is very close to linear, Figure 3.4 (left). This region is very convenient for use with amplifying systems as it allows linear stretching-compressing components to be efficiently used for obtaining high energy pulses with duration close to transform limited and with no parasitic satellites. Simple, highly reliable components like Fiber Bragg Gratings (FBG) can be used for pulse stretching and simultaneous spectral filtering to ensure the best coupling with the amplification system. Figure 3.5 shows the spectrum and pulse waveform obtained after stretching the broadband pulse with simultaneous spectral filtering (truncation) by the FBG. The spectrum reflected by the FBG has very smooth spectral and temporal envelopes, favorable for high gain amplification. Apodization of the FBG is the parameter responsible for the envelope shape which allows mitigation of parasitic effects during high gain amplification. If the laser spectrum is broad enough to fill the bandwidth of the FBG which is simultaneously a pass band filter, then further increase of laser output power results in a broader output spectrum, but the output of the stretcher remains almost constant in terms of spectrum and power.

The laser spectrum broadens with increasing pump intensity and may increase up to 50 nm and more. The spectra presented below were recorded using an Anritsu 9740A optical spectrum analyzer, operated with a spectral resolution of 0.07 nm and the highest acquisition speed to reveal any possible instability. The stronger pump intensity gives the broader spectrum and the lower modulation induced on it. An Agilent ultrafast optical sampling oscilloscope equipped with a 40 GHz optical head was used to examine the pulse train stability. The signal was continuously accumulated for a minimum of 10 minutes for the purpose of statistical measurement. The train of output pulses was found to be very stable, achieving 0.3% RMS stability and 2% peak-to-peak stability, see Figure.3.6.

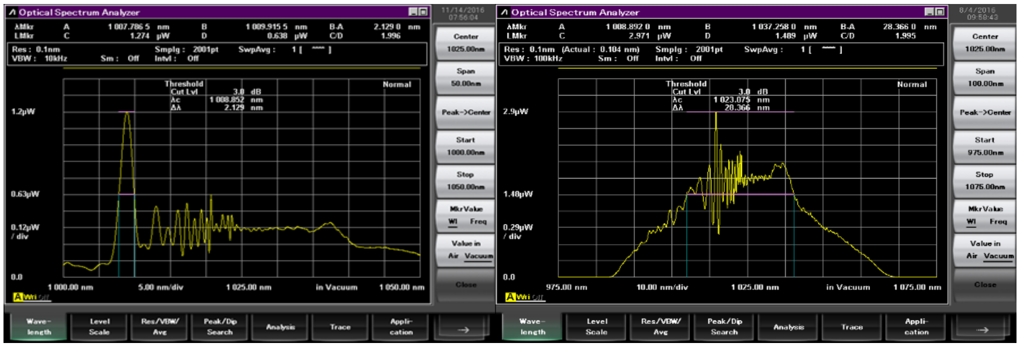

λMkr A 1 007.786 5 nm B 1 009.915 5 nm B-A 2.129 0 nm
LMkr C 1.274 pW D 0.638 pW C/D 1.996
Res : 0.1nm Smplg : 2001pt SwpAvg : 1 [----]
VBW : 10kHz Sm : Off Intvl : Off
Threshold Cut Lvl 3.0 dB
λc 1 008.852 nm
Δλ 2.129 nm
Center 1025.00nm
Span 50.00nm
Start 1000.00nm
Stop 1050.00nm

λMkr A 1 008.892 0 nm B 1 037.258 0 nm B-A 28.366 0 nm
LMkr C 2.971 pW D 1.489 pW C/D 1.995
Res : 0.1nm (Actual : 0.104 nm) Smplg : 2001pt SwpAvg : 1 [----]
VBW : 100kHz Sm : Off Intvl : Off
Threshold Cut Lvl 3.0 dB
λc 1 023.075 nm
Δλ 28.366 nm
Center 1025.00nm
Span 100.00nm
Start 975.00nm
Stop 1075.00nm

Figure 3-4 Examples of the laser output spectra under high (left) and low (right) pump intensity.

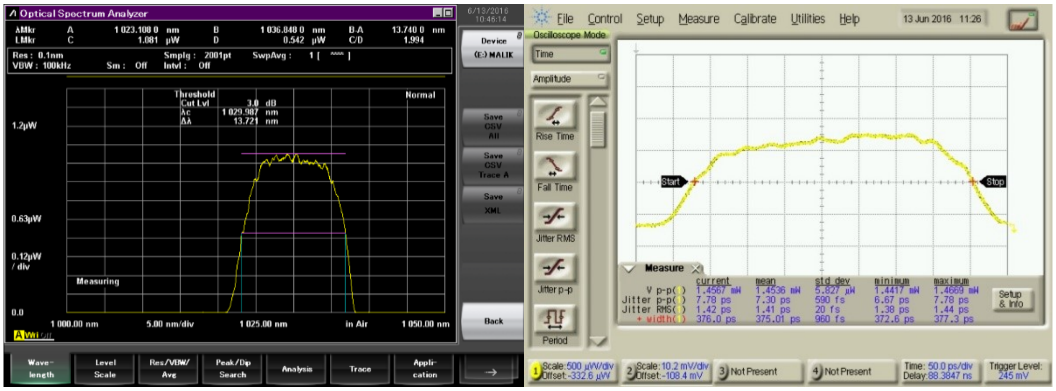

ΛMkr A 1 023.108 0 nm B 1 036.848 0 nm B-A 13.740 0 nm
LMkr C 1.081 μW D 0.542 μW C/D 1.994

Res : 0.1nm Smplg : 2001pt SwpAvg : 1 [^^^^]
VBW : 100kHz Sm : Off Intvl : Off

Threshold
Cut Lvl 3.0 dB
λc 1 029.987 nm
Δλ 13.721 nm

	current	mean	std dev	minimum	maximum
V p-p(1)	1.4567 mW	1.4536 mW	5.827 μW	1.4417 mW	1.4669 mW
Jitter p-p(1)	7.78 ps	7.30 ps	590 fs	6.67 ps	7.78 ps
Jitter RMS(1)	1.42 ps	1.41 ps	20 fs	1.38 ps	1.44 ps
+ width(1)	376.0 ps	375.01 ps	960 fs	372.6 ps	377.3 ps

1 Scale: 500 μW/div Offset: -332.6 μW
2 Scale: 10.2 mV/div Offset: -108.4 mV
Time: 50.0 ps/div Delay: 88.3847 ns
Trigger Level: 245 mV

Figure 3-5 Spectrum and pulse temporal waveform after stretching the pulse with a Fiber Bragg Grating (FBG). Left: spectrum reflected by FBG. Right: waveform of pulse stretched by FBG.

The temporal profile of output pulse varies with the pulse evolution which is strongly affected by the Kerr nonlinearity. The spectral shape and bandwidth of the bandpass filters also has an impact on the pulse evolution and can be used as an independent parameter for mitigating pulse break up and chirp nonlinearity under high gain conditions. A typical spectral profile of the radiation coupled out of the cavity just after the filter is shown in Fig.3.8. The small dip close to the spectral peak is a result of pulse deformation during the evolution without amplification. This shown spectral component when exposed to appropriate amplification experiences nonlinear broadening. Depending on the magnitude of the amplification the broadening results in a representative output spectra as shown in Figure 3.4. The output pulse is close to Gaussian at low pump intensity with output pulse energies < 1 nJ and pulse durations < 5 ps and becomes square at high pump intensities when the pulse energy exceeds 7 nJ and pulse broadens to more than 10 ps, see Figure 3.7.

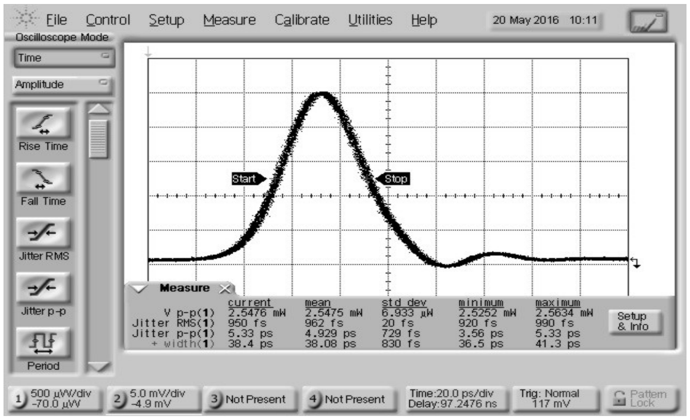

20 May 2016 10:11

```
                 current      mean         std dev     minimum      maximum
     V p-p(1)    2.5476 mW    2.5475 mW    6.933 µW    2.5252 mW    2.5634 mW
Jitter RMS(1)    950 fs       962 fs       20 fs       920 fs       990 fs
Jitter p-p(1)    5.33 ps      4.929 ps     729 fs      3.56 ps      5.33 ps
   + width(1)    38.4 ps      38.08 ps     830 fs      36.5 ps      41.3 ps
```

1 500 µW/div -70.0 µW
2 5.0 mV/div -4.9 mV
3 Not Present
4 Not Present
Time:20.0 ps/div Delay:97.2476 ns
Trig: Normal 117 mV

Figure 3-6 Output pulse train stability. RMS < 0.3%, P-to-P < 2%

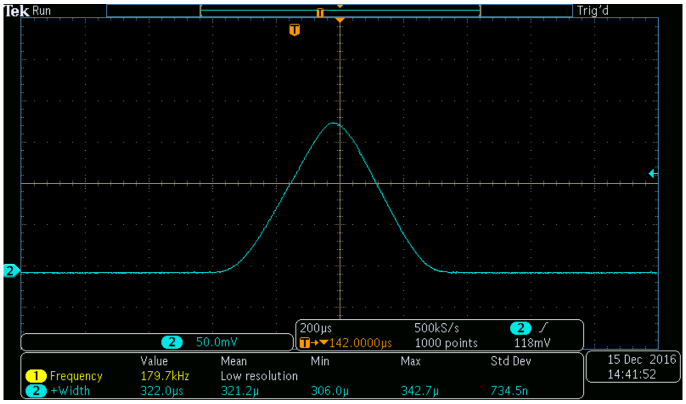

2 50.0mV
200µs 500kS/s 2 118mV
T→142.0000µs 1000 points

```
               Value      Mean             Min       Max       Std Dev
1 Frequency    179.7kHz   Low resolution
2 +Width       322.0µs    321.2µ           306.0µ    342.7µ    734.5n
```

15 Dec 2016
14:41:52

Figure 3-7 Autocorrelation, indicating a square pulse, FWHM 10 ps.

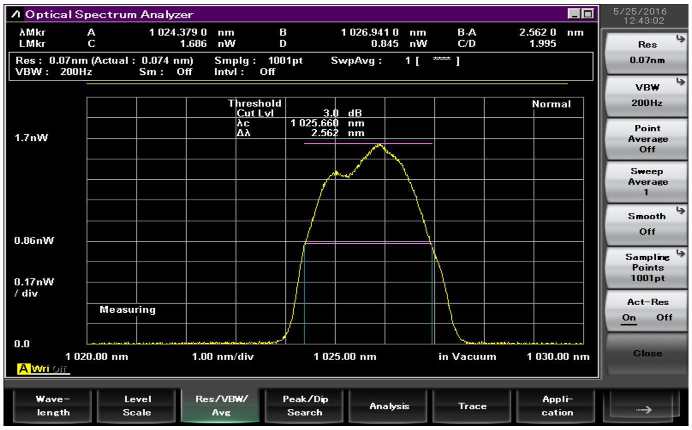

5/25/2016
12:43:02

```
λMkr   A   1 024.379 0  nm    B   1 026.941 0  nm    B-A   2.562 0  nm
LMkr   C       1.686    nW    D       0.845    nW    C/D   1.995
Res :  0.07nm (Actual :  0.074 nm)   Smplg :  1001pt   SwpAvg :   1 [  ***  ]
VBW :  200Hz           Sm :  Off     Intvl :  Off
```

```
Threshold
Cut Lvl          3.0  dB
λc       1 025.660    nm
Δλ           2.562    nm
```

Figure 3-8 Spectral replica of band pass filter coupled out of cavity after the filter.

Nonlinear evolution of this replica eventually broadens to generate output spectra as shown in Figure 3.4.

Nonlinear evolution of the pulse for the purpose of spectral broadening and temporal expansion may cause significant spectral phase destortion across the pulse which will affect the pulse compressibility and thus usefullness of the source. In the extreme case it is possible to observe pulse break up due to a strong nonlinear phase, or spectral chirp, acquired through intense pulse broadening. In order to examine the output laser pulse properties after significant spectral broadening acquired as a result of nonlinear evolution the MIIPS (multiphoton intrapulse interference phase scan) methodology of phase analysis was implemented using a FemtoJock phase modulator manufactured by IPG Photonics. In the experiment only a 17 nm fraction of the output spectrum was subject to analysis ,which constitutes the maximum range available for the device at present within the wavelength range of interest, see Figure 3.9. We demonstrate below the fraction of the output spectrum that was analysed and the autocorrelation recorded as a result of pulse compression achieved by means of this pulse shaper. The output pulse showed a high level of chirp linearity and perfect coherence which resulted in compressibility to the transform-limited pulse duration. The measured autocorrelation allowed an estimation of the FWHM of pulse to be 135 fs, assuming a Gaussian pulse shape or 200 fs if a square pulse shape was inferred. The Fast Fourier Transform tool provided as a part software package serving the pulse shaper yielded a FWHM=155 fs for the transform limited pulse, simply by transforming the measured spectrum. The result showed very good compressibility for the selected fraction of spectrum. The compressed pulse also had a temporal shape closed to Gaussian and showed no presence of parasitic satellite pulses.

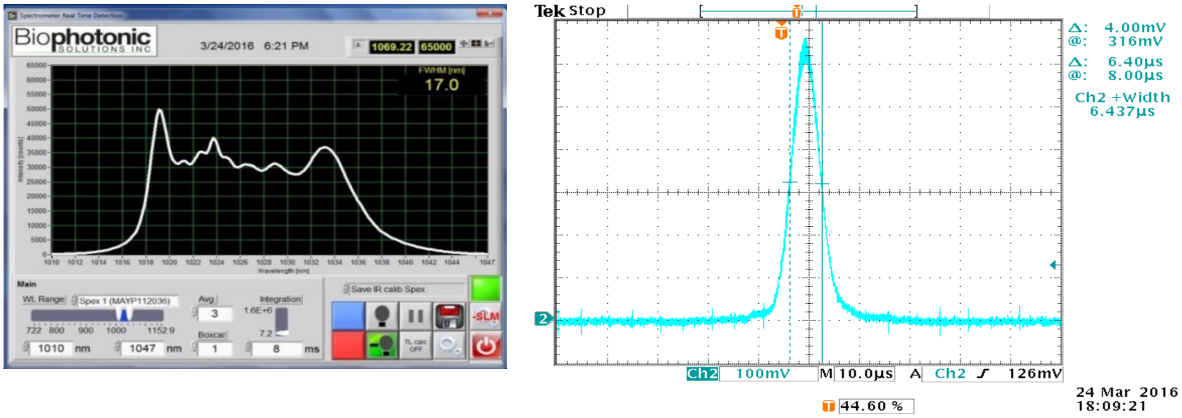

Figure 3-9 . Pulse shaping using MIIPS methodology and a FemtoJock pulse shaper. The fraction of the output spectrum selected for shaping (left), autocorrelation of the shaped pulse (right) having FWHM=135 fs when Gaussian calibration is applied or FWHM=200 fs for square pulse calibration.

4 Modeling of Cross-filter Femtosecond Fiber Laser.

4.1 Schematic of the laser

A theoretical model of the Cross-filter Femtosecond Fiber Laser based on the solution of the equation describing the evolution of the electric field of the coherent laser pulse in the cavity has been developed. A schematic of the elements incorporating the laser is shown in figure 4.1.

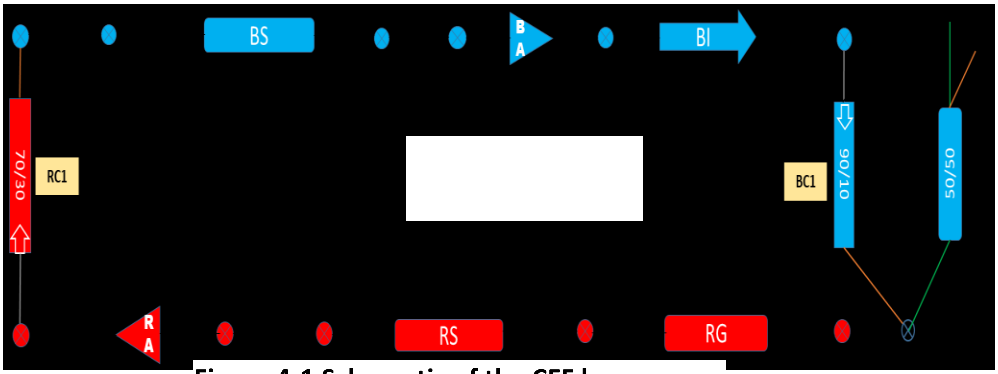

Figure 4-1 Schematic of the CFF laser.

In this scheme, RG and RS are Red Gaussian and Red Square filters. BS is a Blue Square filter. The transmission and phase distortions of these filters have been measured experimentally and the relevant parameters are included in the model, the results of which are very sensitive to the spectral characteristics. RC, BC and BI are a Red Coupler, a Blue Coupler and a Blue isolator (to prevent counter propagation). Almost all the parameters used in the model of the system (fibers and filter characteristics) have been measured, but some, for example the inversion of amplifiers, are impossible to measure. A reasonable variation of parameters has also been tested and those which have best fit with experimental observations were used. For example, the spectral transmission of filters were all fully measured and calibrated, however, the phase distortions were measured over a smaller spectral region and the with the performance projected to cover the unknown regions. In addition, the doping and amplification of RA and BA have been measured, but the exact profile of excitation along the fiber is calculated below.

4.2 Theoretical model of the pulse propagation.

4.2.1 Main equation

In this approach the real, fast oscillating electric field of the optical pulse $E(z,t)$ is written as the slow complex modulated envelope $A(z,t)$ and its complex conjugate $\overline{A(z,t)}$ along of the fiber length z:

$$E(z,t) = A(z,t)e^{-i\omega_0 t} + +\overline{A(z,t)}e^{i\omega_0 t} \quad (1)$$

The main equation which we solve is the following:

$$\frac{\partial A}{\partial z} = \frac{g-a}{2}A - \beta_1\frac{\partial A}{\partial t} - i\frac{\beta_2}{2}\frac{\partial^2 A}{\partial t^2} + i\frac{\beta_3}{6}\frac{\partial^2 A}{\partial t^2} + i\gamma\left[|A|^2 - T_R\frac{\partial |A|^2}{\partial t} + iT_S\left(\bar{A}\frac{\partial A}{\partial t} + \frac{\partial A\bar{A}}{\partial t}\right) + (\nu - i\mu)|A|^4\right]A \quad (2)$$

This equation is a combination of the standard Cubic-Quintic Complex Ginzburg-Landau Equation [AGR13] with the addition of the last term which takes higher order nonlinear effects into account [AKH05]. We analyzed solutions of this equation including all terms and found that under our conditions, the effects of linear and nonlinear absorption (*a*), cubic frequency dispersion (β_3), nonlinear front steepening (T_S) and high order nonlinear absorption and phase modulation ($\nu - i\mu$) can be neglected. The term in square brackets is nonlinear in respect to *A*, where the main nonlinear optical effect is self-phase modulation, which is included using the parameter $\gamma = \frac{2\pi n_2}{\lambda_0 A_w}$, where the index of refraction $n = n_0 + n_2 I^2$ depends on the intensity and n_2 is the real, positive nonlinear index of refraction of second order. In the case of single mode fiber, the radial distribution of the field can be approximated using the Gaussian distribution $E(r) = Ee^{-2\frac{r^2}{r_w{}^2}}$,with the effective radius of the fiber r_w and $A_w = \frac{\left(\iint_{-\infty}^{\infty}|E(r)|^2 2\pi r dr\right)^2}{\iint_{-\infty}^{\infty}|E(x,y)|^4 2\pi r dr}$ is the effective area of the fiber, which is used to calculate the nonlinear parameter γ. A small, but detectable and measurable effect is Stimulated Raman Scattering (SRS) which is taken to account using the so-called Raman time T_R in the simplest form in formula (2). After running numerous simulations we found that under our conditions, the best value of T_R is 4.5 fs, which is close to the commonly used experimentally extracted values between 3 and 6 fs. This equation is a simplified by using the so-called retarded time $t' = t - z/v_\mathrm{g} = t - \beta_1 z$ moving with group velocity v_g and in this case we can see how the temporal shape of the envelope $A(z,t')$ changes along the fiber length z.

$$\beta_1 = \frac{1}{c}\left[n - \omega\frac{\partial n(\omega)}{\partial\omega}\right]_{\omega=\omega_0} = \frac{n_g}{c} = \frac{1}{v_g} \qquad (3)$$

The group velocity dispersion is taken to account through the second derivative of the phase

$$\beta_2 = \frac{1}{c}\left[2\frac{dn(\omega)}{d\omega} + \omega\frac{d^2n(\omega)}{d\omega^2}\right]_{\omega=\omega_0} \cong \frac{\omega}{c}\frac{d^2n(\omega)}{d\omega^2} \cong \frac{\lambda^3}{2\pi c}\frac{d^2n(\lambda)}{d\lambda^2} \qquad (4)$$

where the index of refraction of the fiber is a polynomial $n(\lambda) = \sum_{n=1}^{4}(b_n\lambda)^n$ specific to each fiber. We found that terms higher than $\beta_2(\omega_0)$ at the carrier frequency at 1025 nm does have a small effect and should be included for very long fibers.

Under our conditions, we can write the Complex Ginzburg-Landau Equation (CGLE) including Self Phase Modulation and Raman terms proportional to the intensity and can be written as:-

$$\frac{\partial A}{\partial z} = \frac{\mathrm{g}}{2}A - i\frac{\beta_2}{2}\frac{\partial^2 A}{\partial t^2} + i\gamma\left[|A|^2 - T_R\frac{\partial |A|^2}{\partial t}\right]A \qquad (5)$$

For picosecond pulses, where the pulse duration is much longer than T_R, we can neglect the last term and the equation becomes the so-called Nonlinear Schrodinger Equation (NSE)

$$\frac{\partial A}{\partial z} = \frac{\mathrm{g}}{2}A - i\frac{\beta_2}{2}\frac{\partial^2 A}{\partial t^2} + i\gamma|A|^2 A \qquad (6)$$

All these equations are written for the complex electric field amplitude envelope *A* in time domain, but the electric field can be presented also in the frequency domain $= \frac{2\pi c}{\lambda}$. using the complex spectrum of the field at each spatial point *z* detuned from the carrier frequency ω_0 and using the Fourier Transform (FT) of the complex spectrum on detuned frequency $\tilde{A}(z, \omega - \omega_0)$

$$A(z,t) = \frac{1}{2\pi}\int_{-\infty}^{\infty}\tilde{A}(z,\omega-\omega_0)e^{-i(\omega-\omega_0)t}d\omega = FT\{\tilde{A}(z,\omega)\} \qquad (7)$$

$$\tilde{A}(z,\omega-\omega_0) = \int_{-\infty}^{\infty}A(z,t)e^{i(\omega-\omega_0)t}dt = IFT\{A(z,t)\} \qquad (8)$$

This spectrum $\tilde{A}(\omega)$ is calculated using the inverse Fourier transform (IFT) of the envelope of the complex electric field $A(t)$. Using spectral representation is very useful, specifically in the case where the laser amplification per meter $g(z, \omega)$ is spectrally dependent

$$\mathrm{g}(z,\omega) = \left[\sigma_{em}(\omega) n_e(z) - \sigma_{ab}(\omega) n_{\mathrm{g}}(z)\right] n_{Yb}(z) \qquad (9)$$

where the concentration of doping is $n_{Yb}(z)$ and n_e and $n_{\mathrm{g}} = 1 - n_e$ are the populations of the excited and ground states respectively in an effective two level system, with σ_{em} and σ_{ab} the cross-sections of stimulated emission and absorption respectively in the fiber. Also, in this case we can use the spectrally dependent dispersion coefficient per meter:

$$\beta_2(z,\omega) = \frac{1}{c}\left[2\frac{dn(\omega)}{d\omega} + \omega\frac{d^2n(\omega)}{d\omega^2}\right] \qquad (10)$$

The spectral representation of the field $\tilde{A}(z, \omega - \omega_0)$ is also particularly useful because it is practically impossible to measure the intensity of a femtosecond pulse in time domain, but relatively easy to measure the spectrum and compare theoretical prediction with experimental measurement.

$$I(z,\omega - \omega_0) = \left|\tilde{A}(z,\omega - \omega_0)\right|^2 \qquad (11)$$

4.2.2 Fourier method of solution of equation.

To solve these nonlinear differential equations we use the Split Step Fourier Method (SSFM). This method is very well developed and tested, where the differential operator in the time domain $\frac{\partial^2 A}{\partial t^2}$ is replaced by $-\omega^2$ in the frequency domain using the property of the Fourier transform. In this method we calculate the forward propagation along the fiber since the back reflections are negligible in fibers. This allowed us to formulate the task as the so-called Cauchy problem, where we use the initial field in the frequency domain at point z=0 and calculate the evolution of field from point z to the next point $z+h$.

We used the so-called symmetrical second order version of the SSFM, where evolution is split in several steps. On the first step (SSFM.1), the complex spectrum is just multiplied on exponent with a complex phase with real amplification $\mathrm{g}(z,\omega)$ and a complex dispersion $\beta_2(z,\omega)\omega^2$ on half of the spatial step $h/2$. On the second step (SSFM.2), using the Fast Fourier Transform function (FFT) the spectrum is transformed to the field in time domain. The third step (SSFM.3) includes nonlinear optical effects dependent on intensity and the derivative calculated as the time dependent complex phase modulation including Self Phase Modulation $\gamma|A'(z+h/2,t)|^2 h$ and Raman phase shift $\gamma T_R \frac{d|A'(z+h/2,t)|^2}{dt} h$ on full spatial step *h*. On the next step of the algorithm (SSFM.4) the time dependent field is transformed back to the frequency domain using the Fast Fourier Transform (FFT) and multiplied to include spectral amplification and dispersion in the last half step (SSFM.5). The following is the sequence of transformations of the field in spectral domain from initial $\tilde{A}(z,\omega)$ to the next point $\tilde{A}(z+h,\omega)$:

$$\tilde{A}'(z+h/2,\omega) = \tilde{A}(z,\omega)e^{[0.5(\mathrm{g}(z,\omega)+i\beta_2(z,\omega)\omega^2)]h/2} \tag{SSFM.1}$$

$$A'(z+h/2,t) = FFT\{\tilde{A}'(z+h/2,\omega)\} \tag{SSFM.2}$$

$$A''(z+h/2,t) = A'(z+h/2,t)exp\left\{i\gamma\left[|A'(z+h/2,t)|^2 - T_R\frac{d|A'(z+h/2,t)|^2}{dt}\right]h\right\} \tag{SSFM.3}$$

$$\tilde{A}''(z+h/2,\omega) := IFFT\{A''(z+h/2,t)\} \tag{SSFM.4}$$

$$\tilde{A}(z+h,\omega) := \tilde{A}''(z+h/2,\omega)e^{[0.5(\mathrm{g}(z,\omega)+i\beta_2(z,\omega)\omega^2)]h/2} \tag{SSFM.5}$$

In the case of the developing pulse in the cavity, we use a (weak) input pulse to the cavity and after a full trip through the cavity we then use the output field as the input and repeat the calculation observing the evolution of the pulse as it circulates inside the cavity. The static effects of mirrors, couplers, isolators are easily incorporated by additional spectral modulation $M(\omega)$ on the well-defined surfaces (points) of fiber.

4.3 Model of linear dissection of the cavity.

One of the first tests was modeling of the propagation of a pulse in the linear cavity, to check all parameters of the model of the laser. For this model we experimentally measured energies and spectra at several points in the cavity and we adjusted the parameters of the model, primarily the excitation probability of Ytterbium, to match as much as possible, the simulated results with directly measured pulse energies and spectra. In figure 4.2 we demonstrate that using different models of the excitation of the active fiber have some, but not a critical effect, on the energy of the generated pulses.

The main parameter which has the greatest effect on the model is the value of the spatial step, which should be small enough to have the so-called B-integral smaller than 1, which is the phase change induced via nonlinear phase self-modulation

$$Bi(z,t) = \gamma\,|A(z,t)|^2 h \ll 1. \tag{12}$$

Under our conditions the smallest spatial step is in the second amplifier and *h*=1 cm.

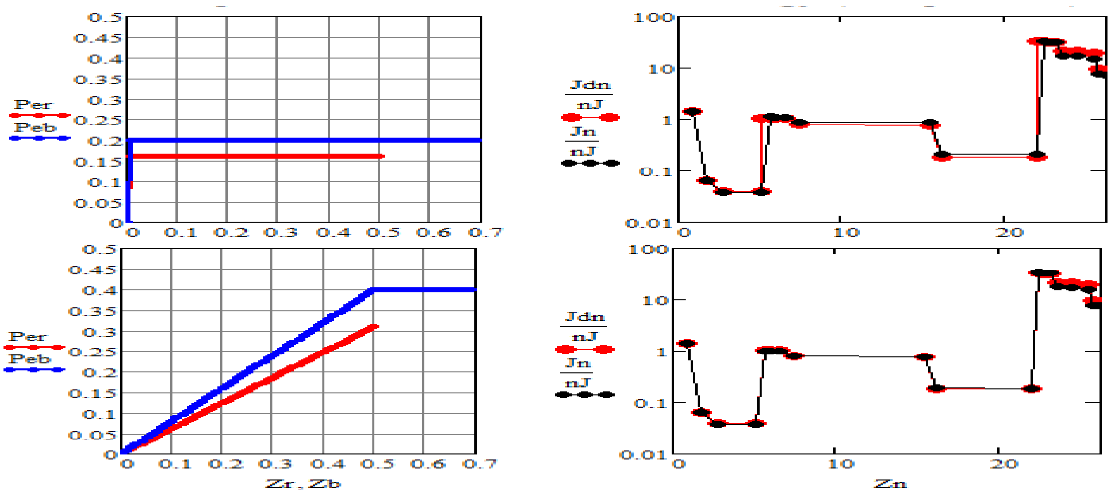

Figure 4-2 . Left hand column illustrates the dependence of the population of the excited states in RA and BA (red and blue amplifiers) normalized, along the fiber in meters. The right hand column displays the pulse energies along the cavity in meters, Black – experimentally measured, Red – calculated.

4.4 Spectral and phase characteristics of the laser components.

The spectral characteristics of the laser and the group velocity delay of components are presented in figure 4.3. The group velocity delay of components was measured using the Phase Shift Modulation method. The table of constants and parameters used in the model are presented in figure 4.4.

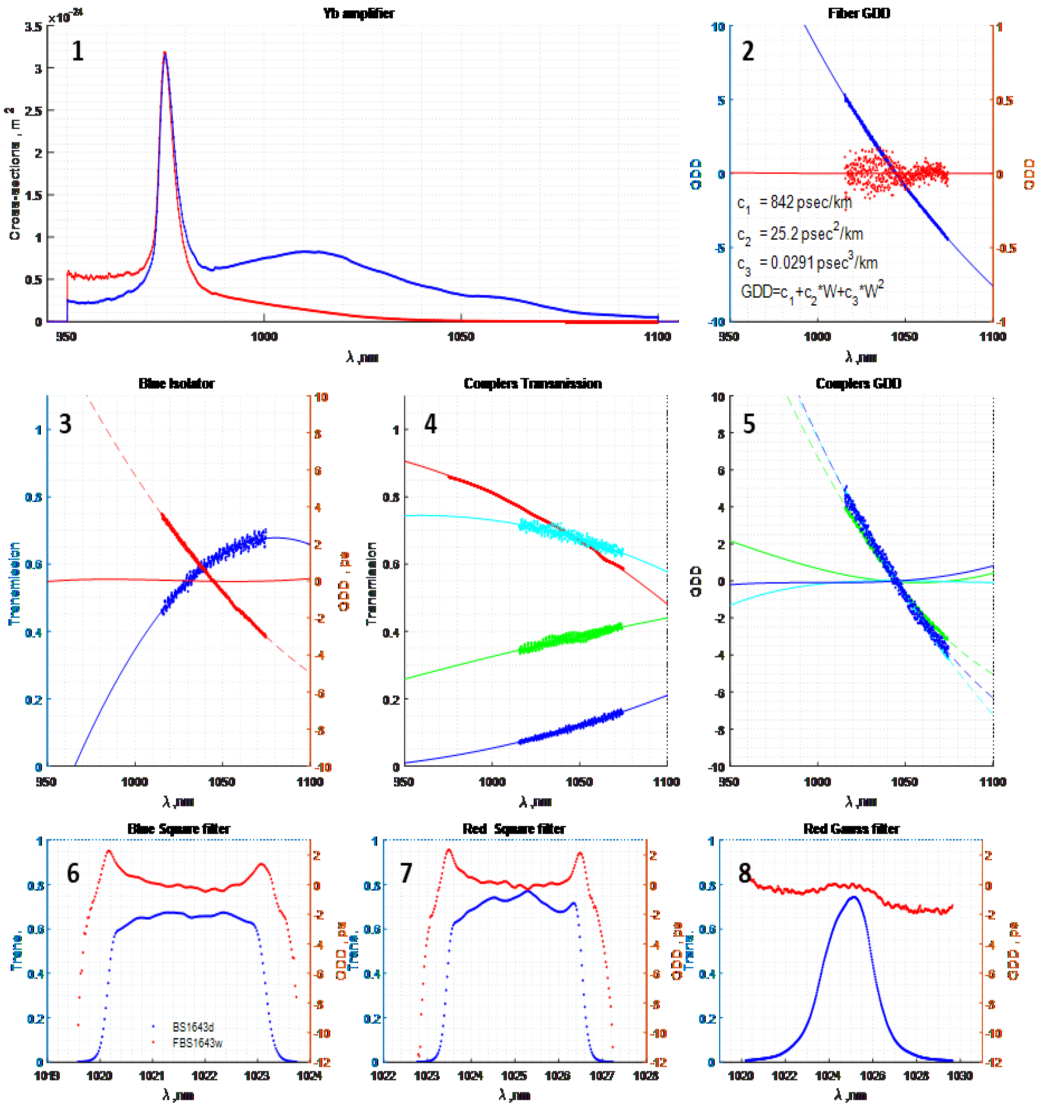

Figure 4-3 Spectral properties of laser' components. 1. Red – absorption and blue – stimulated emission spectra of Yb doped fiber. 2 – Group Delay Dispersion (GDD) of fibers. 3- Transmission and GDD of isolator, 4 Transmission of couplers, 5 – Gdd of couplers. 6,7,8 – measured transmission and GDD of filters.

τ_R	4.5 fsec	Raman time
τ_s	$1/\omega_0$	Self-steepening time
n_2	2.6×10^{-20} m^2/W	Nonlinear index of refraction
γ_2	$2\pi n_2/\lambda_s a_w$	Nonlinear phase index
n_4	2.3×10^{-39} m^2/W^2	Nonlinear index of refraction of second order
γ_4	$2\pi n_4/\lambda_s a_w^2$	Nonlinear phase index of second order
b_2	25.2 ps^2/km	Group velocity dispersion of second order
b_3	2.3 fs$\times b_2$	Group velocity dispersion of third order
λ_p	975 nm	Pump wavelength
λ_s	1023 nm	Mean amplified wavelength
n_{Yb}	2000 ppm^3	Concentration of dopant ions
τ_c	90 ns	Period of the cavity
τ_f	840 μs	Fluorescence time of Yb ion
r_p	62.5 μm	Radius of pump fiber
r_s	4 μm	Radius of doped fiber
r_w	3.25 μm	Effective radius of fibers
Γ_p	$0.5r_s^2/r_p^2$	Filling factor of pump light
Γ_a	$1\text{-}\exp(\text{-}2r_s/r_w)$	Filling factor of amplified light

Figure 4-4 General Parameters used in the model.

4.5 Control of B -integral.

The main parameter to control quality of the solution of the equation is the value of the spatial step, which should be small enough to have the so called B-integral smaller than 1 which is the phase change via nonlinear phase self-modulation

$$Bi(z,t) = \gamma \, |A(z,t)|^2 h \ \ll 1. \qquad (13)$$

In fact, the value of the minimum step was chosen slightly less than the step at which further reduction does not affect the simulation result in any way. In our case, the B-integral should be less than 0.5 at all points of the laser ring

Under our conditions the spatial step smallest in second amplifier is *h*=1cm.

The major parameters of the pulse and the B – integral along the fiber can be seen in Figure 4.5

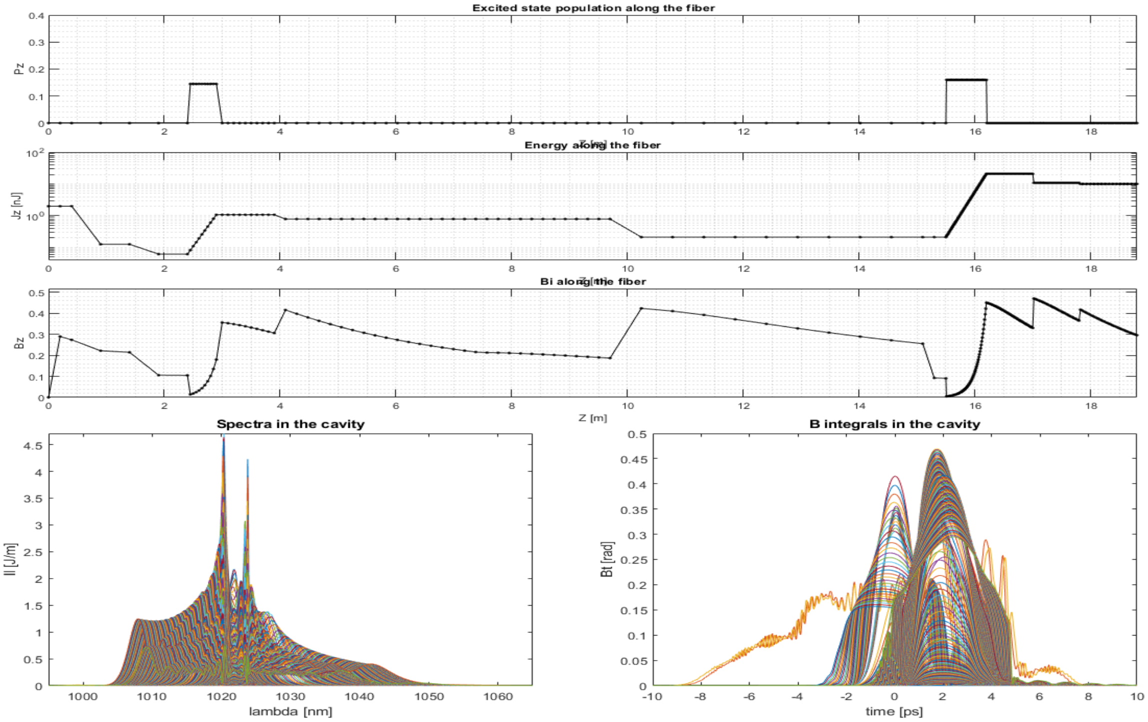

Figure 4-5 . Three upper rows illustrate the dependence of the population of the excited state of Yb, the energy of the pulse (nJ) at each point along the fiber and the maximum value of time-dependent Bi integral along the fiber. The two lower panels present on the left, the calculated spectra (in the wavelength domain) and on the right, the Bi-integral (in the time domain).

3-D plots have also been generated which clearly illustrate the spectral evolution of the pulse as it evolves and propagates around the laser cavity, see Figure 4.6 below.

Using our experimentally measured parameters of the laser and through adjusting the unknown parameters in the model, the output spectrum was calculated, with excellent agreement shown with the experimentally measured spectral profiles, as illustrated in Figure 4.7.

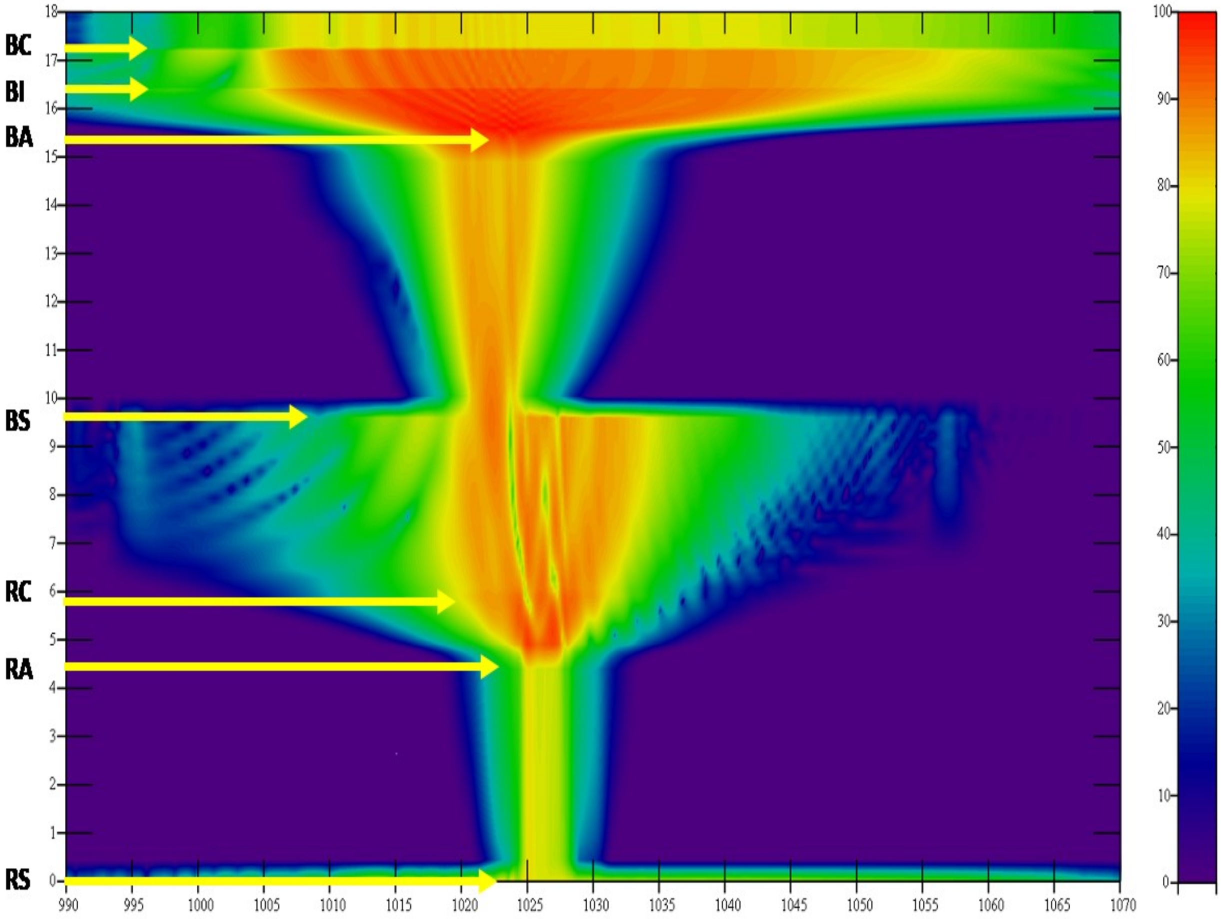

Figure 4-6 Spectral intensity of the pulse (Z - log scale) along the length of the cavity (Y), X axis is wavelength in nanometers.

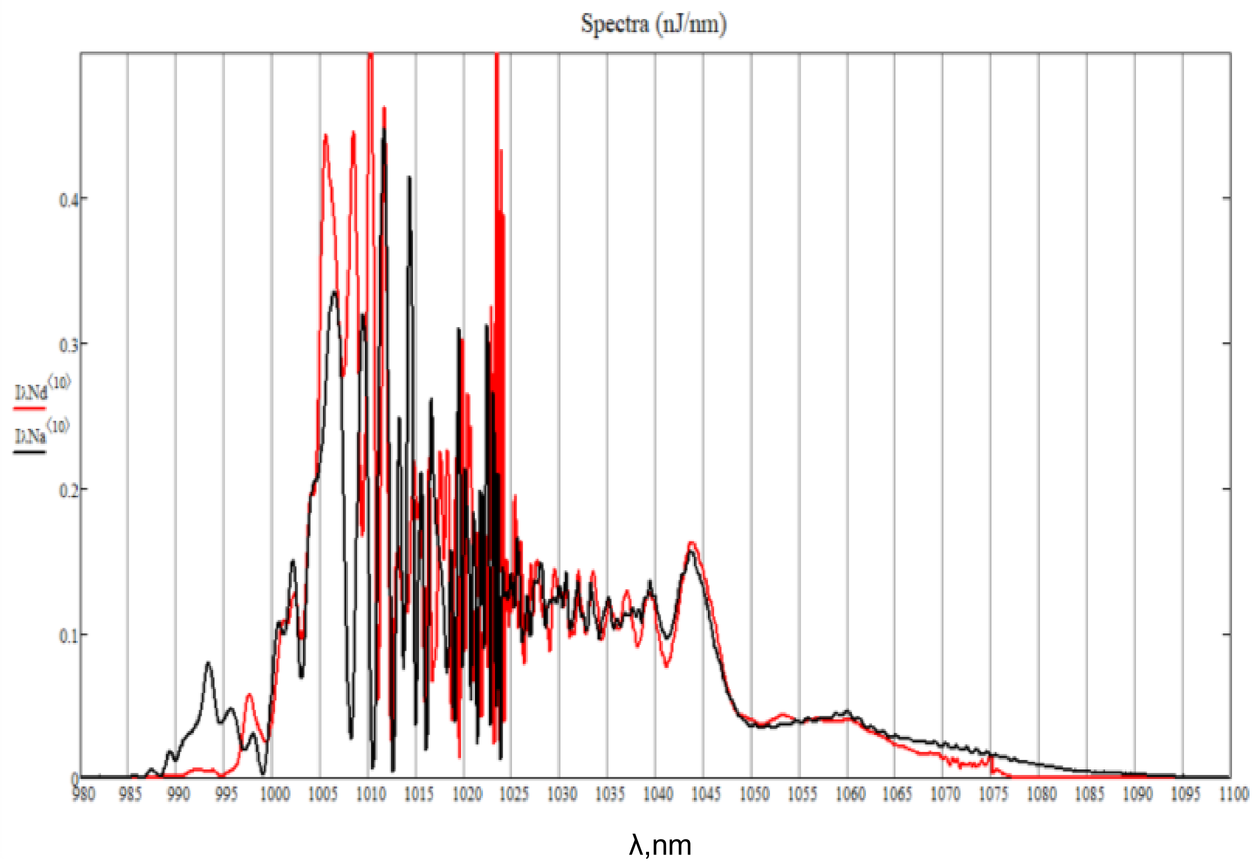

Figure 4-7 Comparison of calculated (red) and measured (black) spectra at the output of the cavity.

4.6 Optimization of the filters in the cavity.

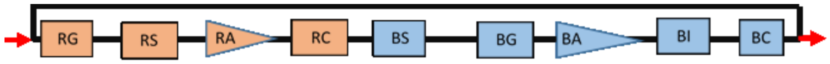

Figure 4-8 Laser cavity composition.

With excellent agreement shown between the experimental and theoretical prediction, the model was used to improve laser performance. For example, we added a narrow filter (BG Figure 4.8) before the second amplifier and eliminate noise-like spectral features of the pulse. In Figure 4.9. we show optimization of the position and width of the additional filter and the resulting spectrum achieved with it.

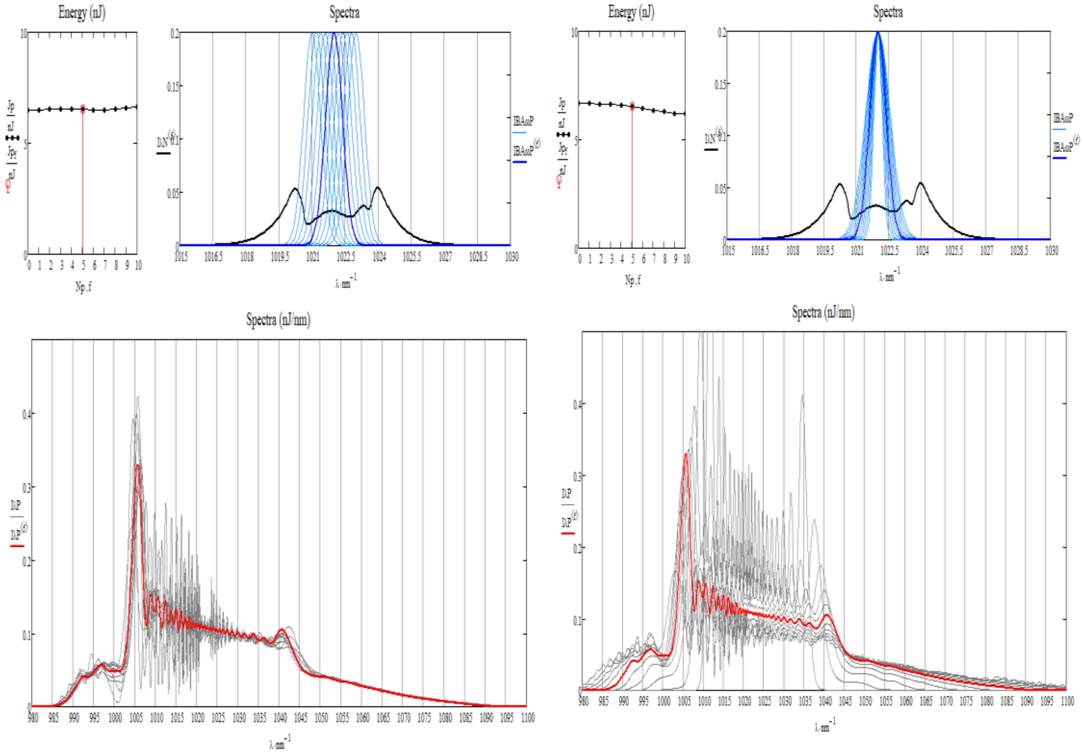

Figure 4-9 Optimization of the additional RG filter to improve output spectrum. First graph is variation of filter position, second is variation of filter width. In the bottom corresponding spectrums with a red is optimized.

4.7 Laser generation stabilization.

In the process of studying the cavity, one feature was found that provides extremely stable laser operation over a wide range of output energies.

In the case when a pulse after the red amplifier, as a result of nonlinear evolution in the fiber, arrives at the input of the blue filter so that the first formed nonlinear lobe hits exactly the filter window (see Figure 4.10), a very stable generation mode is observed. In this case, the gain of the blue amplifier can vary over a wide range without adversely affecting the generation.

Any changes in the power in the resonator lead to a displacement of the lobe with respect to the filter and leads to negative feedback on the loss of the filter.

Thus a kind of lock is implemented for the generation mode (Figure 4.11).

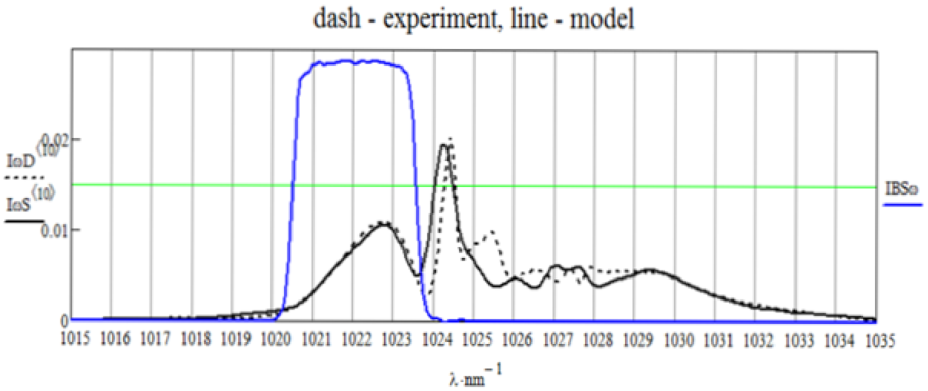
dash - experiment, line - model

Figure 4-10 Lock of generation on blue filter.

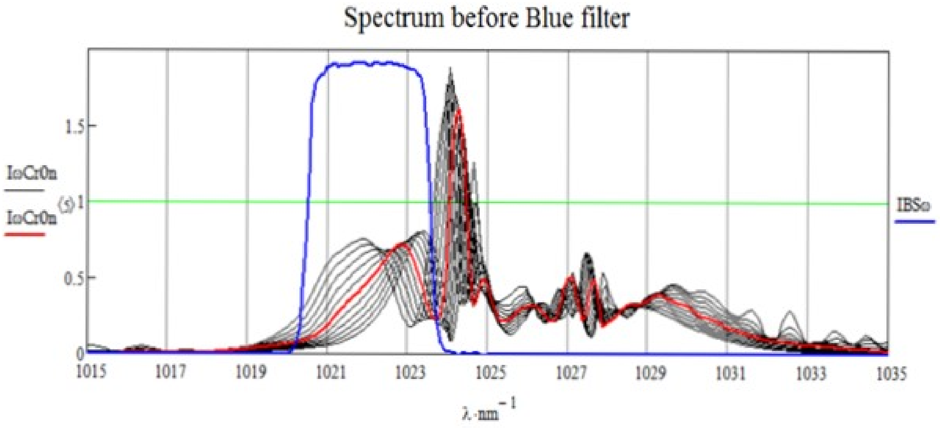
Spectrum before Blue filter

Figure 4-11 Optimization of red amplifier

4.8 Calculation of field intensity in time domain.

The fiber laser can generate ultrashort (femtosecond) pulses, however, there are no experimental techniques that allow the direct measurement of the time profile of femtosecond light pulses. Our theoretical model reproduces the experimentally measured spectral features with very high precision. Therefore, we have confidence that the theoretically calculated phase of the pulse is very close to the actual phase. Using the calculated spectrum and phase we can calculate the field in the time domain by a simple Fourier transform of the spectrum. The generated chirped pulses (not shown) had durations of several picoseconds, but by appropriate compensation of the phase distortion, transform limited performance can be effectively achieved and pulse durations less than 30 fs readily generated , see Figure 4.12.

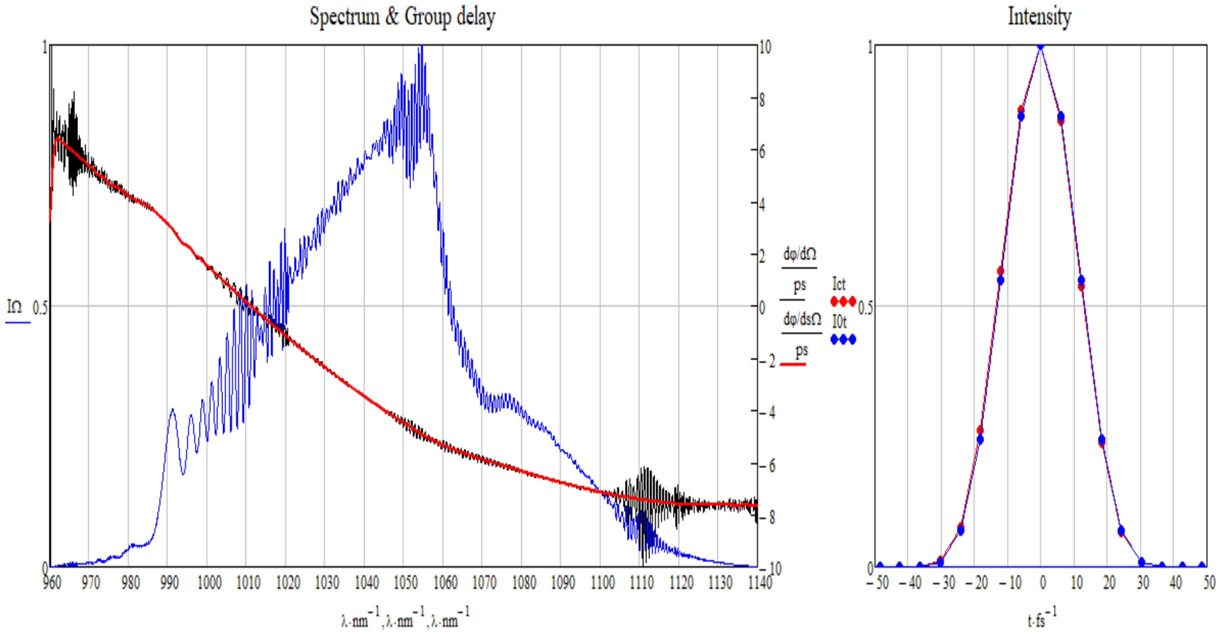

Figure 4-12 Calculation of spectra, intensity and autocorrelation of the optimized and compressed pulses. Left figure : blue – spectrum, black – group delay and red – smoothed GDD (using 2 nm resolution); Right figure: Displays the temporal profile of the pulse , red, compressed by removing smoothed GDD, blue using fully compensated phase (no phase distortion).

4.9 Starting of the laser.

The model has also been used to give insight into the startup process of pulse generation, which has also shown excellent agreement with experimental observation. In Figure 4.13, the left-hand illustration shows the time dependence of the energy of the output pulse during the period from turn on, while the right hand figure presents the inversion of the amplifiers. It can be seen that under CW pumping, it takes about 1 ms to develop the laser pulse and stabilize the dynamic equilibrium of the inversion of the amplifiers.

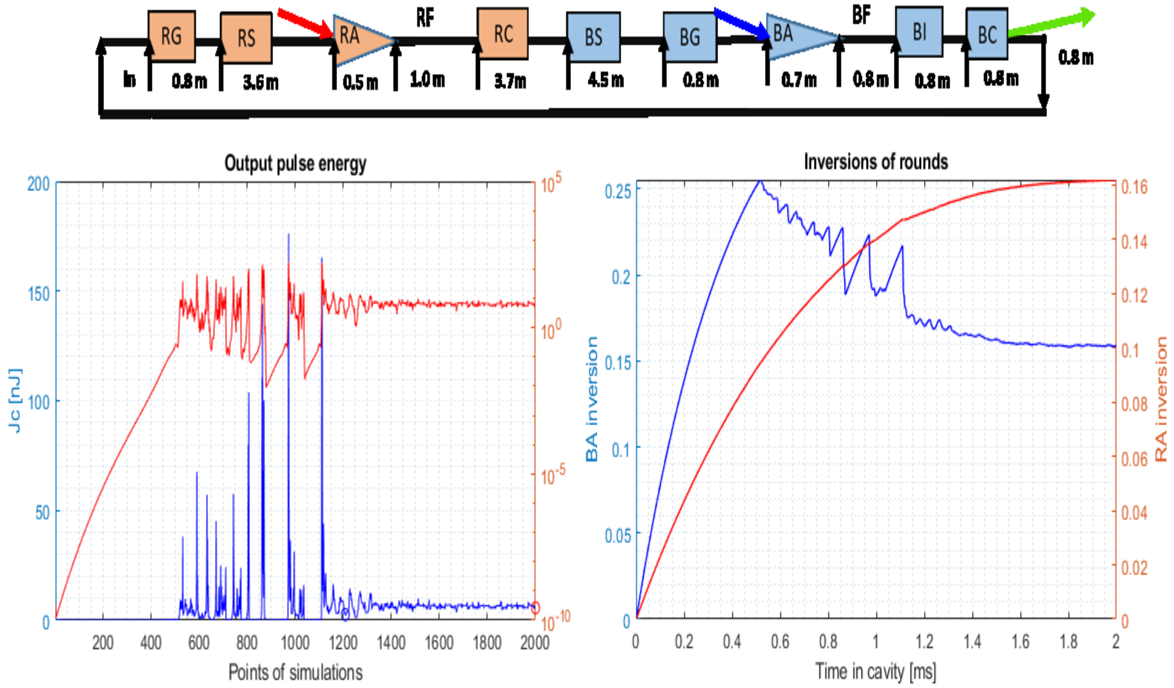

Figure 4-13 Calculation of the development of the laser pulse in the cavity. Left figure is the time dependence of output energy of the pulse, blue – linear,in nano-Joules, red similarly but presented on a log scale. On the right hand is shown the time dependence of the population inversion in first (RA, red) and second (BA, blue) amplifiers.

4.10 Stability of single and double pulsing.

The model has also been used to predict or prove some very interesting, important and experimentally observed effects, for example so called “double pulsing”, when instead of a single femtosecond pulse, the laser generates two weaker pulses with approximately the same total energy. In this case, it was found that in order to suppress such an effect that from the beginning of the generation process instead of a simple CW pumping scheme, pulsed pumping with a very specific time profile should be employed. The simulation shown in Figure 4.14 demonstrates that such modulation will negate double pulse generation, maintaining single pulse operation. The weaker pulses do not survive in between the pump while stronger (single) pulse successfully survive through the start-up pump pulses to steady state operation. In other words, a single pulse survives between pulses and recovers on the next pump pulse, while the double pulse disappears and on the next pump pulse everything starts from the beginning until we get a single pulse generation. It was found that pump pulses intensity gap, in pulses survival, exceeds 10% of pump current and it is well enough for reliable single pulse startup.

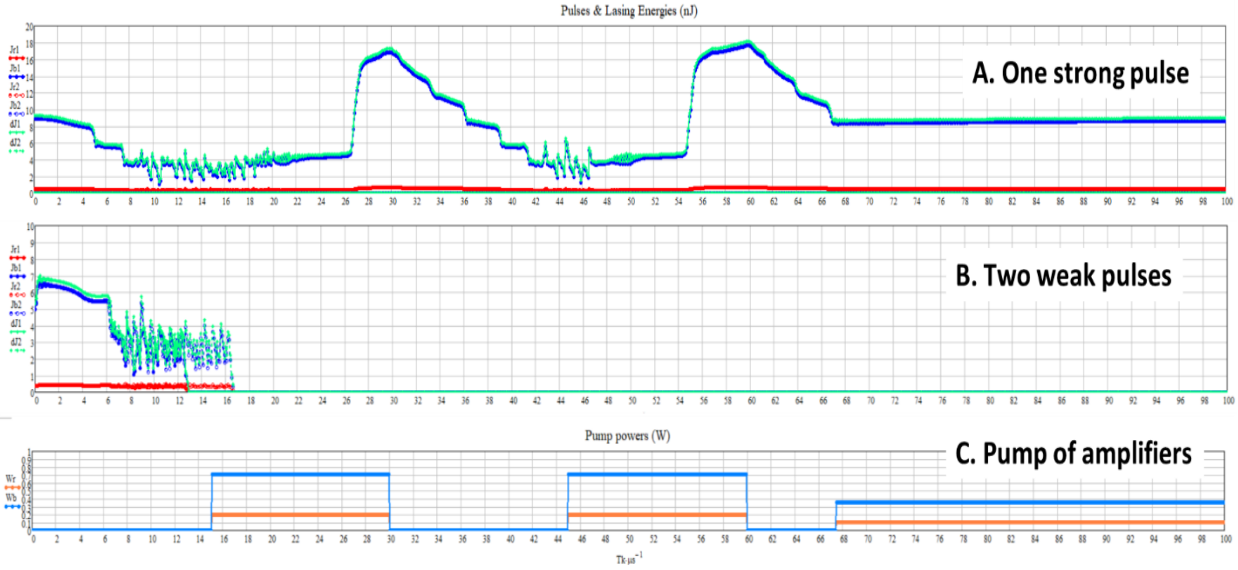

Figure 4-14 . Modeling of the suppression of double pulsing. Figures A and B. represent the energy of the pulses, after the red and blue amplifiers, lasing energy (green), solid one pulse, open – another pulse. C. pumping powers of the red and blue amplifiers.

Modeling of steady-state operation shows the difference in parameters of stable laser operation for single and double pulse modes. In Figure 4.15 you can see the ranges of operation and tuneability for single pulse (black) and double pulse (red) modes of operation. The minimum energy per pulse when generation is stable is more or less equal for both modes and is about 0.7 nJ for simulated configuration. When the laser operates in single pulse mode it can be tuned within the range of stability without any problems until generation take place.

In the case when the laser is started at 0.65 W pump power (see Figure 4.15) it will have operate in single pulse mode for certain, in this particular case. It can then be powered up to any chosen power within possible range of operation.

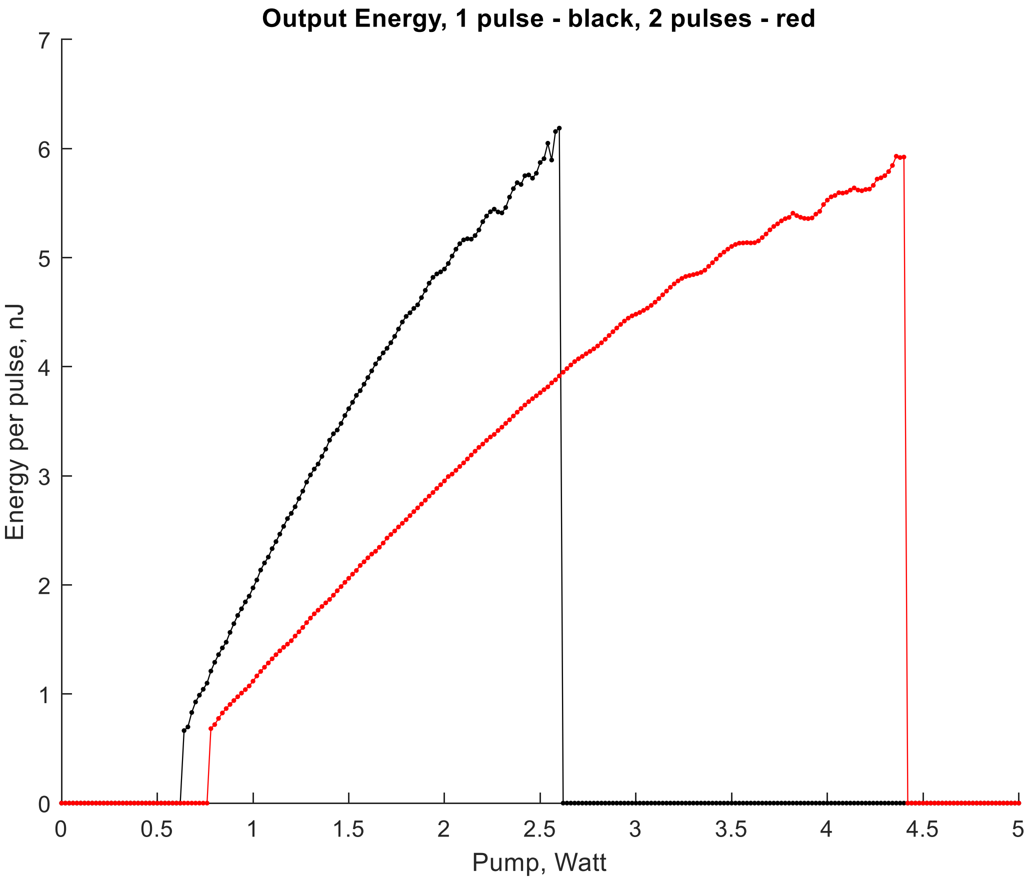

Figure 4-15 Modeling of pump ranges of operation and tuneability for single pulse (black) and double pulse (red) modes of operation.

4.11 “Shelves” of extra stability of laser generation.

The model was also used to investigate how the femtosecond oscillator behaved with different pumping powers of the amplifiers. For example, if the first (RA) amplifier is kept under constant pumping but slowly compared to one period in the cavity decrease the pumping of second (BA) amplifier, the generated output energy decreases. The dynamics of the generation of pulses has been simulated for different rates, from a sharp switch-off to a slow, linear in time pump decreasing over 100 ms as presented in Figure 4.16. It can be seen when the pump to the second amplifier is sharply switched off, the laser continues to generate pulses, but the energy decreases in a step-like manner. There exist some quite stable “shelves” where the pulses continue to be generated at a constant energy without any pumping taking place, but using the accumulated energy of the amplifier. When the pumping power is decreased very slowly (about 100 msec slope), the output energy follows the pump profile, but with some delay and there are unstable regions between stable “shelves” or plateaus. A similar picture was observed in the case of increasing of the pump. The output energy increased almost linearly with pumping, but going through stable shelved regions with unstable durations and with some hysteresis. The pump power can be slowly changed and the output power and pulse duration will follow it but at some values the output exhibits unstable spectra oscillating between two different realizations. However, the strength of the agreement between the theoretical model and the experimental realization has allowed the selection of pump power and cavity configuration to provide the most stable configuration.

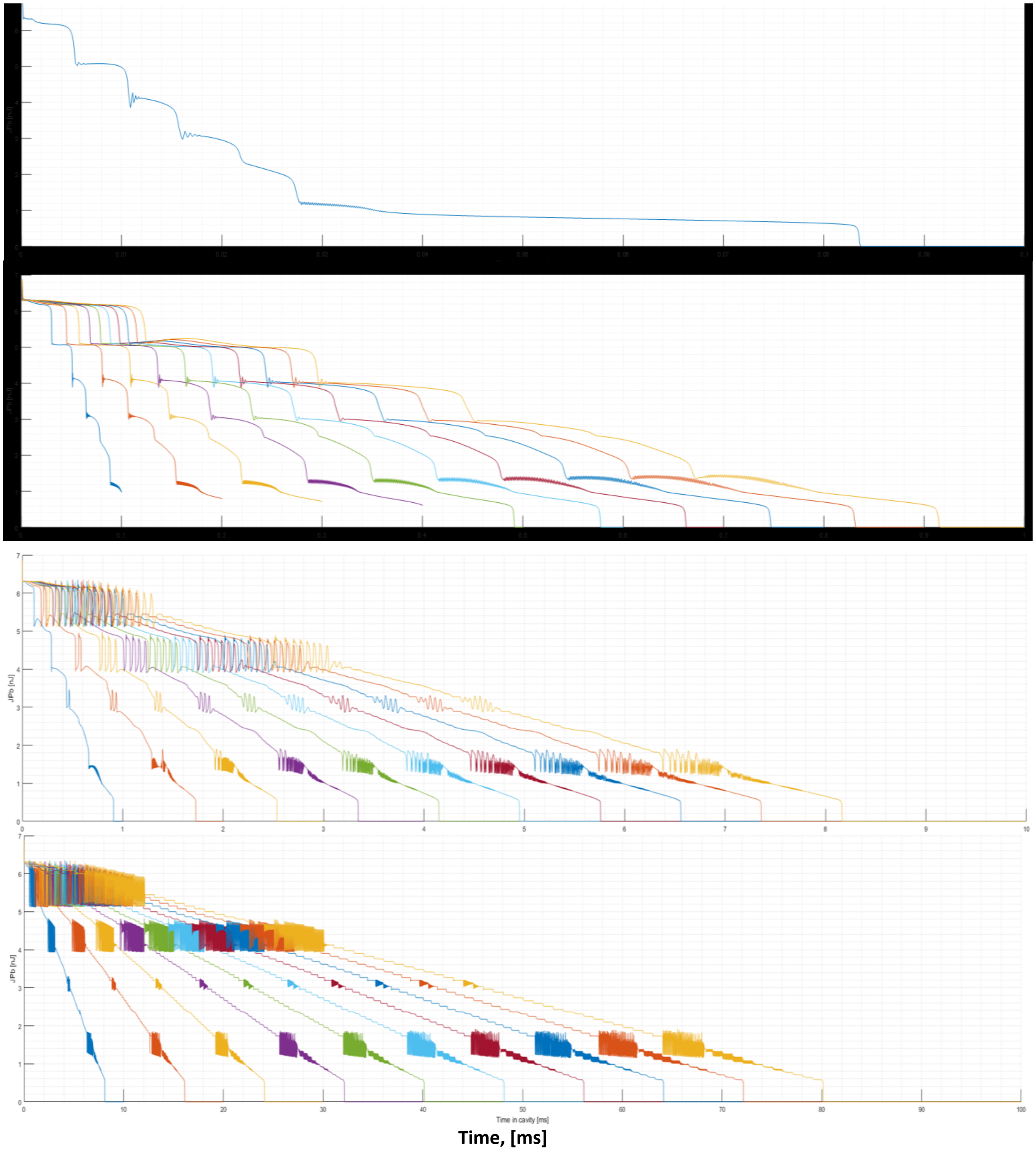

Figure 4-16 . Modeling of stable shelves and unstable intermediate regimes in laser operation. X – is time in cavity, Y – energy of output pulse. The modeling was carried out under different rates of switching-off the pumping of the second amplifier. In the top row the pumping was switched-off at zero time. In the lower panels the pumping power decreased linearly with time with different rates going from max to zero from 0.1 ms to 100 ms range. Stable operational regions or "shelves" can be seen with very unstable regions between them.

4.12 Validation of the model on existence of the “shelves”

Initial investigations were undertaken on the generation of the “shelves” or regions of power stability in a low power, experimental seed laser system. With the laser operating at maximum rate the BA amplifier was switched off and the output signal was observed in the real time on an oscilloscope. As demonstrated in Figure.4.17 up to 6 stable regions of operation were identified, which was comparable the analytical estimate. During of investigation of these shelves of stability it was found that they can be used for laser tuning and calibration.

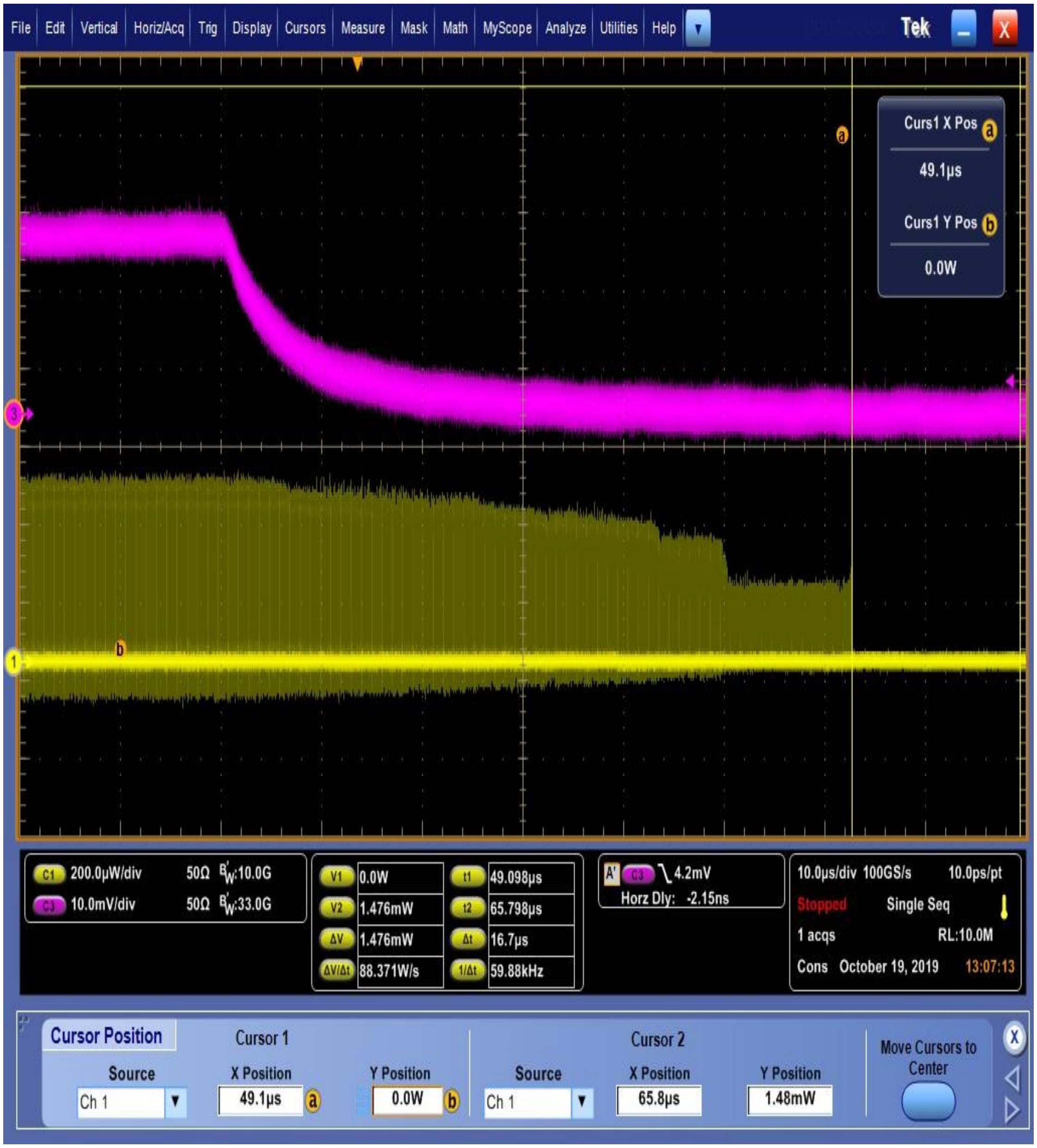

Curs1 X Pos 49.1µs
Curs1 Y Pos 0.0W

C1 200.0µW/div 50Ω B'W:10.0G
C3 10.0mV/div 50Ω B'W:33.0G

V1 0.0W
V2 1.476mW
ΔV 1.476mW
ΔV/Δt 88.371W/s
t1 49.098µs
t2 65.798µs
Δt 16.7µs
1/Δt 59.88kHz

A' C3 \ 4.2mV
Horz Dly: -2.15ns

10.0µs/div 100GS/s 10.0ps/pt
Stopped Single Seq
1 acqs RL:10.0M
Cons October 19, 2019 13:07:13

Cursor Position
Cursor 1: Source Ch 1; X Position 49.1µs; Y Position 0.0W
Cursor 2: Source Ch 1; X Position 65.8µs; Y Position 1.48mW

Figure 4-17 Demonstrating up to 6 stability “shelfs “ of laser generation.

If changing the pump of blue and red amplifiers in the middle of the second "shelf", one obtains the best stability of generation with wide spectral width at the pump condition of this particular shelf. In Figure. 4.18 and 4.19 you can see pulse stability and pulse spectrum at this point.

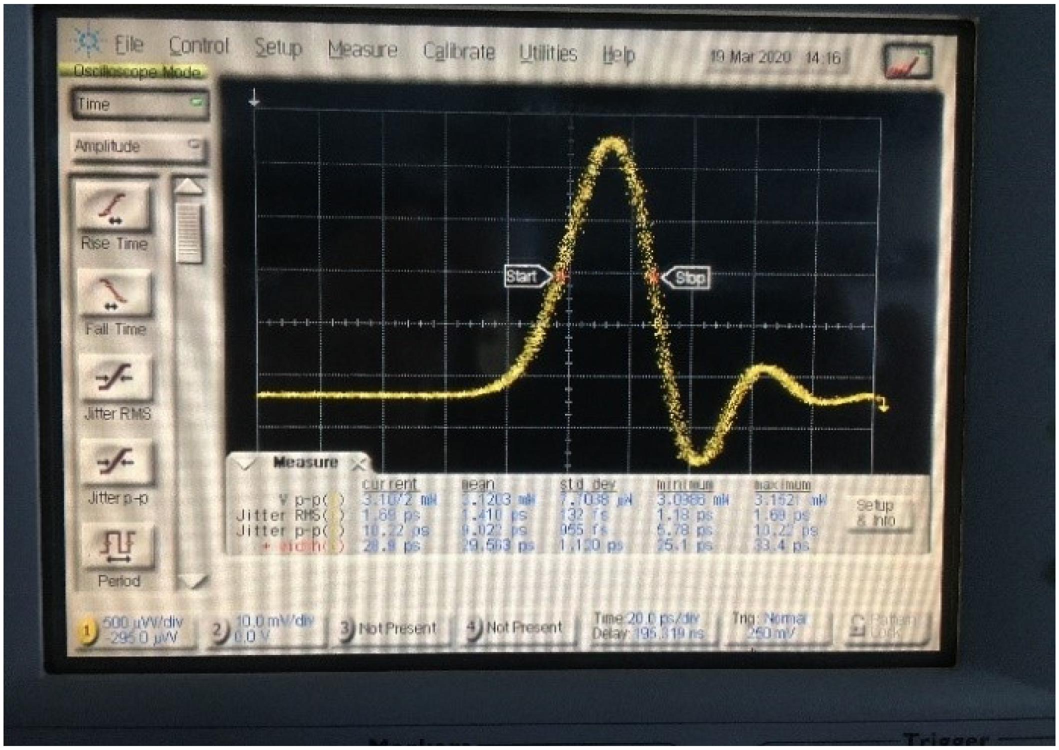

	current	mean	std dev	minimum	maximum
V p-p( )	3.1072 mW	3.1203 mW	7.7038 µW	3.0986 mW	3.1521 mW
Jitter RMS( )	1.69 ps	1.410 ps	132 fs	1.18 ps	1.69 ps
Jitter p-p( )	10.22 ps	9.022 ps	955 fs	5.78 ps	10.22 ps
+ width( )	28.8 ps	29.563 ps	1.130 ps	25.1 ps	33.4 ps

1 500 µW/div -295.0 µW
2 10.0 mV/div 0.0 V
3 Not Present
4 Not Present
Time: 20.0 ps/div Delay: 195.319 ns
Trig: Normal 250 mV

Figure 4-18 Pulse stability at TSS (c) P-k to P-k stability 1.6%, RMS stability 0.24%;

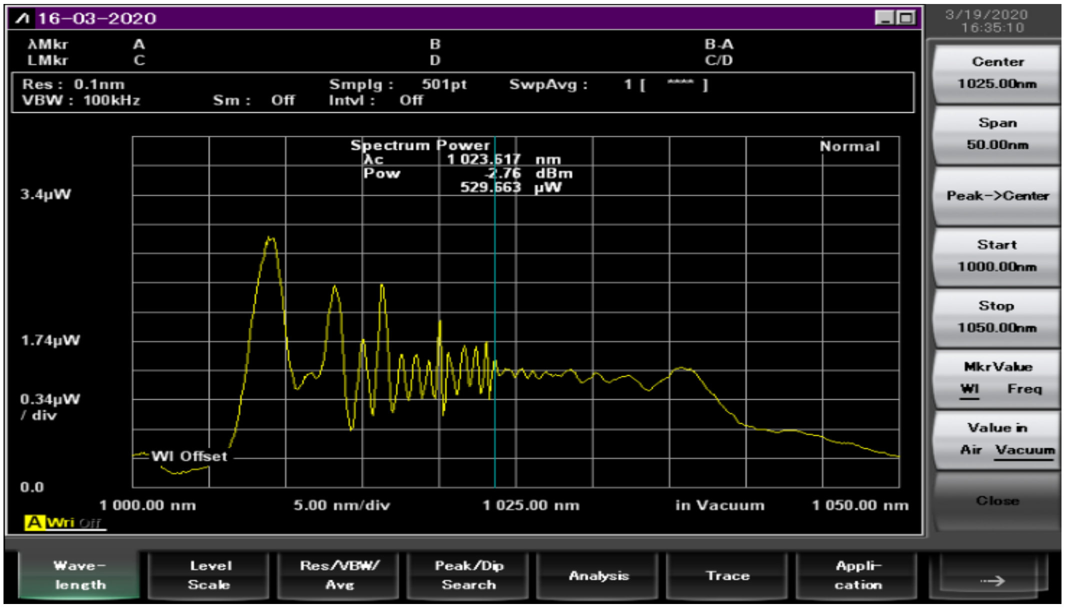

Res : 0.1nm
VBW : 100kHz
Sm : Off
Smplg : 501pt
Intvl : Off
SwpAvg : 1 [****]

Spectrum Power
λc 1 023.517 nm
Pow -2.76 dBm
529.563 µW
Normal

Center 1025.00nm
Span 50.00nm
Start 1000.00nm
Stop 1050.00nm
MkrValue Wl Freq
Value in Air Vacuum

Figure 4-19 Spectrum in the middle of the second shelf.

The experimental operational spectrum has also been directly compared to the theoretical prediction and exceptionally good agreement has been obtained, see figures 4.20 and 4.21. Some differences in the amplitude of the spectral peaks was observed but these can be explain by the averaging of the real laser spectrum.

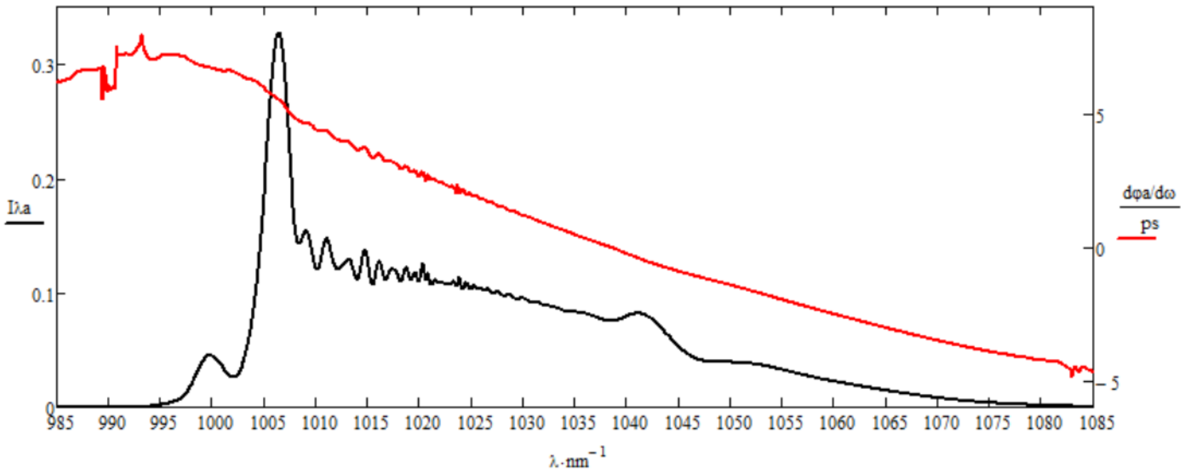

Figure 4-20 Calculated spectrum of the field at the output of the laser (black, in units of nJ/nm) and associated group delay (red, in units of ps).

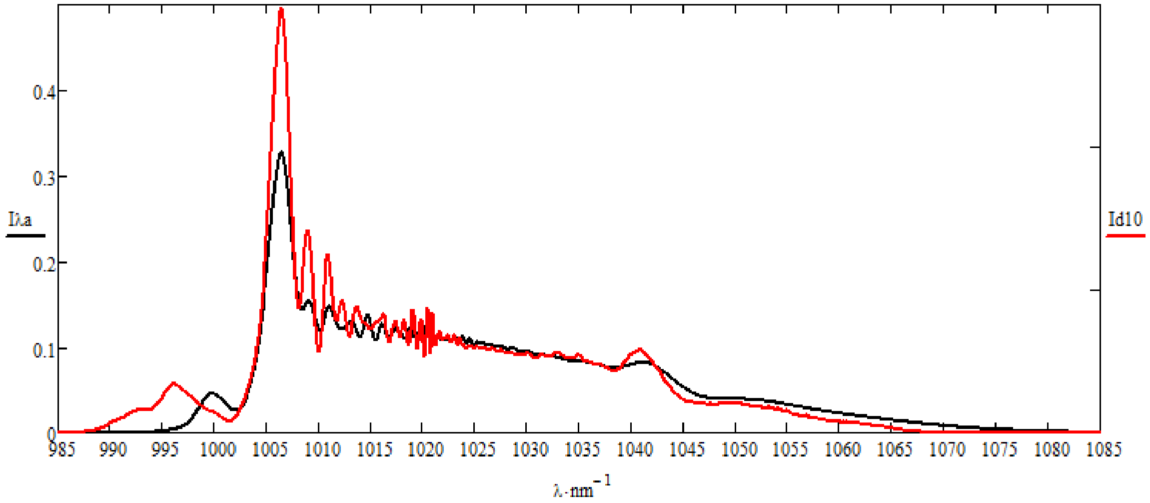

Figure 4-21 Comparison of calculated (black) and measured (red) spectra (nJ/nm).

5 Ultrashort femtosecond pulses setup.

5.1 Targets

Ultrafast lasers have entered everyday manufacturing processes in several applications over the past decade. These applications mostly require pulses that are not very short, usually between 0.5 and 1 ps (1 ps = 10^{-12} s) and with relatively high pulse energies, ranging between 20 and 60 µJ, as can be seen from the specification of the bestselling commercial laser systems. Ophthalmological surgery and material cutting or etching are the most common applications. This segment of the ultrafast laser market was historically established by the efforts of the leading laser manufacturers, like Coherent and Spectra-Physics. Currently, the market place has experienced continuous expansion in the number of potential suppliers.

Lasers that generate pulses of the order of tens of femtoseconds in duration (1 fs = 10^{-15} s) contribute to another segment of the market. These devices are also offered by a number of manufacturers, but they are used mainly for research and development, where the requirements for environmental stability are generally not as strict. Current commercially available systems generally require delicate handling, usually need to be in a controlled environment, particularly with respect to temperature and vibration and require relatively frequent maintenance. The output pulse energy for such lasers varies over a very broad range, upwards from several nanojoules. The available repetition rate is again usually fixed but commercially available varies widely from 1 kHz to 100 MHz. There are many industrial applications that do not require high pulse energy, given the peak power available with such short pulse durations, but commercially, there is a need for reliable lasers that are tolerant to the industrial environment and that are simple in handling to allow operation by users not skilled in laser technology, like biologists, chemists, or physicians. Laser-assisted processing of optically transparent solid materials, like glasses or sapphire, which includes bulk modification for 3-D structuring [CHE05] surface etching [SOH05] [WOR08] and direct bonding [HEL12] may require pulse energies as low as 200-300 nJ, combined with a few hundred or sub-hundred femtosecond pulse duration. Other processes that require pulse parameters of similar magnitude include laser induced forward transfer (LIFT) [BAN08] and frequency conversion using parametric or continuum generation [TZE09]. The process control for some applications may benefit from low pulse energies in combination with high repetition rates, in which case the effect takes place as a result of multi-pulse action which can be fine-tuned. Analytical applications require even lower pulse energy in combination with shorter pulse duration to ensure nondestructive interaction. These applications include multiphoton microscopy [DIA06] and spectroscopy [DRO11] that benefit not only from short pulse duration and high beam quality, but also from controllable spectral phase and temporal pulse profile for selective chromophore excitation when an ensemble of different chromophores is investigated. Laser-assisted crystallization or nucleation [ADA03][IKE15][SUG11][BLA00] finds application in the pharmaceutical industry and metallurgy as a method to enhance the extraction and an intermediate preparation step for further material analysis, where the target pulse parameter range is similar to multiphoton microscopy and spectroscopy. Two-photon polymerization [SER2003] for lithography and 3-D printing or micro-structuring [RIC04] use pulse energies from a single nanojoule to tens of nanojoules, given the pulse duration is less than 100 fs. Similar pulse parameters are in use for photoporation and transfection [STE06] which became widely used processes in today’s gene manipulation procedures performed on living cells. The number of applications where low-energy femtosecond pulses can be successfully used is quickly growing and many of them have become a routine part of manufacturing or analytical processes.

The common feature of all the aforementioned applications is the requirement for a “cold” process, where heat dissipation is suppressed or strongly mitigated and can be effectively controlled in both time and volume. This is achieved by using pulses shorter than 50 fs, which ensures minimal or no thermal effect caused by radiation on the region of interest. The realization of “cold” interaction regimes allows maximizing purely nonlinear processes without the destruction associated with the accumulation of excess energy inherent to longer pulses.

A goal of this research programme goal was to offer a reliable, femtosecond laser tool, capable of satisfying the requirements of the above mentioned applications and enhanced by the capability of programming the spectral phase and thereby manipulating and selecting the temporal pulse shape. Here we describe the architecture that that has led to its implementation by IPG Photonics in their YLPF-FlexO series of femtosecond oscillators and also demonstrate its pulse shaping capabilities.

The laser system is built upon two functionally distinct blocks - an all-fiber, self-starting master oscillator, coupled to a hybrid low-power Yb amplifier and a free-space pulse compressor that is used to correct for the large group delay dispersion that laser pulses acquire through nonlinear evolution in the oscillator/amplifier. It also provides a means to shape output pulses, as described below.

5.2 Master oscillator

A cross-filter ultrafast laser is used as an oscillator; see Figure 3.2. This is a new type of ultrafast laser source invented and patented [SAM18] by IPG Photonics in 2014. Briefly, this is a ring oscillator with an 11 MHz repetition rate, generating pulses with an energy around 10 nJ and a full spectral bandwidth of up to 90 nm (bottom-to-bottom), centered at 1030 nm. A typical laser spectrum is shown in Figure 5.1(a). As has been discussed previously, the output pulses of the cross-filter laser are positively chirped and stretched to ~10 ps. Figure 5.1(b) shows an experimental autocorrelation function (ACF), having 12 ps full-width at half-maximum (FWHM), with the triangular autocorrelation pulse shape representing the rectangular pulse of a strong linealy dispersed pulse. The pulses are fully coherent and allow for perfect phase control, thus making it possible to achieve full compression to the transform limit. Based on Fourier-transform calculations, the spectrum in Figure 5.1(a) supports pulses as short as 50 fs FWHM.

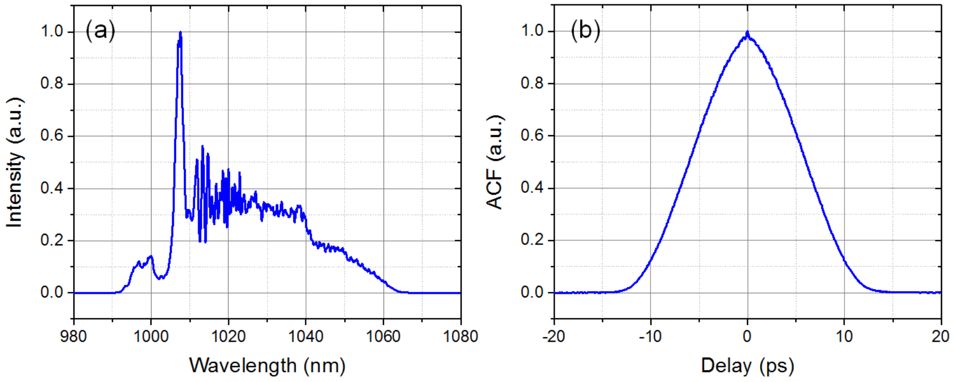

Figure 5-1 Typical output pulse characteristics for the cross-filter oscillator: (a) Experimental laser spectrum, measured with an AQ6374 optical spectrum analyzer (Yokogawa, Japan); (b) Experimental autocorrelation trace, showing 12ps ACF FWHM. The ACF profile is measured with PulseCheck autocorrelator (APE, Germany).

The internal field dynamics for cross-filter oscillators have been modeled using the nonlinear differential complex Ginsburg-Landau equation (CGLE), as described in textbooks [AGR12]. To solve the CGLE, a symmetrical split-step Fourier method (SSFM) was implemented in Mathcad (PTC, USA) on a standard personal computer. All necessary constants are taken from the literature and the components' specifications. The physical parameters of the laser system were experimentally measured, except for the population inversion profiles in Yb fiber amplifiers as has been previously discussed. The latter were optimized to get the best match with experimental spectra and autocorrelation functions, measured at several critical points around the laser resonator. An example of a simulated output spectrum and its group delay dispersion is presented in Figure 5.2(a). The corresponding time-domain intensity profile in Figure 5.2(b) illustrates a strongly chirped pulse, with features that are associated with those in the spectrum.

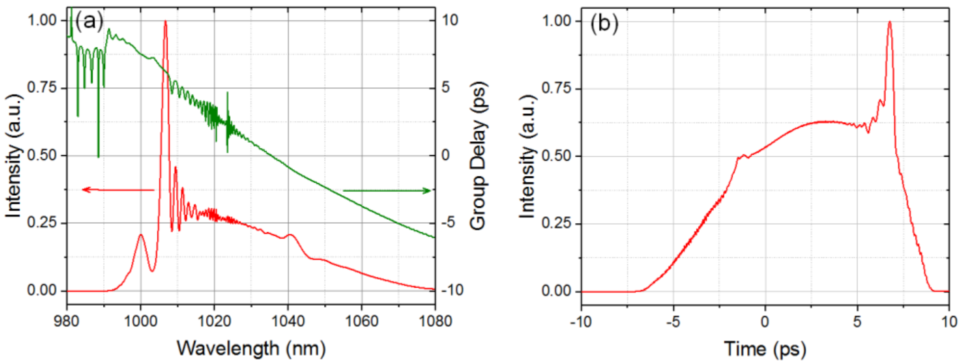

Figure 5-2 . Modelling of the cross-filter oscillator using CGLE: (a) Simulated output spectrum (red curve) and group delay (green curve); (b) Simulated time-domain profile of strongly chirped output pulses. The width of the simulated ACF profile (not shown) matches the width of the experimental ACF trace in Figure 5.1(b).

A low-power Yb amplifier-converter was employed to provide amplification with simultaneous spectral broadening at higher pulse energies under the conditions of the limited amplification bandwidth inherent to Yb amplifiers. This hybrid amplification-conversion mode allows not only obtaining up to 20 dB pulse energy amplification, but also broadening of the spectral bandwidth, compared to the oscillator. The amplifier- converter output remains fully coherent, allowing full manipulation of the phase similar to that achieved with the oscillator, but with pulse energies of up to 400 nJ.

5.3 Two-stage compressor

The oscillator/amplifier output was collimated in a linearly polarized 4.5mm-dia. (1/e2) beam and sent into a free-space pulse compressor, see Figure 5.3. The laser beam was first double-passed through a pair of transmission gratings, comprising the "static" stage, and then, it was guided through a folded-4f pulse shaper [DAN17] with a programmable spatial light modulator (SLM) at the Fourier plane (1D-LCOS SLM, Hamamatsu). The throughput of the entire two-stage compressor setup is almost 50%. The output laser spectrum was slightly narrower than the original but was capable of supporting 53 fs pulses.

A grating compressor was used to correct for the second-order dispersion (SOD) at the oscillator/amplifier output, which was estimated to be about 1.3×10^5

fs^2 at 1030nm. For 1000g/mm gratings, a grating separation of only 21 mm allowed offsetting this amount of SOD. This setup, however, does not address the nonlinear chirp, present in the oscillator/amplifier output pulses, and adds about 0.73×10^6 fs^3 of third-order dispersion (TOD).

The folded-4f shaper, commonly used for femtosecond pulse shaping [40], enabled further refinement of the laser pulse profile. The 4f setup dispersed the laser spectrum across the linear phase modulator and enabled direct manipulation of the spectral phase, regardless of the laser repetition rate. Multiphoton intra-pulse interference phase scan (MIIPS) [XU06],[COE08] was used to measure the residual spectral phase and correct for the third order and higher-order dispersion. This adaptive compression stage also offered the capability to reshape the laser pulses by modifying the phase mask applied to the SLM. The shaper's "time window" was about 3 ps.

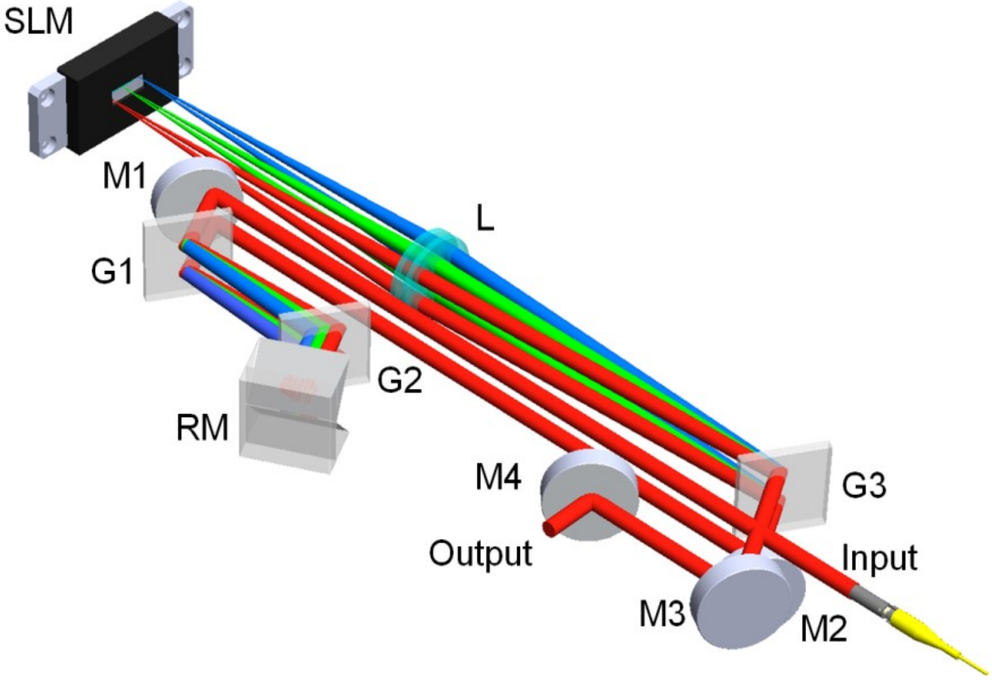

Figure 5-3 Two-stage pulse compressor, comprising a grating pair and a folded-4f shaper with an adaptive element at the Fourier plane: M1-4, guiding mirrors; G1-3 – transmission gratings; RM – roof mirror; L – lens assembly; SLM – spatial light modulator.

5.4 Pulse Compression and Shaping

The fidelity of the two-stage pulse compression was validated via autocorrelation measurements (PulseCheck, APE, Germany). Non-collinear ACF traces were recorded after pulse optimization using only the grating pair, as shown in Figure 5.4(a), and also using both static and adaptive stages, see Figure 5.4(b).

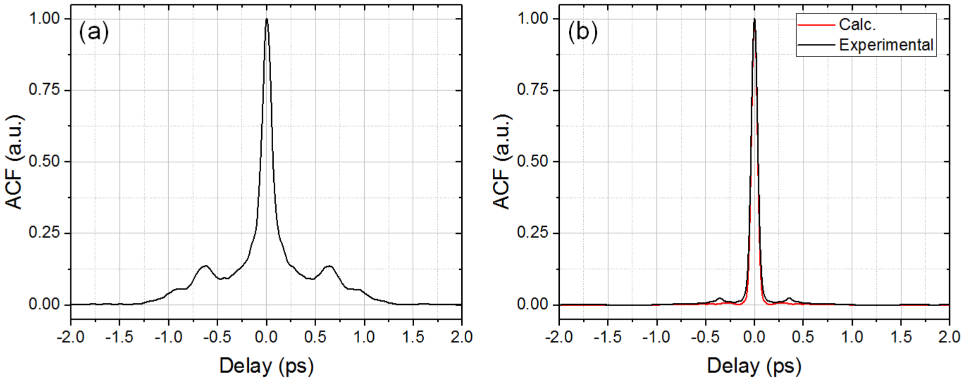

Figure 5-4 Verification of pulse compression using the two-stage compressor: (a) ACF trace for the optimized grating-pair compressor, without the 4f shaper; (b) ACF trace for compressed pulses at the system output. The theoretical limit (red curve) is calculated for the experimental output spectrum and a constant spectral phase.

As anticipated, the grating compressor alone gave laser pulses with ~100 fs FWHM duration (ACF FWHM of 130fs) and an extensive modulated tail due to the residual TOD. The MIIPS-enabled dispersion correction using the 4f shaper, following the static compressor, gave a 76.9 fs ACF FWHM, which is only 7% longer than what one would expect for TL pulses, calculated from the experimental output spectrum. The corresponding FWHM pulse duration was measured to be 56.9 fs. It was calculated from the ACF FWHM using a ×0.74 factor that is deemed appropriate for the given shape of the laser spectrum. Note that a sech^2 approximation gives an over-optimistic estimate of 49.6 fs FWHM (×0.645 factor), which is lower than the Fourier-transform limit of 53 fs. A Gaussian fit would suggest a 54.5 fs FWHM (×0.709 factor).

Once the pulse dispersion is accounted for (and compensated if necessary), it is relatively straightforward to use the shaper in order to alter the spectral phase and thereby, generate other optical waveforms. The simplest example is to add a linear chirp (applying a parabolic spectral phase mask) in order to adjust the pulse duration or even the arrival time for the red- and blue-parts of the spectrum to, e.g., control excitation [NAI16] [WIP13]. Figure 5.5(c) illustrates the measured ACF profiles for several applied chirp values, targeting 100 fs, 200 fs and 400 fs FWHM pulse durations, estimated from the ACF width using a sech^2 fit. The corresponding SOD values, used to generate the phase masks for the shaper, are 1900 fs^2, 3700 fs^2, and 7000 fs^2 at 1025 nm, respectively. For the latter, Figure 5.5(a) shows the corresponding parabolic phase profile, added to the dispersion compensation mask. The expected time-domain intensity profile of the pulse is shown in Figure 5.5(b). Note that either positive or negative chirp can be applied, and the SOD magnitude can be as high as 15000 fs^2.

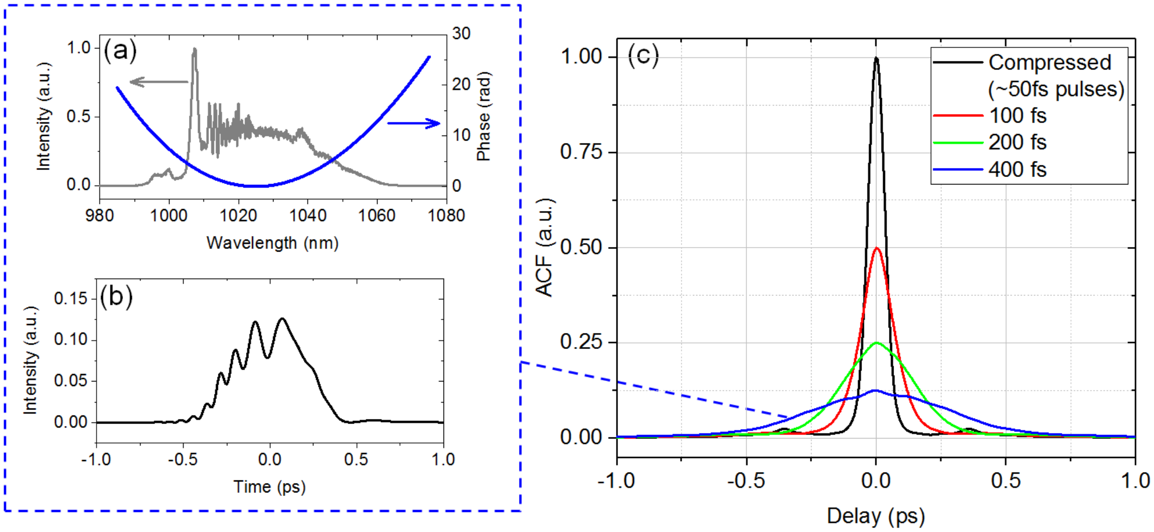

Figure 5-5 Tuning the generated pulse duration using a programmable linear chirp: (a) A Parabolic phase mask corresponding to 7000 fs^2 SOD at 1025nm, applied by the 4f shaper. The laser spectrum is shown as a reference; (b) Calculated intensity profile for 7000 fs^2 SOD at 1025nm; (c) Experimental ACF profiles for the compressed pulse (reference) and for 1900 fs^2, 3700 fs^2, and 7000 fs^2 SOD at 1025 nm. The corresponding target sech^2 pulse durations are 100 fs, 200 fs, and 400 fs, respectively.

Another common technique is the use of sinusoidal phase modulation for the reshaping of a single pulse into a burst of sub-pulses [PES14]. The number of sub-pulses and their relative magnitude strongly depend on the phase modulation amplitude. Their time period (spacing) is equal to the spectral phase modulation "frequency" (measured in [ps]), which can be continuously tuned. For the pulse burst in Figure 5.6, the modulation amplitude was set to 0.45π, which leads to a pulse sequence with three main sub-pulses of similar magnitude. The calculated phase mask in Figure 5.6(a) and expected time-domain intensity profile in Figure 5.6(b) are given for 0.2 ps spacing between pulses. The latter can be adjusted continuously, with high precision, by simply tuning the modulation frequency of the sinusoidal phase mask. Experimental ACF traces for 0.2 ps, 0.4 ps, and 0.8 ps spacing between pulses are illustrated in Figure 5.6(c). They match the simulated ACF profiles for the corresponding parameters.

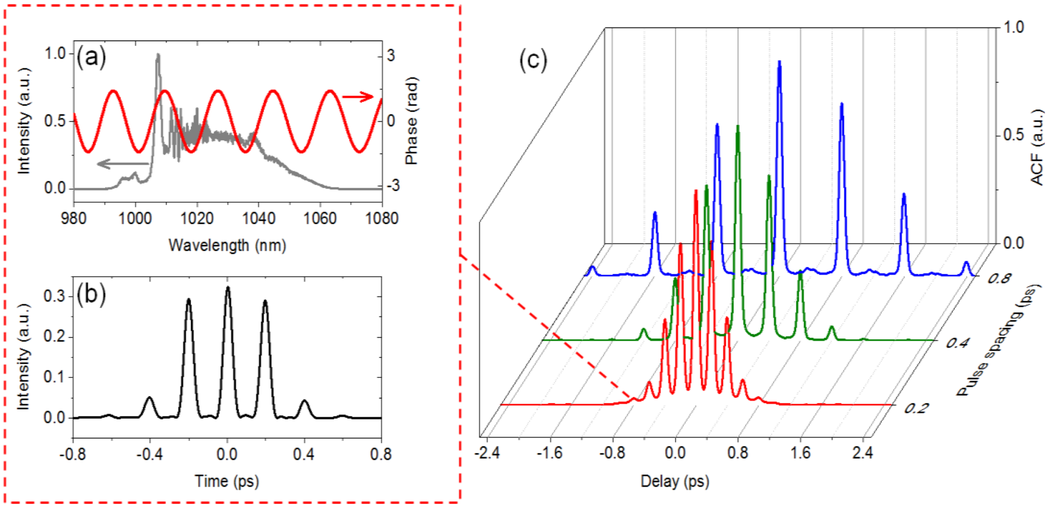

Figure 5-6 Generation of pulse bursts using sinusoidal phase modulation: (a) Sinusoidal phase with amplitude 0.45π and 0.2 ps modulation "frequency" (in the spectral domain). The input laser spectrum is shown as a reference; (b) Calculated intensity profile for the sinusoidal mask described in Fig. 5.6(a); (c) Experimental ACF profiles for 0.2 ps, 0.4 ps, and 0.8 ps spacing between pulses in the burst.

Phase shaping is an attractive, relatively lossless way to bring selectivity into nonlinear optical processes. It can be illustrated in the second harmonic generation (SHG) process, see Figure 5.7. When ultrashort laser pulses are compressed to their transform limit and focused on to a thin nonlinear crystal, the dominant contribution to the bell-shaped SHG spectrum comes from sum-frequency generation (SFG) across the laser spectral bandwidth. Laser photons at frequencies ω+Δ and ω-Δ, where Δ is an arbitrary detuning, add up to produce

SHG photons at 2ω and interfere constructively with other contributions because their nonlinear phase $\varphi(\omega+\Delta)+\varphi(\omega-\Delta)$ is independent of detuning Δ; here, $\varphi(\omega)$ is the spectral phase of the laser pulse. Then, if a phase mask with a proper symmetry is applied, such as, e.g., $\varphi(\omega) \propto (\omega-\omega_0)^3$, constructive interference is preserved only for ω_0, corresponding to frequency $2\omega_0$ in the SHG spectrum.

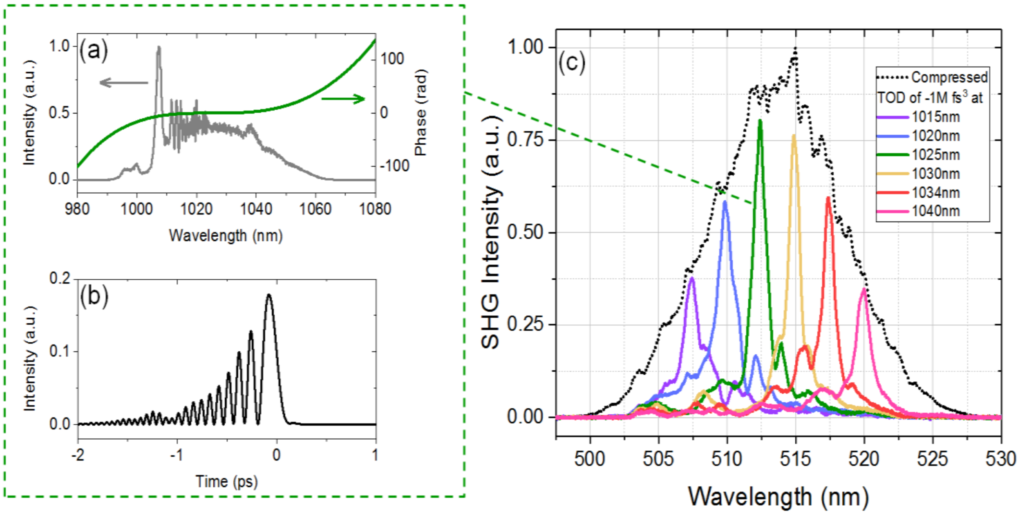

Figure 5-7 Selective two-photon excitation using programmable cubic phase: a) Cubic phase mask corresponding to -106 fs^3 TOD at 1025nm, applied by the 4f shaper. The laser spectrum is shown as a reference; (b) Calculated intensity profile for -106 fs^3 TOD at 1025nm; (c) Experimental SHG spectra for the cubic phase mask scanned across the laser spectrum from 1015 nm to 1040 nm, in 5 nm increments. The SHG spectrum of the compressed pulses is given as a reference. The spectra were acquired with AQ6374 optical spectrum analyzer (Yokogawa, Japan), configured for 0.1nm resolution.

The latter can be understood by recalling that TOD corresponds to a parabolic group delay (in the frequency domain). Spectral bands at frequencies symmetric relative to ω_0, i.e., at $\omega_0+\Delta$ and $\omega_0-\Delta$, are equally delayed and therefore, continue contributing to the signal at $2\omega_0$through the SFG process. For other SHG frequencies though, the timing between paired spectral bands drifts, suppressing their contribution to the nonlinear signal.

Experimentally, one observes a narrowed SHG spike when a cubic phase is applied. If there are no other phase distortions, the SHG peak closely tracks the point of symmetry for the cubic phase. That is if the phase mask is centered at 1025 nm, as in Figure 5.7(a), the SHG peak is expected to be at 512.5nm. By changing the center frequency/wavelength of the cubic phase mask, one effectively tunes the two-photon excitation band. Note that the strength of the two-photon peak when TOD is applied is similar to what one gets using compressed pulses; i.e., the entire spectral bandwidth of the shaped pulse contributes towards the two-photon transition at $2\omega_0$.

5.5 Booster-converter.

The dual filter seed source has an acceptable spectral width for ultrashort pulse generation but is quite limited in its output power, which is effectively defined by the stability window of generation and start-up limitations as previously discussed. Greater flexibility in the achievable output power and spectral output of the system can be rachieved by using an additional booster amplifier with a fiber-optic nonlinear converter, see Fig 5.8.

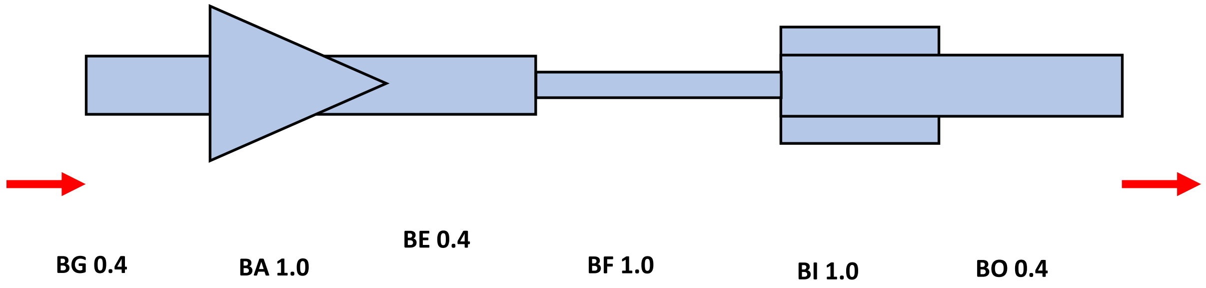

Figure 5-8 . Booster-amplifier with nonlinear converter. BA – ytterbium amplifier 1m, BF –relatively small mode field diameter fiber 1m (operating as a nonlinear converter), BG, BE, BI, BO – feeding, isolator and output LMA fibers.

This configuration of booster is very flexible and makes it easy to control the output parameters because the major nonlinear conversion takes place in BF (the control fiber). As a result, we can manipulate the output power and the spectrum by changing the type (mode field) and length of the fiber BF only.

Figures 5.9-5.11 show the simulation results for two configurations with 6 μm and 12 μm mode field diameter control fibers.

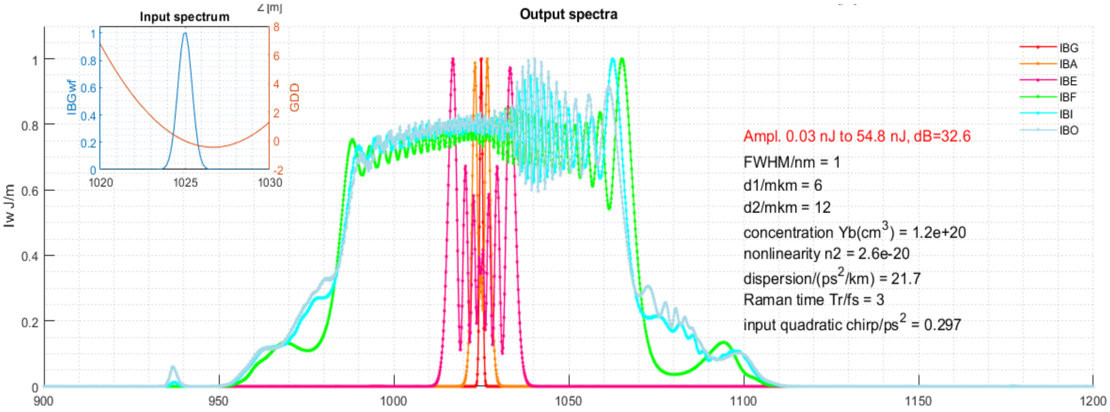

Figure 5-9 Input spectral FWHM 1 nm, “control fiber” diameter 6 μm, 55 nJ

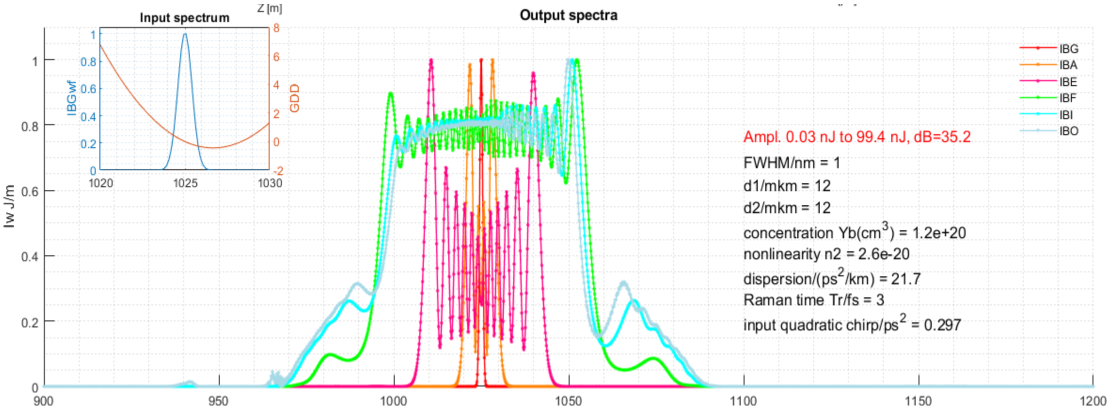

Figure 5-10 Input spectral FWHM 1 nm, “control fiber” diameter 12 μm, 100 nJ

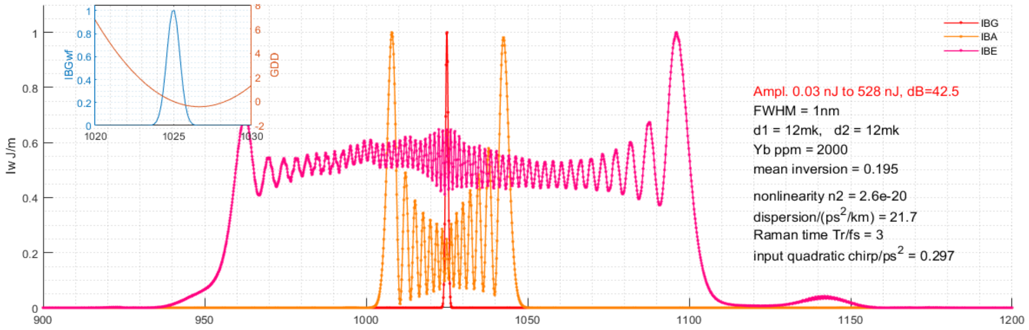

Figure 5-11 . Input spectral FWHM 1 nm, “control fiber” diameter 12 μm, 528 nJ

Thus, using the LMA booster-amplifier and the larger mode diameter control fiber a high energy (about 1 μJ) pulse and very broadband spectrum of the order of 50 nm and above can be controllably produced, with the capability to compress the pulse to 50 fs or less in a practically transform limited format.

5.6 Booster – converter test results.

Based on the above calculation we have assembled a prototype laser source with advanced characteristics (control fiber 1m MFD 6 μm).

750 mW output power, 70 nJ. Pulse FWHM (sech2) = 37fs

Fidelity is 0.8-0.9, which is good.

Satellites are present at ~2.35ps delay due to amplitude modulation.

Fig. 5.12-5.15 illustrate the performance of the system.

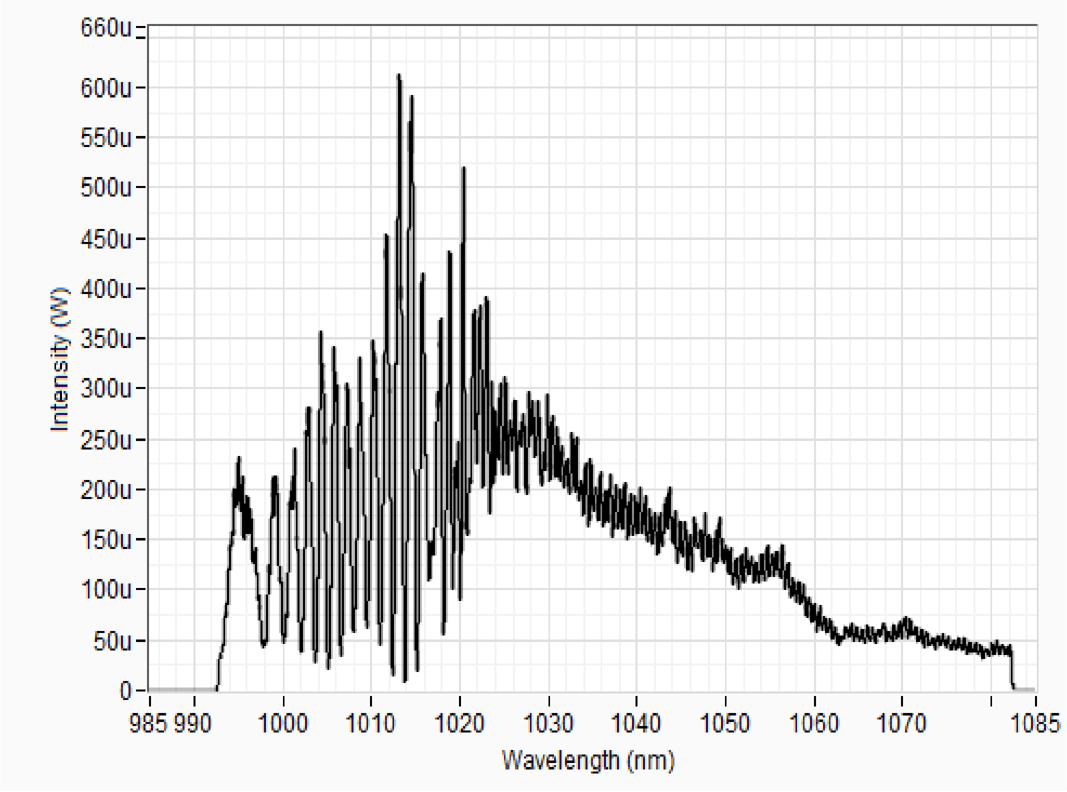

Figure 5-12 Output spectrum 750 mW output power, 70 nJ.

Figure 5-13 Pulse ACF.

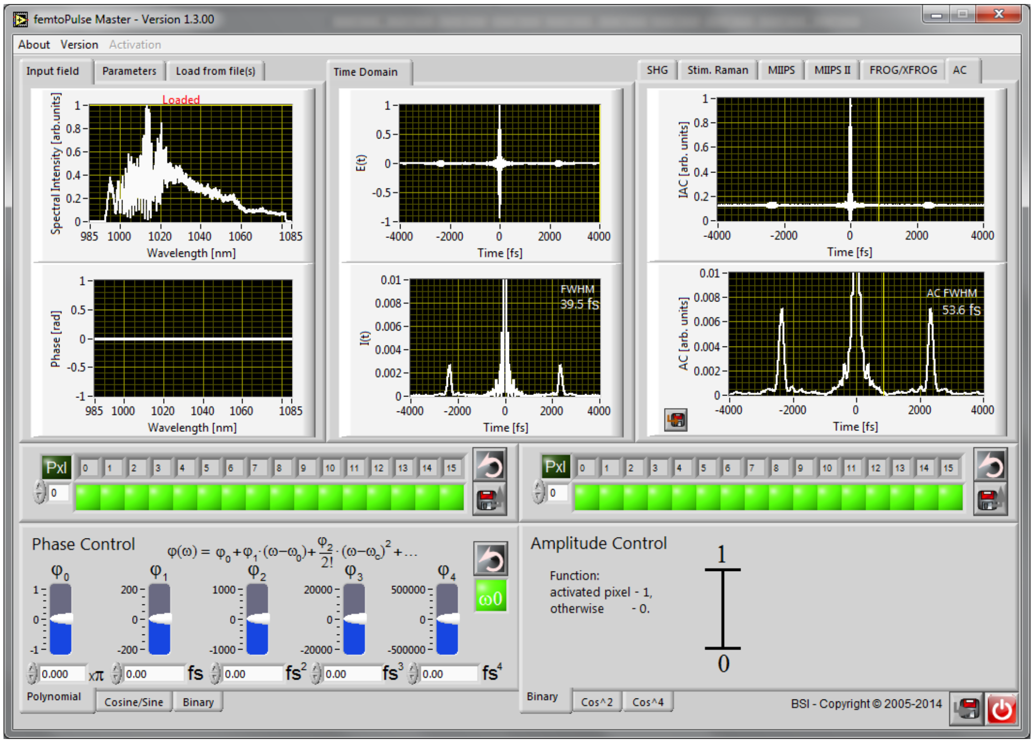

0.000 xπ

0.00 fs

0.00 fs^2

0.00 fs^3

0.00 fs^4

Function:
activated pixel - 1,
otherwise - 0.

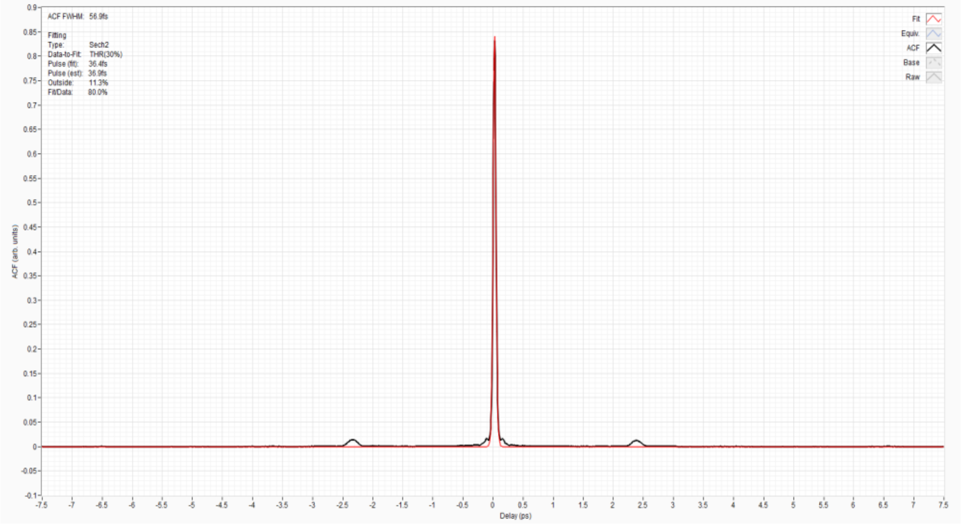
ACF FWHM: 56.9fs

Fitting
Type: Sech2
Data-to-Fit: THR(30%)
Pulse (fit): 36.4fs
Pulse (est): 36.9fs
Outside: 11.3%
Fit/Data: 80.0%

Figure 5-14 . A screenshot of femto Pulse Master simulation software, showing the calculated time-domain characteristics of a pulse defined by the laser spectrum (top-left) and a flat spectral phase (bottom-left); time-domain electric field profile (top-middle); intensity profile, normalized to unity at the peak and zoomed down to 1% level (bottom-middle); interferometric autocorrelation (top-right) and background-free autocorrelation, normalized to unity at the peak and zoomed down to 1% level to highlight the pedestal (bottom right).

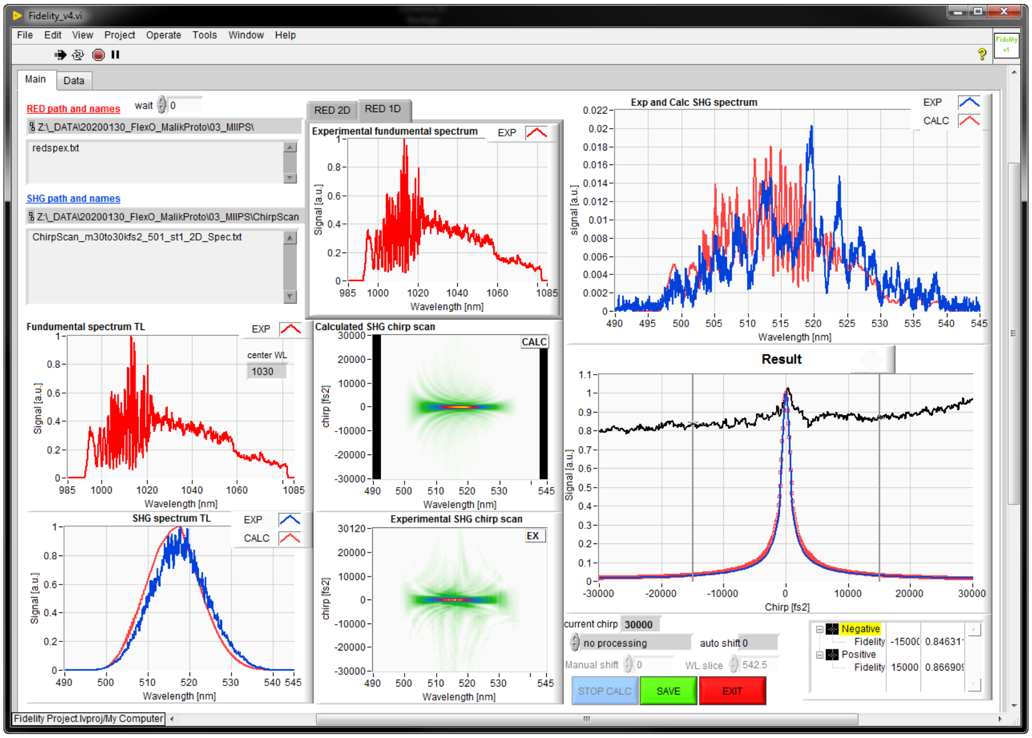

RED path and names   wait 0

Z:_DATA\20200130_FlexO_MalikProto\03_MIIPS\

redspex.txt

SHG path and names

Z:_DATA\20200130_FlexO_MalikProto\03_MIIPS\ChirpScan

ChirpScan_m30to30kfs2_501_st1_2D_Spec.txt

center WL 1030

current chirp 30000

no processing   auto shift 0

Manual shift 0   WL slice 542.5

Negative
Fidelity -1500(0.84631

Positive
Fidelity 15000 0.86690(

Figure 5-15 . Fidelity calculations based on the chirp scan: (top-left) the loaded laser spectrum; (bottom-left) calculated and experimental SHG spectra for the compressed pulses; (top-middle) laser spectrum, refitted on the calculation grid; (bottom-middle) calculated and experimental SHG traces as a function of linear chirp, scanned within +/-30,000fs^2; (top-right) instantaneous SHG spectra plotted by the program for every chirp value as the spectrograms are generated; (bottom-right) Spectrally-integrated SHG signal as a function of the applied chirp, calculated and experimental; the ratio between the theoretical (blue) and experimental (red) curves gives "fidelity" curve (black).

For the calculations in Figure 5.14, the laser spectrum was acquired after the pulse shaper that was used to compress the laser output. The spectrum was confined by the passband of the pulse shaper, which cuts the spectral wings on both sides and limits the calculated transform-limited (TL) pulse duration to ~40fs FWHM. The expected autocorrelation (AC) width for this spectral shape is 54fs FWHM. There are significant side-pulses at ~2.8ps delay due to the high-frequency amplitude modulation that can be seen across the laser spectrum. The modulation next to the main peak is imposed by the sharp cutoff on the spectral wings. When the pulse is fully compressed, sub-pulse distribution is symmetric relative to the main peak, as to be expected.

In the presence of instabilities, the compensation mask, determined via the MIIPS technique or some other method, accounts only for ensemble-averaged distortions. Each individual pulse can no longer be perceived as TL and pulse-to-pulse variations would lead to deviations from the expected profile. Obviously, it also affects how such ensemble responses to deliberately added phase distortions.

The degree of pulse reproducibility, or pulse-train fidelity, is estimated by comparing two traces – experimental linear chirp scan while monitoring SHG spectra and a calculation for the given spectrum under assumption that the pulse train has no instabilities and is fully coherent. The SHG spectrograms are integrated over the wavelength axis to show the total SHG signal as a function of applied chirp, in addition to the compensation mask that corrects for ensemble-averaged distortion. The two curves are normalized to unity at the peak, where no chirp is applied.

One can see that the experimentally measured curve (Figure 5.15, bottom-right; red curve) is wider than the calculated one (Figure 5.15, bottom-right; blue curve) for the given laser spectrum; i.e., the rate of pulse stretching is not as fast as one would expect. This is interpreted as due to the instability that effectively broadens the pulses and thereby, makes them less sensitive to the added chirp.

To have a metric to quantify the degree of instability, the normalized theoretical curve is divided by the normalized experimental curve (see Figure 5.15, bottom-right; black curve). Its asymptotic value in the limit of large chirp, plus or minus, is taken as the fidelity parameter. Its value is close to 1 for a stable pulse train, and approaches 0 for an incoherent source. For the example in Figure 5.15, the retrieved value is about 0.3, which is indicative of significant noise on the pulse train.

When the blue edge of the output spectrum is removed by an amplitude mask (on the pulse shaper), the temporal satellites disappear at the expense of reduced power and a longer pulse duration, see Figures 5.16 and 5.17.

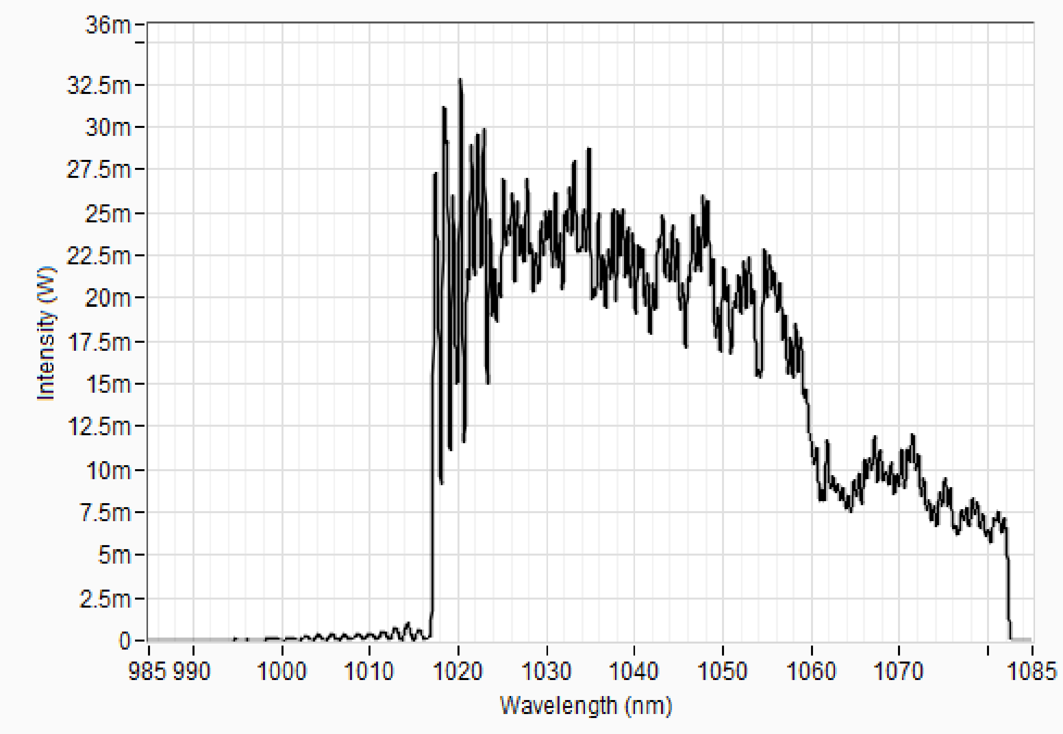

Figure 5-16 Filtered spectrum

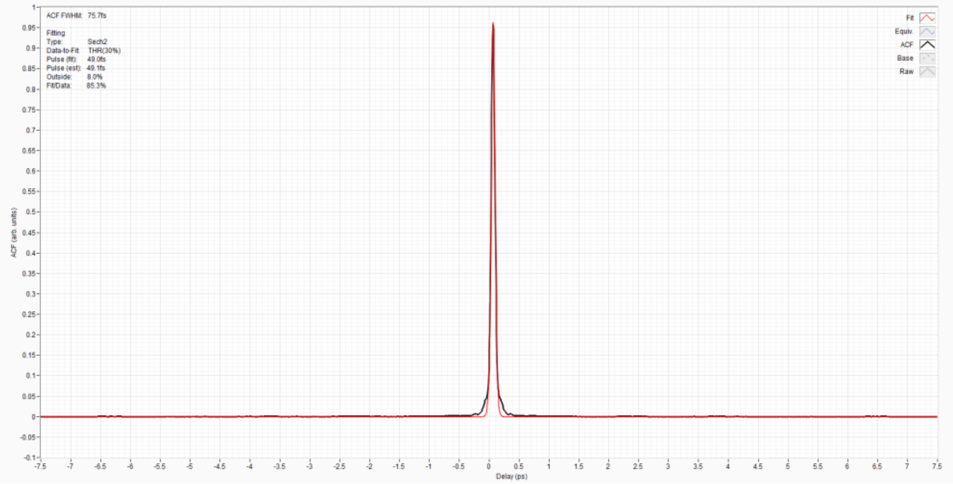

Figure 5-17 Improved pulse ACF

We found a very good correlation of our numerical simulation with the experimental results. This gives the possibility to design, on demand, of different types of femtosecond laser sources which will be of immediate commercial importance.

6 Conclusions.

The key outcomes of this research have been:

1. **I have developed a new method of passive mode-locked pulse generation based on the cross-filters technique and nonlinear conversion in a passive fiber. The results of this research have been patented [SAM16]**
2. **The laser configuration provides the capability of self-starting operation and an appropriate technique was developed to enable this.**
3. **An analytical computer model of the laser was developed which shows excellent correlation with experimental results. It provides a powerful tool for further improvement of the laser parameters and allows the customized design of new laser configurations according potential customers' specification.**
4. **The laser was tested in different applications: as the seed source for high power pico-femtosecond laser by spectrally selecting the generated spectrum (considering the flatness and linearity of the chirp, typically 15-20 nm). The results show that the laser is capable of providing configurations with an output energy greater than 100 μJ and pulse durations 200-700 fs.**
5. **The laser was investigated for the generation of ultrashort pulses utilizing the full operational spectral band, and was capable of delivering up to 15 nJ with 50 fs pulses.**
6. **The technique of pulse amplification and conversion by using an external amplifier was also investigated. A corresponding computer model of operation of such configuration was also developed. The overall system was capable of delivering pulse output energies of greater than 100 nJ in pulses of less than 50 fs and an output power of 1000 mW.**
7. **This research program has resulted in the generation of numerous commercial and technical know-hows which have**

simplified the development and mass manufacture of pico-femtosecond fiber lasers.

8. **The results of this project are currently being used by IPG for the development and manufacture of a new line of laser products.**

In the course of this project, results were obtained that were not included in this thesis however, they are important and very promising for practical applications.

Namely:

Theoretically and experimentally, the possibility of a controlable shift of the center of the lasing wavelength was demonstrated (up to 45 nm) by changing the fiber length of the amplifier and the gain profile along the fiber length (control of the pump wavelength).

When using long amplifiers, the laser goes into the similariton mode. This mode is characterized in that the nonlinear broadening and gain in the amplifier occur simultaneously. As a result, a wider and smoother spectrum is obtained without loss of coherence. This is important for producing pulses shorter than 30 fs.

The conditions were found under which the laser is capable of generating multiple frequencies. In our case, this was 11xn MHz (n=1 to 11). All possible frequencies were obtained up to the 11th harmonic inclusive (11 pulses per period). The theoretical model also shows at what parameters such modes are possible and could be stable.

All the above need extended research and development before they could be implemented in a commercial device for routine application.

7 References

[ADA03] H. Adachi, K. Takano, Y. Hosokawa, T. Inoue, Y. Mori, H. Matsumura, M. Yoshimura, Y. Tsunaka, S. Morikawa, S. Kanaya, H. Masuhara, Y. Kai, and T. Sasaki. “Laser Irradiated Growth of Protein Crystal,” Jpn. J. Appl. Phys. 42, 798 (2003).

[Agr08] G. P. Agrawal. Nonlinear Fiber Optics. Academic Press, 4th edition (2008).

[AGR12] G. P. Agrawal. [Nonlinear Fiber Optics], Academic Press, 5th Edition (2012).

[AGR13] G.P. Agrawal Nonlinear Fiber Optics, 5th ed. Elsevier 2013

[AGU10] C. Aguergaray, D. Méchin, V. Kruglov, J. Harvey. “Experimental realization of a mode-locked parabolic Raman fiber oscillator” Opt. Exp. 18, 8680 (2010).

[AGU12] C. Aguergaray, N. Broderick, M. Erkintalo, J. Chen, V. Kruglov. “Mode-locked femtosecond all-normal all-PM Yb-doped fiber laser using a nonlinear amplifying loop mirror” Opt. Exp. 20, 10545 (2012).

[AKH05] N. Akhmediev and A. Ankiewicz: Dissipative Solitons in the Complex Ginzburg-Landau and Swift-Hohenberg Equations, Lect. Notes Phys. 661, 1–17 (2005)

[Arm62] J. A. Armstrong, N. Bloembergen, J. Ducuing and P. S. Pershan. “Interactions between light waves in a nonlinear dielectric”. Phys. Rev., 127 (1962) pp. 1918.

[BAN08] D. Banks, C. Grivas, I. Zergioti, I., and R. Eason. “Ballistic laser-assisted solid transfer (BLAST) from a thin film precursor,” Opt. Express 16(5), 3249 (2008).

[BAO09] Q. Bao, H. Zhang, Y. Wang, Z. Ni, Y. Yan, Z.X. Shen, K.P. Loh and D.Y. Tang, “Atomic-layer graphene as a saturable absorber for ultrafast pulsed lasers”, *Adv. Funct. Mater.* **19**, 3077 (2009)

[BLA00] K.A. Blanks. “Novel synthesis of gibbsite by laser-stimulated nucleation in supersaturated sodium aluminate solutions,” Journal of Crystal Growth 220, 572 – 578 (2000).

[Cap91] G. Cappellini and S. Trillo. “Third-order three-wave mixing in single-mode fibers: exact solutions and spatial instability effects”. J. Opt. Soc. Am. B, 8 (1991) pp. 824.

[Cha11] B. H. Chapman, E. J. R. Kelleher, S. V. Popov, K. M. Golant, J. Puustinen, O. Okhotnikov and J. R. Taylor. “Picosecond bismuth-doped fiber MOPFA for frequency conversion”. Opt. Lett., 36 (2011) pp. 3792.

[CHE05] Y. Cheng, K. Sugioka, and K. Midorikawa. “Freestanding optical fibers fabricated in a glass chip using femtosecond laser micromachining for lab-on-a-chip application, ”Opt. Express 13(18), 7225-7232 (2005).

[Che13] Y. Chen, W. J. Wadsworth and T. A. Birks. “Ultraviolet four-wave mixing in the LP02 fiber mode”. Opt. Lett., 38 (2013) pp. 3747.

[COE08] Y. Coello, V.V. Lozovoy, T.C. Gunaratne, B. Xu, I. Borukhovich, C. Tseng, T. Weinacht and M. Dantus. “Interference without an interferometer: a different approach to measuring, compressing, and shaping ultrashort laser pulses,” J. Opt. Soc. Am. B 25(6), A410-A150 (2008).

[DAN03] M. Dantus, V. V. Lozovoy, and I. Pastirk, "Measurement and Repair: The femtosecond Wheatstone Bridge." OE Magazine 9 (2003).

[DAN17] M. Dantus. [Femtosecond Laser Shaping: From Laboratory to Industry], CRC Press (2017).

[DES93] E.A. deSouza, C.E. Soccolich, W. Pleibel, R.H. Stolen, J.R. Simpson, and D.J. diGiovanni, “Saturable absorber mode-locked polarization maintaining erbium-doped fibre laser”, *Elect. Lett.* **29**, 447 (1993).

[DIA06] A. Diaspro, P. Bianchini, G. Vicidomini, M. Faretta, P. Ramoino and C. Usai. “Multi-photon excitation microscopy,” Biomedical Engineering 5, 36 (2006).

[DOR88] N.J. Doran and D. Wood, “Nonlinear optical loop mirror”, *Opt. Lett*. **13**, 56 (1988).

[DRO11] M. Drobizhev, N.S. Makarov, S.E. Tillo, T.E. Hughes and A. Rebane. “Two-photon absorption properties of fluorescent proteins,” Nature Methods 8(5), 393 – 399 (2011).

[dM04] C. J. S. de Matos, J. R. Taylor and K. P. Hansen. “Continuous-wave, totally fiber integrated optical parametric oscillator using holey fiber”. Opt. Lett., 29 (2004) pp. 983.

[Dud07] J. M. Dudley, C. Finot, D. J. Richardson and G. Millot. “Self-similarity in ultrafast nonlinear optics”. Nat Phys, 3 (2007) pp. 597.

[Dul91] I. N. Duling. “All-fiber ring soliton laser mode locked with a nonlinear mirror”. Opt. Lett., 16 (1991) pp. 539.

[Far59] M. Faraday “Experimental Researches in Chemistry and Physics”.

[FER90] M. E. Fermann, F. Haberl, M. Hofer, and H. Hochreiter, “Nonlinear amplifying loop mirror”, *Opt. Lett.* **15**, 752 (1990).

[Fis69] R. Fisher, P. Kelly and T. Gustafson. “Subpicosecond pulse generation using the optical Kerr effect”. IEEE J. Quantum Electron., 5 (1969) pp. 325.

[Gal01] A. Galvanauskas. “Mode-scalable fiber-based chirped pulse amplification systems”. IEEE J. Sel. Top. Quantum Electron., 7 (2001) pp. 504.

[Gom85] A. S. L. Gomes, U. Österberg, W. Sibbett and J. R. Taylor. “An experimental study of the primary parameters that determine the temporal compression of CW Nd:YAG laser pulses”. Opt. Commun., 54 (1985) pp. 377.

[Gom86] A. S. L. Gomes, W. Sibbett and J. R. Taylor. “Spectral and temporal study of picosecond-pulse propagation in a single-mode optical fibre”. Appl. Phys. B, 39 (1986) pp. 43.

[Gui15] F. Guichard, Y. Zaouter, M. Hanna, K.-L. Mai, F. Morin, C. Hönninger, E. Mottay and P. Georges. “High-energy chirped- and divided-pulse Sagnac femtosecond fiber amplifier”. Opt. Lett., 40 (2015) pp. 89.

[Han88] D. Hanna, J. Townsend and A. Tropper. “Continuous-wave oscillation of a monomode ytterbium-doped fibre laser”. Electron. Lett., 24 (1988) pp. 1111. [Har64] L. E. Hargrove, R. L. Fork and M. A. Pollack. “Locking of He-Ne laser modes induced by synchronous intracavity modulation”. Appl. Phys. Lett., 5 (1964) pp. 4.

[Has73] A. Hasegawa and F. Tappert. “Transmission of stationary nonlinear optical pulses in dispersive dielectric fibers. I. Anomalous dispersion”. Appl. Phys. Lett., 23 (1973) pp. 142. 130References

[Hec04] J. Hecht. City of Light - The Story of Fiber Optics. Oxford University Press (2004).

[HEL12] D. Hélie, F. Lacroix and R. Vallée. “Reinforcing a Direct Bond between Optical Materials by Filamentation Based Femtosecond Laser Welding,” J. Laser Micro/Nanoengineering 7(3), 284 (2012).

[Hol02] D. Hollenbeck and C. D. Cantrell. “Multiple-vibrational-mode model for fiberoptic Raman gain spectrum and response function”. J. Opt. Soc. Am. B, 19 (2002) pp. 2886.

[IAC98] C. Iaconis, I. A. Walmsley,. (1998), "Spectral Phase Interferometry for Direct Electric-Field Reconstruction of Ultrashort Optical Pulses", Opt. Lett., 23 (10):792–794, Bibcode:1998
OptL...23..792I, doi:10.1364/OL.23.000792, PMID 18087344

[IKE15] K. Ikeda, M. Maruyama, Y. Takahashi, Y. Mori, H.Y. Yoshikawa, S. Okada, H. Adachi, S. Sugiyama, K. Takano, S. Murakami, H. Matsumura, T. Inoue, M. Yoshimura, and Y. Mori. “Selective crystallization of the metastable phase of indomethacin at the interface of liquid/air bubble induced by femtosecond laser irradiation,” Applied Physics Express 8, 045501 (2015).

[Isl02] M. Islam. “Raman amplifiers for telecommunications”. IEEE J. Sel. Top. Quantum Electron., 8 (2002) pp. 548.

[Jau12] C. Jauregui, A. Steinmetz, J. Limpert and A. Tünnermann. “High-power efficient generation of visible and mid-infrared radiation exploiting four-wavemixing in optical fibers”. Opt. Express, 20 (2012) pp. 24957. 131References

[Kla60] J. R. Klauder, A. C. Price, S. Darlington and W. J. Albersheim. “The theory and design of chirp radars”. Bell Systems Technical Journal, 39 (1960) pp. 745.

[KOB10] S. Kobtsev, S. Kukarin, S. Smirnov, Y. Fedotov “High energy mode-locked all-fiber laser with ultra-long resonator” Las. Phys. 20, 351 (2010).

[Kru02] V. I. Kruglov, A. C. Peacock, J. D. Harvey and J. M. Dudley. “Self-similar propagation of parabolic pulses in normal-dispersion fiber amplifiers”. J. Opt. Soc. Am. B, 19 (2002) pp. 461.

[Lau69] A. Laubereau. “External frequency modulation and compression of picosecond pulses”. Physics Letters A, 29 (1969) pp. 539.

[Lav10] L. Lavoute, J. C. Knight, P. Dupriez and W. J. Wadsworth. “High power red and near-IR generation using four wave mixing in all integrated fibre laser systems”. Opt. Express, 18 (2010) pp. 16193.

[Lim06] J. Limpert, F. Roser, T. Schreiber and A. Tünnermann. “High-power ultrafast fiber laser systems”. IEEE J. Sel. Top. Quantum Electron., 12 (2006) pp. 233.

[Mae90] M. Maeda, W. Sessa, W. Way, A. Yi-Yan, L. Curtis, R. Spicer and R. Laming. “The effect of four-wave mixing in fibers on optical frequency-division multiplexed systems”. J. Lightwave Technol., 8 (1990) pp. 1402.

[Mai60] T. H. Maiman. “Stimulated optical radiation in ruby”. Nature, 187 (1960) pp. 493.

[MAM98] P. V. Mamyshev, “All-optical data regeneration based on self-phase modulation effect,” in 24th European Conference on Optical Communication (ECOC ’98) (IEEE Cat. No.98TH8398), 475–476 (1998).

[MAR96] Javier Martin and Jose Capmany, Transfer functions of double- and multiple-cavity fabry–perot filters driven by lorentzian sources. Applied Optics 35, 1996 p. 7108

[Moc65] H.W. Mocker and R.J. Collins, “Mode competition and self-locking effects in a Q-switched Ruby laser”, *App. Phys. Lett*. **7**, 270 (1965).

[Mol80] L. F. Mollenauer, R. H. Stolen and J. P. Gordon. “Experimental Observation of Picosecond Pulse Narrowing and Solitons in Optical Fibers”. Phys. Rev. Lett., 45 (1980) pp. 1095.

[Mol84] L. F. Mollenauer and R. H. Stolen. “The soliton laser”. Opt. Lett., 9 (1984) pp. 13.

[Mou11] G. Mourou and T. Tajima. “The extreme light infrastructure: Optics’ next horizon”. Opt. Photon. News, 22 (2011) pp. 47.

[NAI16] M. Nairat, A. Konar, V.V. Lozovoy, W.F. Beck, G.J. Blanchard and M. Dantus. “Controlling S2 Population in Cyanine Dyes Using Shaped Femtosecond Pulses,” J. Phys. Chem. A 120, 1876-1885 (2016).

[Nak81] H. Nakatsuka, D. Grischkowsky and A. C. Balant. “Nonlinear picosecond-pulse propagation through optical fibers with positive group velocity dispersion”. Phys. Rev. Lett., 47 (1981) pp. 910.

[NIC07] J. Nicholson, S. Ramachandran, S. Ghalmi. “A passively mode-locked, Yb-doped, figure eight, fiber laser utilizing anomalous-dispersion higher-order-mode fiber” Opt. Exp. 15, 6623 (2007).

[NEL97] L. Nelson, D. Jones, K. Tamura, H. Haus, E. Ippen. “Ultrashort pulse fiber ring laser” Appl. Phys. B 65, 277 (1997).

[PES14] D. Pestov, A. Ryabtsev, G. Rasskazov, V.V Lozovoy and M. Dantus. “Real-time single-shot measurement and correction of pulse phase and amplitude for ultrafast lasers,” Opt. Eng. 53, 051511 (2014).

[Poc85] J. P. Pochelle, J. Raffy, M. Papuchon and E. Desurvire. “Raman and four photon mixing amplification in single mode fibers”. Opt. Eng., 24 (1985).

[Ram28] C. V. Raman. “A New Radiation”. Indian J. Physics, 2 (1928).

[Ric91] D. Richardson, R. Laming, D. Payne, V. Matsas and M. Phillips. “Selfstarting, passively modelocked erbium fibre ring laser based on the amplifying Sagnac switch”. Electron. Lett., 27 (1991) pp. 542.

[RIC04] M. Richardson, A. Zoubir, C. Rivero, C. Lopez, L. Petit and K. Richardson. “Femtosecond laser micro-structuring and refractive index modification applied to laser and photonic devices,” Proc. SPIE 5347, 18 – 27 (2004).

[Ric10] D. J. Richardson, J. Nilsson and W. A. Clarkson. “High power fiber lasers: current status and future perspectives”. J. Opt. Soc. Am. B, 27 (2010) pp. B63.

[Sal07] B. E. A. Saleh and M. C. Teich. Fundamentals of Photonics. Wiley, 2nd edition (2007).

[SAM16] I. Samartsev, A. Bordenyuk “Passively mode-locked fiber ring generator” US10193296B2 2019-01-29, PATENT

[SAM17] I. Samartsev, A. Bordenyuk and V. Gapontsev “Environmentally stable seed source for high power ultrafast laser,” Proc. SPIE 10085, 100850S (2017).

[SAM18] I. Samartsev, A. Bordenyuk, “Passively mode-locked fiber ring generator,” US Patent # US 10,193,296, B2.

[SER2003] J. Serbin, A. Egbert, A. Ostendorf, B.N. Chichkov, R. Houbertz, G. Domann, J. Schulz, C. Cronauer, L. Fröhlich and M. Popall. “Femtosecond laser-induced two-photon polymerization of inorganic–organic hybrid materials for applications in photonics,” Opt. Lett. 28(5), 301 (2003).

[SET04] S.Y. Set, H. Yaguchi, Y. Tanaka, and M. Jablonski, “Laser mode locking using a saturable absorber incorporating carbon nanotubes”, *J. Lightwave Tech.* **22**, 51 (2004).

[Sha82] C. V. Shank, R. L. Fork, R. Yen, R. H. Stolen and W. J. Tomlinson. “Compression of femtosecond optical pulses”. Appl. Phys. Lett., 40 (1982) pp. 761.

[Shc13] E. Shcherbakov, V. Fomin, A. Abramov, A. Ferin, D. Mochalov and V. P. Gapontsev. “Industrial grade 100 kW power CW fiber laser”. In Advanced Solid-State Lasers Congress. Optical Society of America (2013), p. ATh4A.2.

[Sni88] E. Snitzer, H. Po, F. Hakimi, R. Tumminelli and B. McCollum. “Double-clad, offset core Nd fiber laser”. In Proc. Conf. Optical Fiber Sensors, paper PD5. Optical Society of America (1988).

[SOH05] I.B. Sohn and M.S. Lee. “Fabrication of photonic devices directly written within glass using a femtosecond laser,” Opt. Express 13(11), 4224-4229 (2005).

[STE06] D. Stevenson, B. Agate, X. Tsampoula, P. Fischer, C.T.F. Brown,, W. Sibbett, A. Riches, F. Gunn-Moore and K. Dholakia. “Femtosecond optical transfection of cells: viability and efficiency,” Opt. Express 14(16), 7125 – 7133 (2006).

[Sto72] R. H. Stolen, E. P. Ippen and A. R. Tynes. “Raman oscillation in glass optical waveguide”. Appl. Phys. Lett., 20 (1972) pp. 62.

[Sto74] R. H. Stolen, J. E. Bjorkholm and A. Ashkin. “Phase-matched three-wave mixing in silica fiber optical waveguides”. Appl. Phys. Lett., 24 (1974) pp. 308.

[Sto75] R. H. Stolen. “Phase-matched-stimulated four-photon mixing in silica-fiber waveguides”. IEEE J. Quantum Electron., 11 (1975) pp. 100.

[Sto78] R. H. Stolen and C. Lin. “Self-phase-modulation in silica optical fibers”. Phys. Rev. A, 17 (1978) pp. 1448.

[Sto82] R. H. Stolen and J. Bjorkholm. “Parametric amplification and frequency conversion in optical fibers”. IEEE J. Quantum Electron., 18 (1982) pp. 1062.

[STOl82] R.H. Stolen, J. Botineau and A. Ashkin, “Intensity discrimination of optical pulses with birefringent fibers“, *Opt. Lett*. **7**, 512 (1982).

[su214] “The Worldwide Market for Lasers - Market Review and Forecast 2014”. Technical report, Strategies Unlimited - PennWell (2014).

[SUG11] T. Sugiyama and H. Masuhara. “Laser-induced crystallization and crystal growth,” Chem Asian J. 6, 2878-2889 (2011).

[SUN12] Z. Sun, T. Hasan and A.C. Ferrari, “Ultrafast lasers mode-locked by nanotubes and graphene”, *Physica E*, **44**, 1082 (2012).

[TRE02] Rick Trebino’s book, Frequency-Resolved Optical Gating: The Measurement of Ultrashort Laser Pulses, Kluwer Academic Publishers, 2002.

[TRE97] R. Trebino, K. W. DeLong, D. N. Fittinghoff, J. N. Sweetser, M. A. Krumbügel, and D. J. Kane, "Measuring Ultrashort Laser Pulses in the Time-Frequency Domain Using Frequency-Resolved Optical Gating," Review of Scientific Instruments 68, 3277-3295 (1997).

[TZE09] Y.W. Tzeng, Y.Y. Lin, C.H. Huang, J.M. Liu, H.C. Chui, H.L. Liu, J.M. Stone, J.C. Knight and S.W. Chu. “Broadband tunable optical parametric amplification from a single 50 MHz ultrafast fiber laser,” Opt. Express 17(9) 7304 – 7309 (2009).

[WEI11] A.W. Weiner. [Ultrafast Optics], John Wiley & Sons (2011).

[WIP13] A. Wipfler, J. Rehbinder, T. Buckup and M. Motzkus. “Elimination of two-photon excited fluorescence using a single-beam coherent anti-Stokes Raman scattering setup,” J. Raman Spectroscopy 44, 1379-1384 (2013).

[WOR08] D. Wortmann, J. Gottmann, N. Brandt and H. Solle. “Micro- and nanostructures inside sapphire by fs-laser irradiation and selective etching,” Opt. Express 16(3), 1517-1522 (2008).

[XU06] B. Xu, J.M. Gunn, J.M. Dela Cruz, V.V. Lozovoy and M. Dantus. "Quantitative investigation of the multiphoton intrapulse interference phase scan method for simultaneous phase measurement and compensation of femtosecond laser pulses," J. Opt. Soc. Am. B 23(4), 750-759 (2006).

[Yan96] F. Yang, M. Marhic and L. Kazovsky. "CW fibre optical parametric amplifier with net gain and wavelength conversion efficiency gt;1". Electron. Lett., 32 (1996) pp. 2336.

[Yar77] A. Yariv and D. M. Pepper. "Amplified reflection, phase conjugation, and oscillation in degenerate four-wave mixing". Opt. Lett., 1 (1977) pp. 16.

[ZHA10] L.M. Zhao, D.Y. Tang, H. Zhang, X. Wu, Q. Bao and K.P. Loh, "Dissipative soliton operation of an ytterbium-doped fiber laser mode locked with atomic multilayer graphene", *Opt. Lett.* **35**, 3622 (2010).

[ZHAN12] M. Zhang, E.J.R. Kelleher, F.Torrisi, Z. Sun, T. Hasan, D. Popa, F. Wang, A.C. Ferrari, S.V. Popov and J.R. Taylor, "Tm-doped fiber laser mode-locked by graphene-polymer composite", *Opt. Exp*. **20**, 25077 (2012).

[ZIR91] M. Zirngibl, L.W. Stulz, J. Stone, J. Hugi, D. diGiovanni and P.B. Hansen, "1.2 ps pulses from passively mode-locked laser diode pumped Er-doped fibre ring laser", *Elect. Lett.* **27**, 1734 (1991).

8 Acronyms

The following is a list of acronyms used throughout this thesis, presented in alphabetical order. Throughout the body of the text, the acronyms are defined once in their position of first use, then not again; except in figure captions where they are defined for every occurrence:

ACF – Auto Correlation Function

AML - Actively Mode-Locked

AR - Anti-Reflection

ASE - Amplified Spontaneous Emission

CGLR – Complex Ginsburg-Landau Equation

CF – Cross Filter

CW - Continuous-Wave

DFG - Difference-Frequency Generation

EDFA - Erbium-Doped Fiber Amplifier

Er - Erbium

FBG - Fiber-Bragg Grating

FPC - Fiber-Polarization Controller

FROG - Frequency-Resolved Optical Gating

FWHM - Full-Width at Half Maximum

FWM - Four-Wave Mixing

GVD - Group Velocity Dispersion

IR - Infra-Red

LD - Laser-Diode

LMA - Large-Mode Area

LP - Linear Polarized

MCVD - Modified Chemical Vapor Deposition

MFD - Mode-Field Diameter

MIIPS - Multiphoton Intrapulse Interference Phase Scan

MOPA - Master Oscillator Power Amplifier

MOPFA - Master Oscillator Power Fibre Amplifier

NA - Numerical Aperture

NALM - Nonlinear Amplification Loop Mirror

Nd - Neodymium

NLPR - Nonlinear Polarization Rotation

NOLM - Nonlinear Optical Loop Mirror

OSA - Optical Spectrum Analyzer

PER - Polarization Extinction Ratio

PD - Photodiode

PM - Polarization-Maintaining

PML - Passively-Mode Locked

SBS - Stimulated Brouillion Scattering

SESAM - Semiconductor Saturable Absorber Mirror

SFG - Sum-Frequency Generation

SHG - Second-Harmonic Generation

SLD - Semiconductor Laser Diodes

SLM - Spatial Light Modulator

SOD- Second-Order Dispersion

SPIDER - Spectral Phase Interferometry for Direct Electric-field Reconstruction

SPM - Self-Phase Modulation

SRS - Stimulated Raman Scattering

SSFM - Split-Step Fourier Method

Tm - Thulium

TL – Transform Limited

TOD – Third-Order Dispersion

UV - Ultra-Violet

XPM - Cross Phase Modulation

Yb - Ytterbium

9 List of publications:

1. Gapontsev V. P., Sadovskii P. I., Samartsev I. E., Shestakov A. V., Blinov L. M.,“Activated fiber lasers and prospects of their applications in medicine”.SPIE Vol. 1353, Lasers and Medicine, 1989, pp. 208-212.

2. Vorobiov I.L., Gapontsev V.P., Sadovsky P.I, Samartsev I.E., «The device for temperature measurement». The copyright certificate № 1591632 from May, 08th, 1988

3. Gapontsev V. P., Samartsev I. E.,“High Power Fiber Laser”.Conf. “Advanced Solid State Lasers”. March 1990. Proc. SPIE. Vol.-Salt Lake City, Utah

4. Gapontsev, V.P., and Samartsev, L. E., “High-power fiber laser,” Optical Society of America Trends in Optics and Photonics Series on Advanced Solid-State Lasers Proceedings, 6:258-262. 1991,

5. Gapontsev V.P, Sadovskii P.I., Samartsev I.E.1,5-um Erbium Glass Lasers .Conference on Lasers and Electrooptic, May 21-25, 1990, Anaheim, California, p.682-683

6. V.P.Gapontsev, I.E. Samartsev, L.M.Blinov, A.I.Zayats, R.R.Lorian, V.M.Firsov,“Single-mode erbium-doped quartz fiber lasers”In Technical Digest of USSR Conference “Laser optics” Leningrad, 1990, pp.45-46.

7. Gapontsev V. P., Samartsev I. E., Zayats A. A., Loryan R. R.,“Laser-diode-Pumped Yb-Doped Single-Mode Tunable Fiber Laser”.“Advanced Solid State Lasers”.IEEE/Lasers/ and Electro-Optics Society Optical Society of America SDIO/ Innovative Science and Technology Office, 1991 Technical Digest Series, March 18-20, Hilton Head, South Carolina.

8. Gapontsev V. P.,, Dianov E.M., Duraev V.P, Kiselev A.V., Kuznetsov A.V., Samartsev I.E., Prohorov A.M., Shcherbakov E.A.,«Fiber интерферометр Majkelsona with indemnification of losses».Quantum electronics, T. 18, № 9, 1991, p. 1137-1139.

9. Gapontsev V. P., Samartsev I. E., Zayats A. A., Loryan R. R., “High Efficiency, LD-Pumped, ND-Doped CW Fiber Lasers With Output Power Scaled To One Watt”.IEEE/Lasers and Electro-Optics Society. February 17-19, 1992, Santa Fe, New Mexico.

10. Gapontsev V.P., Ivanov G. A., Koreneva N. A., LeBedera Z. M., Samartsev I. E., Chamorovsky Yu. K.,“Active Fiber Light-Guides”.ISFIK’92, pp. 180-182.

11. Gapontsev V. P., Samartsev I. E.,“LD-pumped Tunable CW Lasers”.ISFOC’92, p. 187-189.

12. Buritskii K.S., Gapontsev V. P., Dianov E. M., Maslov V. A., Samartsev I. E., Chernykh V. A., Shcherbakov E. A.,“Blue-green light generation from a neodymium fiber laser”.Santa Fe, NM, February 20-21, 1992 Technical Digest V.6 OSA

13. Sychugov V. A., Tikhomirov A. E., Kuznetsov A. V., Samartsev I. E., “Narrow-band laser with an Nd^{3+}-activated fibre”.Kvantovaya Electronika and Turpion Ltd, 1993.Quantum Electronics, vol. 24, No. 1, 1994, 00-00.

14. Gapontsev V. P., Zaiatz A.I., Lorian R.R., Samartsev I.E., Timonin S.A., High efficiency singlemode tunable laser with LD pump based on Yb^{3+} doped fiber.

15. Gapontsev V. P., Samartsev I.,“A High Optical Fiber Amplifier Pumped By a Multi-Mode Laser Source”,International Patent Classification: H01S 3/06

16. Alekseev E.I., Basarob E.N., Gerasimov A.G.,, Gubin V.V., Samartsev I.E., Starostin N.I.,«Polarising characteristics of a superfluorescent source of radiation on the basis of a erbium doped fiber».Letters in MTF, т. 21, iss. 5, 1995, pp. 25-30.

17. Alekseev E.I., Basarob E.N., Gerasimov A.G.,, Gubin V.V., Samartsev I.E., Starostin N.I.,«A fiber-optical gyroscope with a fiber source of radiation for length of a wave 1.54 microns». Letters in MTF, т. 21, iss. 11, 1994, pp.10-13.

18. Chenikov S. V., Taylor J. B., Samartsev I., Gapontsev V. P.,“Compact, All-Diode Pumped Fibre Optical Pulse Source at 35-80 Gbit/s”.Abstract. in Optical Fiber Communications Conference, Vol. 8 of 1995 OSA Technical Digest Series (Optical Society of America, 1995), paper ThM3.

19. Gapontsev V. P., Fomin V. V., Samartsev I. E., Unt A., “25kW peak power, wide-tuneable-repetition-rate and duration eye-safe MOPFA laser”.CLEO’96/ Tuesday AFTERNOON/ p. 209.

20. Chernikov S. V., Taylor J. R., Gapontsev D. V., Samartsev I. E., “Q-switching of Er^{3+}/Yb^{3+}-doped fiber laser using back scattering a fiber ring interferometer”.CLEO’96, Friday MORNING/ p. 259.

21. Alekseev E.I., Basarob E.N., Gerasimov A.G.,, Gubin V.V., Samartsev I.E., Starostin N.I.,2-wavelenght a superfluorescent fiber source of radiation., Letters in MTF, 1997, vol. 23, iss. 20

22. Alekseev E.I., Basarob E.N., Gapontsev V.P., Gerasimov A.G.,, Gubin V.V., Samartsev I.E., Starostin N.I.,Fiber-optical gyroscope with suppression of superfluous noise of a source of radiation., Letters in MTF, vol: 24, num: 18, 30-35, published: , RU

23. V.N. Bagratashvili, N.V. Bagratashvili, V.P. Gapontsev, G.Sh. Makhmutova, V.P. Minaev, A.I. Omel'chenko, I.E. Samartsev, A.P. Sviridov, E,N, Sobol', S.I. Tsypina.“Variation of optical

properties of hyaline cartilage caused by heating by near-IR laser radiation”. Quantum electronics, vol. 31, №. 6, pp. 534-539, 2001.

24. Gapontsev V.P., Minaev V.P., Panteleev A.M., Pinsky I.A, Samartsev I.E.. Portable laser scalpel-koaguljator “LASON-10–P”THE BULLETIN OF PHYSIOLOGY AND PATHOLOGY OF BREATH 2001, RELEASE 10

25. Platonov N. S., Gapontsev D. V., Gapontsev V. P., Schumilin V.“135 W CW Fiber Laser With Perfect Single Mode Output”.CLEO-2002. Postdeadline Papers, CPDC3-1-CPDC3-3. Technical Conference, May 19-24, 2002, Long Beach, California, USA

26. Gapontsev V.P., Minaev V.P, Samartsev I.E. «Medical devices on the basis of powerful semi-conductor and fiber lasers».Quantum electronics, T. 32, № 11, 2002, p. 1003.

27. Gapontsev V.P., Minaev V.P, Samartsev I.E..,«Therapeutic laser devices on the basis of powerful diode and fiber lasers».Scientific session of MEPhI-2002, Moscow, the collection of works, т. 5, p. 66.

28. V. Golyshev, E.Zhukov, I. Samartsev, D. Slepov.,“Nonlinear effects and their mutual influence in fiber-optic communication lines”. 2nd International Symposium on High-Power Fiber Lasers and Their Applications, St. Petersburg, Russia, July, 2003.

29. V. Kislyanskich, M. Ryabko, I. Samartsev."High power, broadband, wavelength stable super fluorescent fiber source on the range of 1543 - 1604 nm". 2nd International Symposium on High-Power Fiber Lasers and Their Applications, St. Petersburg, Russia, July, 2003.

30. V. Golyshev, E. Zhukov, I. Samartsev, D. Slepov."Stimulated Raman scattering in fiber-optic long-haul communication lines".2nd International Symposium on High-Power Fiber Lasers and Their Applications, St. Petersburg, Russia, July, 2003.

31. V. Golyshev, E.Zhukov, I. Samartsev, D. Slepov."Remote pumping in ultra-long haul transmission systems".2nd International Symposium on High-Power Fiber Lasers and Their Applications, St. Petersburg, Russia, July, 2003.

32. Golishev I.A., GhukovE.A., Samartsev I.E, Slepov D.G. "The compelled combinational dispersion in fiber-optical communication lines".Magazine of technical physics, т. 74, p. 136-141, 2004.

33. Golishev I.A., GhukovE.A., Samartsev I.E, Slepov D.G. "Influence of phase self-modulation on the compelled dispersion of Mandelshtama - Brilljuena in fiber-optical communication lines".Magazine of technical physics, т. 74, № 7, p. 66-69, 2004.

34. Golishev I.A., GhukovE.A., Samartsev I.E, Slepov D.G. "Fiber - optical communication lines of the big range", Successes of modern radio electronics, № 5 – 6, p. 96-98, 2004.

35. Golishev I.A., GhukovE.A., Samartsev I.E, Slepov D.G. Phase self-modulation of radiation in fiber-optical communication lines Quantum Electronics, 36, 946 (2006).

36. Burkov V.A., Samartsev I.E.Krapivin V.F..“Application of technology of flexible information-modulating systems at creation of optical and fiber-optical devices and metrological systems in nanotechnology.”Ecology systems and equipment N11,2008.

37. Samartsev I.E.“Optical transport networks. Application of the newest optical technologies on transportnetworks and in access networks. New technologies of digital optical systems DWDM.”, Magazine "Photon-express", № 2(66) 2008, p. 26-28

38. V. Gapontsev, A. Avdokhin, P. Kadwani, I. Samartsev, N. Platonov, Roman Yagodkin “SM green fiber laser operating in CW and QCW regimes and producing over 550W of average output power”. Materials Science, Engineering, Photonics West - Lasers and Applications 20 February 2014

39. *Alex Yusim, I. Samartsev, V. Gapontsev “New generation of high average power industry grade ultrafast ytterbium fiber lasers” Materials Science, Engineering, LASE 11 March 2016

40. *Samartsev, A. Bordenyuk, V. Gapontsev “Environmentally stable seed source for high power ultrafast laser”. Materials Science, Engineering LASE 22 February 2017,

41. *A.Ryabtsev, D. Pestov, A. Bordenyuk, L. Goodman, V.V. Lozovoy, I. Samartsev, and V. Gapontsev, “New self-starting mode locked laser with active phase control”, Proc. SPIE, vol. 10899 (Components and Packaging for Laser Systems V), 108990T (2019)

42. *Pancho Tzankov, Jeff Kmetec, Igor Samartsev, Valentin Gapontsev, "Yb-Fiber Laser Pumped Optical Parametric Sources Using LBO Crystals", in Conference on Lasers and Electro-Optics, (Optical Society of America, Washington, D.C., 2019) p. JTu2A.95

---

*Published during the PhD research period

Issued Patents

1. VALENTIN GAPONTSEV, IGOR SAMARTSEV, PATENT A high power optical fiber amplifier pumped by a multi-mode laser source WO 95/10868, 20 April 1995

2. VALENTIN GAPONTSEV, IGOR SAMARTSEV, PATENT A diode pumped, cw operating, single-mode optical fiber laser emitting at 976 nm,WO 95/10869 20 April 1995

3. VALENTIN GAPONTSEV, IGOR SAMARTSEV, PATENT A coupling arrangement between a multi-mode light source and an optical fiber through an intermediate optical fiber length ,WO 96/20519, 4 July 1996

4. BUABBUD GEORGE (US); LEONARD JR (US); FUCHS WOLFRAM BERN (US); SAMARTSEV IGOR (RU), Patent Multiport optical amplifier with narrowcast power equalization WO 2004/070457 A3, 19 August 2004

5. VALENTIN, GAPONTSEV .P. | IGOR, SAMARTSEV Coupling arrangement between a multi-mode light source and an optical fiber through an intermediate optical fiber length US5999673A 1999-12-07

6. BUABBUD, GEORGE | MORNATTA, CRISTIANO | REEVES-HALL, PETER | SAMARTSEV, IGOR Fiber optic communication system with automatic line shutdown/power reduction US7917030B2 2011-03-29

7. SAMARTSEV, IGOR | ANTONENKO, VLADIMIR Fiber-optic long-haul transmission system US8139951B2 2012-03-20

8. ANTONENKO VLADIMIR, SAMARTSEV IGOR Optical system for multifrequency laser location and method for implementation thereof RU(11) 2 480 712(13) C2 27.04.2013

9. ANTONENKO VLADIMIR, MARJASHIN SERGEJ, SAMARTSEV IGOR, UNT ANDREJ Method for differential control of population inversion of laser medium and apparatus for realising said method RU (11) 2 480 875(13) C2 27.04.2013

10. ANTONENKO VLADIMIR, SAMARTSEV IGOR Dynamically stabilised relaxing wavelength laser system and operation method thereof RU(11) 2 480 876(13) C2 27.04.2013

11. SAMARTSEV IGOR High-speed optical line protected from eavesdropping by quantum noise RU (11) 2 520 419(13) C1 27.06.2014

12. SAMARTSEV, IGOR | ILYASHENKO, VICTOR | KEOVONGMANYSAR, DAVONE Method for assembling high power fiber laser system and module realizing the method US8682126B2 2014-03-25

13. SAMARTSEV, IGOR | ANTONENKO, VLADIMIR | PUDOV, LEONID Method for contactless laser welding and apparatus US8829388B2 2014-09-09

14. DAVYDOV Boris, SAMARTSEV Igor LASER RADIATION DISTRIBUTION METHOD AND MULTIBEAM LASER SYSTEM THEREFOR RU (11) 2 563 908(13) C1 : 27.09.2015

15. MARYASHIN, SERGEY | UNT, ANDREY | SAMARTSEV, IGOR | ANTONENKO, VLADIMIR Method and apparatus for differentially controlling population inversion in gain medium US8953652B2 2015-02-10

16. GAPONTSEV, VALENTIN | SAMARTSEV, IGOR High power single mode ytterbium fiber laser system with single mode neodymium fiber pump source US9036667B2 2015-05-19

17. GAPONTSEV, VALENTIN | SAMARTSEV, IGOR High power single mode fiber pump laser systems at 980 nm US9088131B1 2015-07-21

18. GAPONTSEV, VALENTIN | SAMARTSEV, IGOR High power fiber pump source with high brightness, low-noise output in about 974-1030 nm wavelength US9300108B2 2016-03-29

19. GAPONTSEV, VALENTIN | SAMARTSEV, IGOR Ultra high power single mode fiber laser system US9306364B2

20. GAPONTSEV, VALENTIN | SAMARTSEV, IGOR | YUSIM, ALEX High power ultra-short pulse laser-illuminated projector US9395612B2 2016-07-19

21. GAPONTSEV, VALENTIN | SAMARTSEV, IGOR | YAGODKIN, DIMITRI Ultra-high power single mode fiber laser system with non-uniformly configured fiber-to-fiber rod multimode amplifier US9444215B1 2016-09-13

22. FOMIN, VALENTIN | FERIN, ANTON | ABRAMOV, MIKHAIL | SAMARTSEV, IGOR | GAPONTSEV, VALENTIN Ultra-high power single mode fiber laser system with non-uniformly configure fiber-to-fiber rod multimode amplifier US9667023B2 2017-05-30

23. *AVDOKHIN, ALEXEY | EROKHIN, YURI | LEONARDO, MANUEL | LIMANOV, ALEXANDER | SAMARTSEV, IGOR | VON DADELSZEN, MICHAEL Process and system for uniformly crystallizing amorphous silicon substrate by fiber laser US9941120B2 2018-04-10

24. *LEONARDO, MANUEL | SAMARTSEV, IGOR | AVDOKHIN, ALEXEY | KEATON, GREGORY Broadband red light generator for RGB display US10008819B2 2018-06-26

25. *LEONARDO, MANUEL | SAMARTSEV, IGOR | AVDOKHIN, ALEXEY | KEATON, GREGORY RGB laser source for luminaire projector system US10170886B2 2019-01-01

26. *SAMARTSEV, IGOR | BORDENYUK, ANDREY Passively mode-locked fiber ring generator US10193296B2 2019-01-29

27. *SAMARTSEV, IGOR | BORDENYUK, ANDREY Giant-chirp all-normal-dispersion subnanosecond fiber oscillator US10367327B2 2019-07-30

28. *GAPONTSEV, VALENTIN | SAMARTSEV, IGOR | AVDOKHIN, ALEXEY Ultra-high power single mode green fiber laser operating in continuous wave and quasi-continuous wave regimes US10520790B2 2019-12-31

29. *AVDOKHIN, ALEXEY | EROKHIN, YURI | LEONARDO, MANUEL | LIMANOV, ALEXANDER | SAMARTSEV, IGOR | VON DADELSZEN, MICHAEL Process and system for uniformly crystallizing amorphous silicon substrate by fiber laser USRE48398E1 2021-01-19

*Filed during the period of this PhD program.